UNIVERSITÀ DEGLI STUDI DI PADOVA

LEIBNIZ UNIVERSITÄT HANNOVER

DIPARTIMENTO DI INGEGNERIA INDUSTRIALE

CORSO DI LAUREA MAGISTRALE IN INGEGNERIA DELL'ENERGIA ELETTRICA

Optimization of Pulsed Magnetic Field Application for Electromagnetic Stirring during the Continuous Casting

Author:

Mattia Guglielmi [1111022]

Supervisors:

Pf. Dr.-Ing. Egbert Baake

Ing. Michele Forzan

Dipl.-Ing. Diana Musaeva

Academic Year 2017/18

To my grandfather, Bruno.

Acknowledgements

My first acknowledgement goes to my supervisor, Prof. Michele Forzan, for his precious help, guidance and advice during my Master studies at the University of Padua and during the development of this Thesis work most of all. I am extremely thankful to Prof. Egbert Baake and Prof. Bernard Nacke, from Institute für Elektrothermische Prozesstechnik, Univeristät Hannover for the possibility to carry on experimental activities in their institute. They also gave me the opportunity to attend the HES 2017 conference, which represented to me a great motivation and matter for personal growth. A special acknowledgement goes to Dipl.-Ing. Diana Musaeva and Thomas Steinberg for their strong guidance and everyday support. I am also indebted to all the colleagues of the ETP for sharing their time and knowledge with me, not only during my experimental activities.

The greatest thank you goes to my family, who always supported me with patience and understanding, every day and humbly. Sara, Mattia, Claudio and Licia, you all are my second family; thank you for challenging the freezing wind of Hannover for me. Claire, you are my happiness and greatest supporter; my time in Hannover would have not been the same without you. Marco and Fabio, you have been my fellows and guides, but my friends most of all; thank you for sharing the Erasmus adventure together. Thank you Michele for being my matter of motivation and mate during my whole studies at the University; we shared projects, exams and anxiety. Jan, Eike and Emma, you have been the best roommates.

A final acknowledgement goes to all of the people, friends and colleagues I met during my Master studies and the development of my Thesis project especially. Each one of you taught me something I will never forget.

Abstract

The search for new materials with definite physical properties like homogeneity and high mechanical durability is one of the topics of the highest interest of the modern technology and industry. Therefore, there still remains a wide field for scientific investigations for developing new methods of material producing and improving existing techniques.

In the frame of metal production, Continuous Casting is the most cost- and energy-efficient method to mass-produce semi-finished metal products with consistent quality in a variety of sizes and shapes. It transforms molten metal into solid in a continuous process and is the most efficient way to solidify large volumes of metal into simple shapes for subsequent processing. Most basic metals are presently mass-produced using such process, including over 750 million tons of steel, 20 million tons of aluminium and 1 million tons of copper, nickel and other metals in the world each year.

In the majority of cases, properties of the cast metal are predicted with the conditions of their melting and solidification, thus defining these conditions is a key for achieving required qualities in the material. Magnetic fields are a powerful tool for continuous casting to provide expedient flow pattern in the molten material, with prospects for controlling the microstructure of solidifying metal. Use of the magnetic fields is widely used because it allows for a completely contactless influence on the melt and a direct control of the flow intensity through changing electrical parameters and by varying the design of electromagnetic (EM) field. Effective stirring of the liquid metal is provided, which brings to intense heat and mass transfer, then homogenization of temperature field and chemical components in the liquid volume. It is easy to notice that efficient stirring of the melt is a key component of the casting process, affecting both the quality of the produced metal and its cost.

This work was intended to the investigation of melt flow behaviour under the influence of electromagnetic stirring (EMS), when transient and not standard conditions occur along the casting line: application of AMF on the first solidification area generates two toroidal vortices within the liquid metal, similar to each other in terms of amplitude, velocity and energy. However, when cooling process is too fast or intense, the solidification front shifts upward dramatic variation in the dimension and velocity of the two vortices occurs; transition to a unique, large eddy modifies stirring conditions thus intense motion cannot be achieved anymore. Main goal of this thesis was to experimentally study the effect of low-frequency pulsed magnetic field (PMF) on Galinstan eutectic alloy, to optimize the stirring effect even during the transition of vortices and increase the rate of equiaxed

structure within the solidifying metal. Application of AMF was initially investigated with with the use of numerical model: experimental activity was carried on in parallel to validate simulation results and to understand conditions when the transition happened; relative position between melt and the inductor was changed to simulate shifting of the solidification front. Once shape and velocity of initial vortices dramatically changed, their characteristic rotation frequency was calculated and PMF with the same frequency was applied, to achieve resonance between mechanical (eddies velocity) and electrical (inductor's feeding current) parameters. Motion of melt flow was quantified with velocity of vortices and it was measured thanks to Ultrasound Doppler Velocity (UDV) meter; average standard deviation and fast Fourier transform (*fft*) of pulsed component of velocity were finally calculated.

This thesis consists of Abstract, 4 Chapters, including Conclusions and References.

Chapter 1 gives a description of the Continuous Casting process, including limits and advantages for quality improvement of final products; stirring methods and finally objectives of this investigation are described.

Chapter 2 includes detailed theoretical background for dealing with the stirring process, thus electromagnetic, thermal fields and hydrodynamic equations.

In **Chapter 3** numerical and experimental activities with the application of AMF are described, plus the first results from the simulation.

Chapter 4 deals with optimization of the stirring effect, thus starts from previous results to properly apply PMF; results from PMF application are described at the end of the Chapter.

Sommario

La ricerca di materiali sempre nuovi e con proprietà fisiche specifiche, quali buona omogeneità ed elevata resistenza meccanica, rappresenta ora un campo di forte interesse sia in ambito sperimentale che industriale. Per questo motivo, la ricerca scientifica sta cercando di sviluppare metodi sempre nuovi per la produzione dei diversi materiali, o di migliorare le tecnologie esistenti.

Il processo di Colata Continua (in inglese *Continuous Casting*) rappresenta il metodo più economico ed efficiente per la produzione di metalli semi-lavorati, caratterizzati da buona qualità, di diverse dimensioni e forme. Esso trasforma il metallo durante un processo continuo di solidificazione e costituisce perciò il metodo più efficace per solidificare grandi quantitativi di metallo in forme semplici, finalizzate ad una successiva lavorazione. Ogni anno nel mondo, grandi quantità di metallo di uso comune vengono prodotte sulla base di tale processo; si possono contare 750 milioni di tonnellate di acciaio, 20 di alluminio ed 1 milione di rame, nickel, oltre a numerosi altri materiali.

La conoscenza delle condizioni di fusione e solidificazione consente, nella maggior parte dei casi, di predirre con buona accuartezza le proprietà del prodotto finito. Ottenere determinate qualità e proprietà dello stesso significa quindi conoscere a fondo le condizioni di lavorazione del materiale. Uno degli strumenti più influenti nel processo di colata consiste nell'impiego di campi magnetici, con lo scopo di generare mescolamenti di comportamento opportuno nel metallo fuso, quindi controllare la sua struttura microcristallina in fase di solidificazione. I campi magnetici consentono anche l'interazione col metallo senza alcun contatto ed un controllo diretto dell'intensità del mescolamento tramite opportuna variazione dei parametri elettrici. Grazie alle proprietà conduttive del metallo stesso, l'azione del mapo magnetico produce un effetto di *stirring* che omogenizza temperatura e proprietà chimiche nel liquido. Uno *stirring* efficace ed efficiente costituisce quindi la chiave per produrre metalli di buona qualità ed a basso costo.

Obiettivo di questo lavoro di tesi è quello di analizzare il comportamento del metallo fuso influenzato dal processo di *stirring* elettromagnetico durante la colata continua, in condizioni operative non standard. l'applicazione di un campo magnetico alternato (AMF) in fase di primo raffreddamento dà origine nel metallo liquido a due vortici di forma toroidale simili tra loro, in termini di ampiezza, velocità ed energia. Con condizioni "non standard" ci si riferisce ad un processo di raffreddamento troppo veloce o intenso, tale per cui il fronte di solidificazione tende a muoversi verso l'alto, determinando una variazione di dimensione e velocità dei due vortici prodotti; si verifica quindi il passaggio

ad un unico vortice più ampio, tale da variare le condizioni nelle quali avviene lo *stirring*, e spesso renderele peggiori. Questo lavoro si propone di studiare le conseguenze dell'applicazione di un campo magnetico pulsato, a bassa frequenza, sulla lega eutettica GalInStan, allo scopo di ottimizzare gli effetti di mescolamento anche in fase di transizione da due ad un singolo vortice, aumentando comunque i grani equiassici nel prodotto finito. Il primo step consisteva nello studio dei risultati derivanti dall'applicazione di un campo alternato (AMF) sul setup sperimentale: simulazioni al calcolatore ed attività sperimentali sono state svolte in parallelo, per validare la correttezza dei loro risultati; quindi si è valutato quando si è svolta la transizione. Il movimento del fronte di solidificazione nel setup sperimentale è stato simulato tramite variazione della posizione relativa tra induttore e metallo fuso. Al variare dei due vortici, è stata calcolata la loro frequenza caratteristica di rotazione, quindi si è applicato un campo magnetico pulsato. La medesima frequenza è stata poi scelta per la corrente di alimentazione dell'induttore, allo scopo di ottenere un effetto di risonanza tra velocità dei vortici (grandezza meccanica) e la corrente stessa (grandezza elettrica). Le diverse componenti di velocità dei vortici sono state misurate tramite sonda ad Effetto Doppler (UDV); la componente pulsata della velocità è stata invece analizzata tramite calcolo della sua deviazione standard e della trasfomata veloce di Fourier.

Questa tesi contiene un Sommario iniziale e 4 Capitoli, incluse Conclusioni e Bibliografia.

Il **Capitolo 1** fornisce una descrizione generale del processo di Colata Continua, analizzando limiti e vantaggi della stessa, specialmente in termini di miglioramento della qualità del prodotto finale; in conclusione vengono descritti i metodi di stirring e gli obiettivi di questo lavoro.

Il **Capitolo 2** descrive la teoria alla base dello studio del processo di stirring elettromagnetico; si tratta di campi elettromagnetici, termici ed equazioni idrodinamiche.

Nel **Capitolo 3** vengono descritti i risultati dell'applicazione del campo magnetico alternato (AMF).

Il **Capitolo 4** tratta nel dettaglio del processo di ottimizzazione adottato per l'applicazione del campo pulsato (PMF) per lo *stirring*; i relativi risultati vengono descritti al termine del Capitolo.

Contents

List of Figures

List of Tables

Chapter 1

The Continuous Casting Line

1.1 Ingot forming and solidification process

Continuous casting, also called *strand casting*, is the process whereby molten metal is solidified into a semifinished billet, bloom or slab on a continuous basis. It is the most cost and energy efficient way to solidify large volumes of metal into simple shapes for subsequent processing and rolling in the finishing mills. In fact, in relation to other casting processes, continuous casting generally has a higher capital cost, but lower operating cost. Casting process was born in the middle of the 19th century, when Sir Henry Bessemmer received a patent for casting metal between two counter-rotating rollers. Its definitive application in commercial processes started though in the 1950s only, because earlier attempts suffered from technical difficulties such as breakouts and sticking of the solidifying metal on walls of the casting line. After overcoming this set of problems (for example, breakouts have been solved with vertically oscillating the mold), continuous casting has evolved to achieve yield, quality and cost efficiency. It allows lower cost production of metal sections with better quality, thanks to the continuous and standardized production of a product, as well as providing increased control over the process through automation. Prior to the introduction of continuous casting, molten metals were poured into stationary moulds to form ingots.

Continuous casting is used most frequently to cast steel but aluminium, copper and nickel are continuously casted in smaller quantities as well. It is distinguished from other solidification processes due to its steady state nature, relative to an outside observer who take the laboratory frame as reference; molten metal solidifies against the mould wall while it is simultaneously withdrawn from the bottom of the mould at a rate which maintains solid-liquid interface in a constant position with time. Best working conditions can be achieved when all the steps of the process operate in steady-state manner. During the

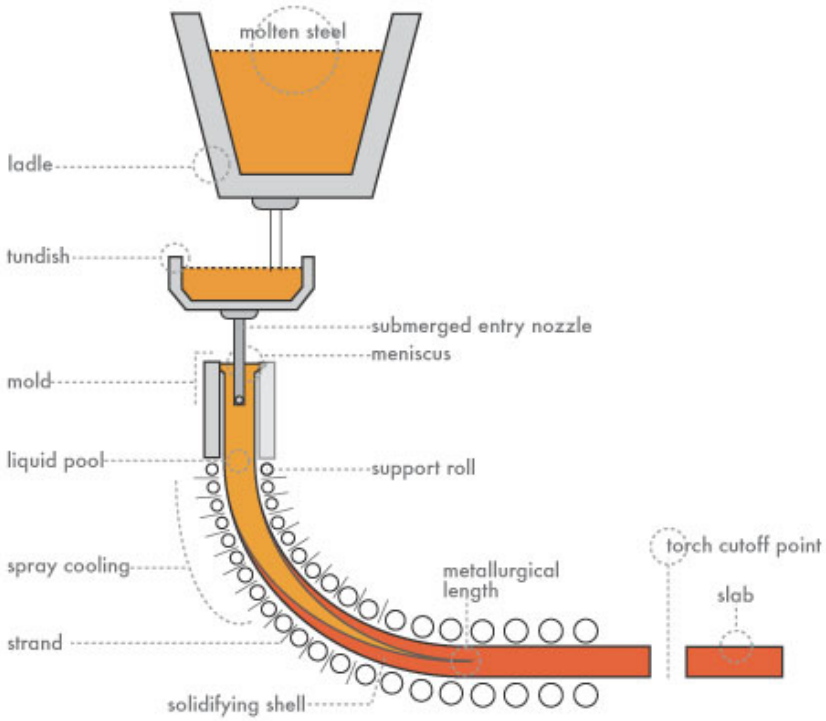

Fig. 1.1: Scheme of the Continuous Casting line

continuous casting process, molten metal flows from a ladle, through a tundish, into the mould (Fig.1.1): after being melted in furnaces, metal is tapped into the ladle, where it undergoes specific treatments, such as alloying and degassing, and it arrives at the correct temperature. The casting machine hosts two ladles in the same moment: the former, filled with molten metal, is transported in the *on-cast* position for feeding the casting machine from its top; the latter is made ready for the *off-cast* position and is switched to the casting position when the first ladle is empty. From the ladle, hot metal is transferred via refractory shroud (pipe) to a holding bath called tundish. The tundish allows a reservoir of metal for feeding the casting machine while switching the two ladles, thus behaving as a buffer of hot metal, as well as smoothing out flow, regulating metal feed to the moulds and cleaning the metal. Tundish flow pattern, in fact, is designed to allow foreign particles in molten metal to be removed, avoiding short circuits and excessive surface turbulence. Nozzles are necessary for this purpose and for controlling the flow. Molten metal is finally drained from the tundish to the top of an open-base copper mould, where the primary water cooling process happens: the mould, with a range from 0.5 to 2 [m], depending on the casting speed and section size, is water-cooled to solidify the molten metal directly in contact with it. It also oscillates vertically to prevent molten metal to stick to the mould walls. Furthermore, a lubricant is added to the metal in the mould for

preventing sticking and to trap any slag particle, including oxide particles or scale, and bring them to the top of the pool and form a floating layer of slag. The shroud, used for pouring molten metal from the tundish to the mould, is set so that hot metal exits it below the surface of the slag layer in the mould and is thus called *submerged entry nozzle* (SEN). Some continuous casting layouts feed several moulds from the same tundish. Once in the mould, a thin, solid shell of metal next to the mould walls solidifies before reaching the middle section of the casting line (the middle section is called strand) and exits the base of the mould into a spray chamber. The bulk of metal within the walls of the strand is still molten. The strand is supported by closely spaced, water-cooled rollers which support the walls of the strand against the ferrostatic pressure of the still-solidifying liquid within the strand. Large amounts of water are sprayed on the strand as it passes through the spray chamber in combination with radiation cooling, to increase the rate of solidification; the spray flow rates are adjusted to control strand surface temperature. This is the secondary cooling process. Final solidification of the strand may take place after the strand has exited the spray-chamber. It is here that the design of continuous casting machines may vary: *curved apron* configuration is adopted for the majority of steel casting; the strand exits the mould vertically or on a nearly vertical curved path and the rollers gradually curve the strand towards the horizontal as it travels through the spray-chamber. Note that moulds, in a curved apron casting line can be straight or curved, depending on the basic design of the machine. *Vertical* design is used to cast aluminium and few other metals for special applications; the strand stays vertical as it passes through the spray-chamber. The last configuration, the *horizontal* casting, is used occasionally for both non-ferrous alloys and steel. The mould axis is horizontal and the flow of steel is horizontal from liquid, to thin shell to solid; no bending is present. In this type of machine, either strand or mould oscillation is used to prevent sticking in the mould. After exiting the spray-chamber, the strand is processed with straightening and withdrawl rolls, taking advantage of its hot condition for achieving a pre-shape (Fig.1.2); the strand is cut into predetermined lengths by mechanical shears or by travelling oxyacetylene torches, it is marked for identification and finally taken either to a stockpile or to the next forming process. In many cases the strand may continue through additional rollers and other mechanisms which may flatten, roll or extrude the metal into its final shape. Casting machines are designed to be billet, bloom or slab casters. Just a final note to strip casting, which has been pioneered for steel and other metals in low-production markets in order to minimize the amount of rolling required.

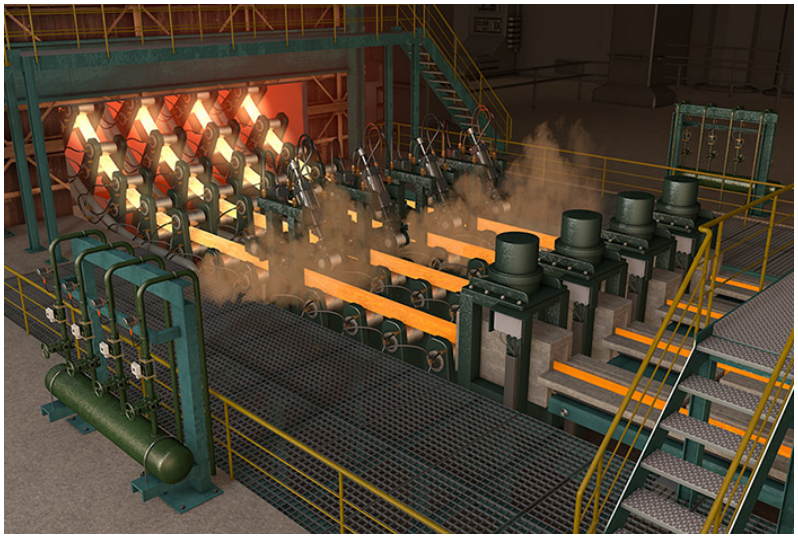

Fig. 1.2: Final section of *curved apron* casting process. Water is sprayed on hot metal during secondary cooling, forming steam.

1.1.1 Chrystal growth and dendrites formation

Controlling the solidification process of metal is essential along the casting line; in fact, the formation of nino-sized crystallites from molten metal determines its solidification structure, thus quality of the final cast product. Solidification means the transformation from liquid phase to the solid one; the initial stage of this transformation is called *nucleation* and it refers to the moment when *nuclei*, solid particles, generate from the liquid phase. At the thermodynamic freezing temperature, the probability of forming stable, sustainable nuclei is extremely small; therefore, solidification begins when liquid cools just under nominal solidification temperature because energy associated with the crystalline structure of the solid is less than the energy of the liquid. Energy difference between liquid and solid phase is the "free energy" per unit volume; it generates the unstable thermal condition necessary for activating the solidification process. Atoms start to cluster together and a solid-liquid interface is generated on the surface of particles they make; their free surface is associated with a certain energy, depending of particles' dimension (volume and surface) and influencing particle' stability during its growth: when particle's radius overcomes the *critical radius*, it becomes a nucleus and it starts collecting further atoms growing in solid, stable particles called *crystals*. Then they attach and cluster forming *grains*. Crystals increase in size by the progressive addition of atoms and grow until they impinge upon other adjacent growing crystal; their final individual size depends on the number of nucleation points. Grains evolve into *compact grains* or *dendrites* and the structure of both of them depends from thermal and flow conditions in the solidification zone, defining the following crystallographic structure of the solid.

Crystal growth, in the both cases of compact grains and dendrites, can develop into two major types of grain structures:

- *equiaxed grains*, made of crystals growing almost equally in all directions. They are common adjacent to a cold mold wall; and
- *columnar grains*; they are long, thin, coarse grains, created when metal solidifies rather slow in the presence of a steep temperature gradient. Columnar grains grow almost perpendicular to mold' surface.

Dendritic solidification

The term dendrite comes from Greek word *dendron*, which means tree. In metallurgy, dendrites have a characteristic tree-like branching structure; their shape is produced by faster growth along energetically favourable crystallographic directions and their growth has strong consequences in regard to material's mechanical, electrical and chemical properties. Dendritic crystalline growth occurs when the liquid-solid interface moves into a super cooled liquid whose temperature falls in advance of interface while heat is being removed. When the solidification process starts, heat of fusion is released at the interface, rising its temperature above the both liquid and solid; temperature drop on the direction from the interface into the solid is generated, thus temperature gradient inverts because of the heat flow direction. When temperature falls in the liquid in advance of the interface, the latter becomes unstable and solid particles then find favourable conditions for rapidly advancing through the liquid phase, generating the characteristic tree-like branching structure (difference between columnar Fig.1.3 and equiaxed Fig.1.4 grains can be noticed in pictures below).

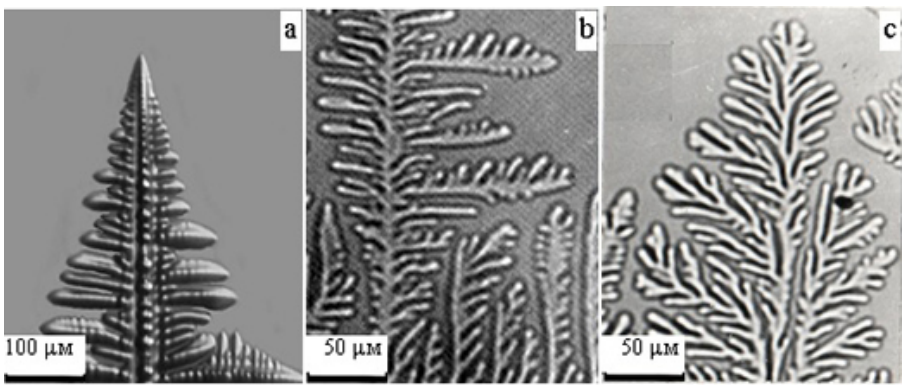

Fig. 1.3: Dendrites characteristic tree-like branching structure. Their columnar shape can be noticed in all of the images.

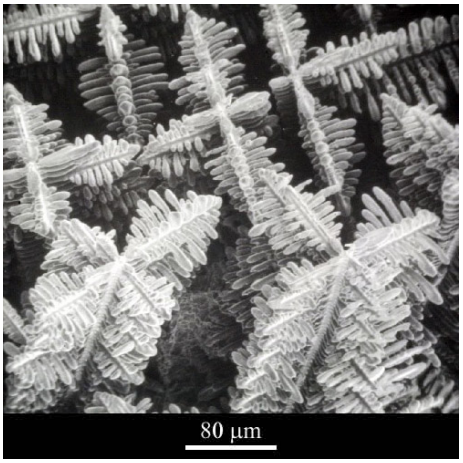

Fig. 1.4: Equiaxed dendrites. Their four branches have almost the same dimension.

Dendrite's generation represents the best way for grains to consume the heat of fusion and the faster this process happens, the more dendrites brunch. Their microstructural length scale is determined by balance between surface energy and temperature gradient in the liquid at the interface. Specifically, fast cooling determines the formation a higher number of nuclei and smaller dendrites' dimension, due to bordering growing crystals; smaller dendrites generally lead to higher ductility of the product. Slower cooling process produces bigger dendrites.

1.1.2 Limits of the casting line

Initial solidification is governed by conduction of heat through the mould but the heat flow is complicated by thermal stress, which bends the shell, and nucleation undercooling, which accompanies the rapid solidification and controls the initial microstructure. Further solidification is governed mainly by conduction and radiation across the interfacial gap between the solidifying shell and the mould. This gap consists mainly of mould flux layers, which move down the mould at different speeds. It is greatly affected by contact resistances and shrinkage and bending of metal shell, which may create an air gap. These phenomena must be controlled during the shell growth because of their influence on defects in the final cast product, like crack formation in the mould due to thermal stress and mould friction. Furthermore, strong deformations occur after the strand exits the mould, because of strong temperature fluctuations, which can produce strong change in the ductility and strength of metal, plus crack propagation. The final step of the solidification and cooling process produces macrosegregation and large composition differences of the final product could arise.

Quality of the final cast product is strongly influenced by a few limits and natural

behaviour of the solidifying metal, which must be taken into account along the casting process (Fig.1.5):

- composition variation within a solidified product is known as *segregation*. Segregation in an alloy is a result of solute rejection at the solidification front followed by its redistribution by diffusion and mass flow. It can also be produced by density changes due to phases transformations, temperature and compositional changes. In few other cases, smelting and refining operations do not completely eliminate all of the impurities which are usually contained inside liquid metals chosen for casting processes; it is possible for them to be trapped inside the liquid metal; this leads to segregation of solute elements in finished casting too. Depending on the extension of composition variation, this defect is classified as *macrosegregation*, relative to grain scale, or *microsegregation*, relative to the product scale. The former is due to the accumulation of rejected solute by transport over long distances through the casting or to motion of growing crystals from their nucleation sites from gravity or turbulence and long-range capillary flow of liquids during the final stages of the cooling process. It corresponds to large composition difference between the surface and the centre of the casting, which cannot be affected by diffusion, as the distance is too large. Hot working procedure breaks down the cast macrostructure enabling the composition to be evened out. Microsegregation (also known as *interdenditic segregation* or *coring*) results from accumulation of the rejected solute between growing crystals and its failure due to either inadequate time to diffuse into the main body of residual liquid; microsegregation of alloying elements and impurities effects strength and ductility. It occurs over short distances over micron length scale. Homogenization, which involves heating the material just below the non-equilibrium solidus and holding it there for a few hours, reduces microsegregation by enabling diffusion to bring the composition back to equilibrium. Notice that segregation is influenced by the mass movement of precipitated phases, due to the difference in density compared with their parent liquid; metal crystals growing independently in the melt tend to sink and produce a corresponding upward displacement of solute enriched liquid. Gravity effects segregation process too: crystals which form freely in the liquid often have a different density from that liquid; as a result, they may either rise towards the surface of the casting or settle towards the bottom.

- *breakouts* have already been mentioned and they represent the main difficulty that may occur during the solidification of metal. The solid shell of the strand breaks

and allows the still-molten metal within to spill out and foul the machine. In most industrial environments this event is very costly as it leads to a shutdown of the strand and typically requires to stop the production for removing the spilled material and replacing the damaged machinery. A breakout is usually due to the shell wall being too thin to support the liquid column above it. This condition is due to different causes often related to heat management: improper cooling water flow into the mould or strand zone may lead to inadequate heat removal from the solidifying metal and cause the solid shell to thicken too slowly. If metal withdrawal rate is too fast, the shell may not have time to solidify to the required thickness even with stronger cooling sprays. Furthermore, when the incoming liquid metal is too hot, its final solidification point may occur further down the strand at a later point than expected; if this point is below the straightening rolls, the shell may break from stresses applied during straightening. Breakouts can also be the result of excessive turbulence within the mould, which may produce irregular shell pattern, that grows abnormally, or may reduce shell strength. A common event is for the shell to stick to the surface of the mould and tear; modern control systems applied to the casting line typically detect this fact and slow the caster down temporarily to let the wall refreeze while it is still supported in the mould. Anyway, should the incoming metal be severely overheated, failing in a breakout again is almost certain; in this case it may be preferable to stop the caster than to risk a breakout. Additionally, possible contamination of the metal in the initial charging step could determine the generation of a thin film between the mould wall and the metal, limiting cooling efficiency and increasing the risk of breakouts.

- *contamination* of metal before or during the continuous casting produces serious problems to the process and in most case the rejection of the final cast product. Oxidation is maybe the most common way through which hot metal may become dirty and it occurs rapidly at molten metal temperature (up to 1700 [°C] for steel); inclusions of gas, slag or undissolved alloys may be also present. Prevention from oxidation consists in isolating metal from the atmosphere as much as possible: exposed liquid metal surfaces are covered by synthetic slag in ladle, tundish and mould. The same slag layer may also trap any inclusion that is less dense than the liquid metal, such as gas bubbles, oxides or undissolved alloys; in that case, items produced from badly contaminated liquid are typically quarantined or sold as bad-quality products.

- Another problem that may occur is *carbon boil* - oxygen dissolved in the steel reacts with carbon inside metal and generates bubbles of carbon monoxide. The reaction

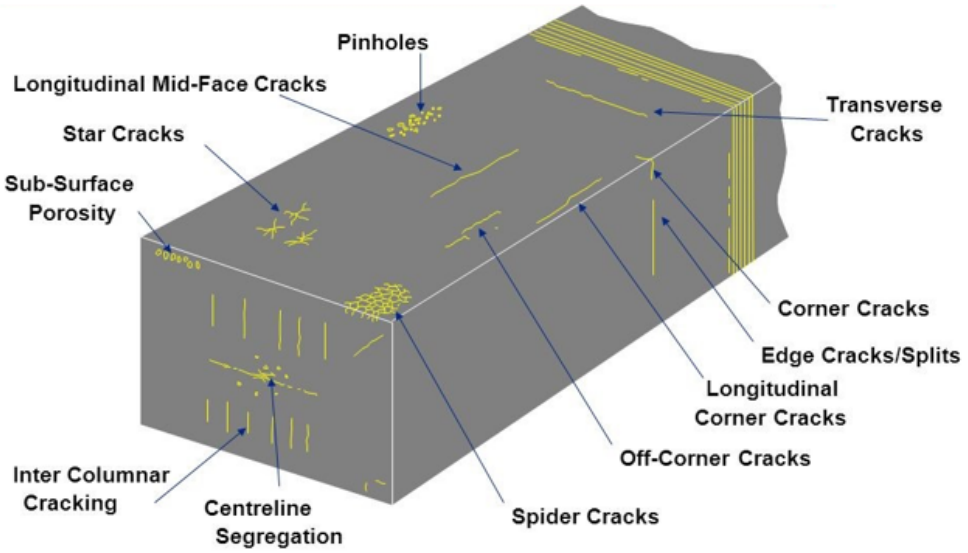

Fig. 1.5: Main defects of the casting process

is extremely fast and violent and it generates large amounts of hot gas. When steel is the cast metal, oxygen is removed by "killing" it, through the addition of silicon or aluminium to steel and the consequent reaction which forms silicon oxide (silica) or aluminium oxide (alumina); a perfect quantity of silicon or aluminium is fundamental for achieving good quality of the final product. Computational fluid dynamics and other fluid flow techniques are being extensively used in the design of new continuous casting operations, in the tundish especially, to ensure that inclusions are removed from the hot metal and finally ensure that all the hot metal reaches the mold before it cools down too much. Slight adjustments to the flow conditions within the tundish or the mold mean the difference between the high and low rejection rates of the product.

- *Argon injection* into the nozzles is adopted top prevent clogging; resulting bubbles from the injection strongly affect flow pattern of molten material, both in the nozzle and in mold. Inclusions could be then collected inside the metal and they could be entrapped into the solidifying shell, leading to serious defects on the surface of the final product. In the end, quality of the final cast product is strongly influenced by velocity of the injected gas: the higher velocity, the higher risk for metal to entrap gas inclusions in the solidifying shell.

- *hot cracking* (also known as *hot tears*) produces failures in the casting that occur as the casting cools. This happens because the metal is weak when it is hot and the residual stresses in the material can cause the casting to fail as it cools. Proper mold

design prevents this type of defect. Hot spots are areas on the surface of casting that become very hard because they cooled more quickly than the surrounding material. This type of defect can be avoided by proper cooling practices or by changing the chemical composition of the metal.

1.1.3 Influence of intensive melt flow on the solidifying structure

The principle of casting line is based on a solidification process which includes together a solid-plus-liquid (*mushy*) zone, formed between the solid skin and liquid pool. Once metal solidifies, three different resulting patterns can be recognized for its internal structure (see Fig.1.6): a) pure metals are characterized by *chill grains* on the external surface and columnar grains which grow towards the centre; b) alloys are made of a small layer of chill grains, then columnar grains and finally a core of equiaxed grains; c) completely equiaxed structure can be achieved by heterogeneous nucleation of grains using nucleation agents. Tha chill zone is named so because it occurs at the walls of the mold where the wall chills the material; here is where the nucleation phase and solidification process takes place. As more heat is removed, grains grow towards the centre of the casting.

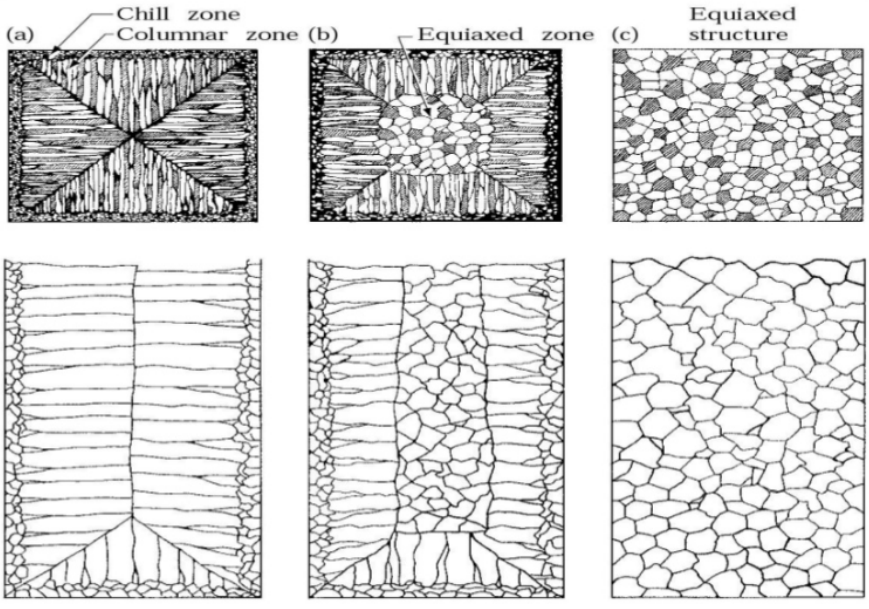

Fig. 1.6: Different solidification patterns of the cast product. Above: horizontal section, orthogonal to the length of the cast metal; below: vertical section

Size and shape of grains of the cast are crucial parameters: thin, long columns are perpendicular to the casting surface and they are undesirable because of their anisotropic properties; on the other hand, equiaxed grains have isotropic properties and smaller size.

They mean finer structure, higher ductility and more uniform grain distribution, thus improving the homogeneity of material properties and its mechanical qualities. In the absence of grain-refining additions to a melt or of heterogeneous nucleation, equiaxed grains can only originate in a casting from primary dendrite fragments. Microstructure of the solidified metal can be influenced with the application of intense motion to the liquid, in order to interfere with its flow pattern. Temperature and chemical components homogenization can be obtained in the liquid volume, plus intensification of heat and mass transfer. Furthermore, strong motion forces the solid-plus-liquid mixture to stay fluid for much higher solid fractions, affecting both shape and dimension of growing grains; it produces *dendrite fragmentation* and grain multiplication, which lead to the transition from columnar to equiaxed grains and a substantial reduction in their size. Fragmentation is not a fracture but a local remelting process [35]; stress produced by turbulences change the local equilibrium at the solid-liquid interface and dendrite side arms detach from the main trunk generating further nucleation points (Fig.1.7 and 1.8). Molten metal flow also rises the temperature of molten steel at solidification interfaces and accelerates re-melting of the dendrites, thus making it possible to solidify metals at lower temperatures compared with in conventional practice. The intensity of fluid motion must be carefully balanced: if the velocity is not sufficiently high, the growth of columnar dendrites does not stop; once started, turbulences must be applied continuously, especially in the lower levels of the strand. A liquid-solid mixture once in motion remains in fluid even when it contains up to 60% solids; but if it stops moving, its viscosity increases rapidly and the mixture behaves as a solid. Extraordinary amounts of power would be required to set in motion the mixture again. On the other hand, if fragmentation is too strong, too small dendrites broken arms and no equiaxed grains can be generated; weak cast materials are produced, with undesired mechanical properties which can lead to rejection of cast products. In specific cases (pure metal processes or turbine blades production), dendrite fragmentation is not desired because of branched crystals too fragile in the solidified metal.

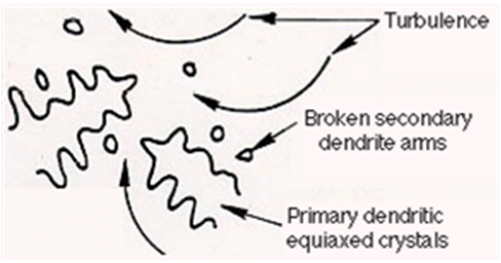

Fig. 1.7: Simple scheme of dendrite fragmentation mechanism

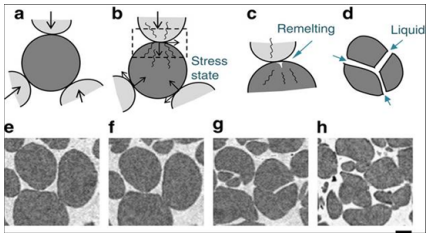

Fig. 1.8: Fragmentation is not a fracture but a local remelting

1.2 Methods of stirring for grain refinement

Intensive melt flow in continuous casting is always produced from *stirring action* on molten material. This solution leads to the microstructure and composition homogenization of the cast product, affecting its inner and surface quality. Industrial experience has shown that stirrer design and operating conditions have a strong influence on metallurgical quality. Thus, different technologies of stirring (Fig.1.9) for grain refinement can be distinguished:

Mechanical Stirring

Mechanical stirring is achieved using augers, impellers or multiple agitators that are attached to a rotating shaft. The advantage of mechanical stirring is that torque and rotational speed can be recorded during stirring and used in real time for determining the fluid viscosity as well as for process control. Mechanical stirring can be subdivided into active and passive techniques according to how shear is induced in the melt. Stirring with propellers is one of the most common method; the impeller always includes two or more blades, specifically designed for generating toroidal vortices inside the liquid. The impeller is driven by an electric motor; it is commonly set in the central axis of the cast and its rotating velocity can be regulated while a constant torque is usually desirable in stirring applications. Japanese experiments [25] show that impeller diameter plays a significant role on mixing patterns inside the melt: larger diameter generates vortices on a deeper position, making the mixing more effective.

Mechanical stirring spread in many industrial and experimental applications for reducing gas contents inside solidified metals; desulfurization for example is a fundamental process for steel and it is achieved with the help of mechanical stirring; in some experimental activities, stirring action is combined with the injection of different materials like powder or plastics [24]. Even if the structure of actual mechanical stirrers is getting more compact and simple, many delicate components are still necessary for the apparatus; the propeller is drawn inside the fluid, thus the two of them keep directly in contact during the whole stirring process, affecting purity of the solidified product. Really intense motion is generated with such a kind of stirring and large volumes can be processed.

The combination of mechanical stirring with vertical semi-continuous casting process [36] showed that fine structure and uniform distribution of particles can be achieved with high rotational speed and high castiong temperature but these stirring conditions also lead to transverse cracks on the billet surface.

Stirring with vibrations

Either sonic or ultrasonic vibrations produced by mechanical vibration elements can be applied during solidification to refine the microstructure. Such vibration is normally provided via magnetostrictive or piezoelectrive transducer. Contact between molten metal and transducer probe (normally made of titanium) is provided via a high-temperature material coupling (typically ceramic based). Some disadvantages are that it can only be applied to small volumes, extremely powerful machines must be used instead; the high-temperature coupling material may dissolve with time when immersed in the liquid metal where it may also contaminate the melt.

Low frequency (*i.e.* in the range of [Hz]) or ultrasonic vibrations (*i.e.* in the range of [kHz]) can be applied: experimental activities [46] demonstrated that the former considerably reduces surface cracks and, in combination with water cooling systems, it produces more uniform cooling, increases the amount of nucleation and the sphericity of grains. The latter has been combined and applied after mechanical stirring to agitate the insoluble solid nanoparticles and promote more nucleation. Recent experimental activities [37] tested the Multi-frequency Multimode Modulated (MMM) technology in the challenge of increasing stirring efficiency and degassing; the goal of this technology is to fully agitate the whole vibrating system thanks to the combination of sonic and ultrasonic driving, which produces multimode vibrations which are uniform and repeatable.

Stirring by gas injection

Stirring by means of gases does not apply any mechanical movement directly to the fluid but motion is achieved thanks to gas injection inside the melt (*argon* is usually the gas chosen for this process). Gas is blown through nozzles fixed on the top or bottom position of the melt and more than one blowing tube can be present. This solution does not allow rapid neither exact control of flow velocity but strong motion can be generated. Big volumes of material can be stirred but contamination of the cast is very easy, because of pipes inside the liquid which could interact with it and because of possible gas bubbles being trapped inside the solidified material, which strongly decrease its quality. Gas stirring has also a cooling effect on the melt and increases the rate of oxidation. A study form ABB [38] puts in evidence that gas stirring technology is made of different moving tools (in the same way of mechanical and vibrating stirring) which reduce reliability of the process: the gas supply line must be connected to the ladle, automatically or manually, and disconnected after treatment; connections and joints in the supply lane may leak and the flow meter will give false information. Therefore it is necessary to inspect the system to make sure the required stirring action is delivered. Furthermore, the presence

of a gas plug in a ladle lining always represents a potential risk; any break through is very costly and increases the risk of personal injuries. On the other hand, stirring through gas injection plays a significant role in steelmaking processes, in the ladle especially, thanks to its strong mixing action.

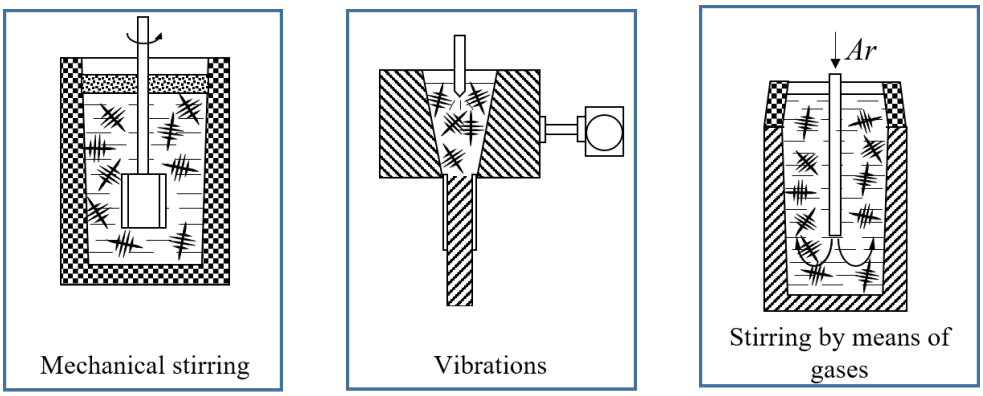

Fig. 1.9: Different methods of stirring

Electromagnetic stirring

Electromagnetic stirring (EMS) is based on the concept the electric motor: when the coil surrounding molten material is fed by an alternating current (single-phase or three-phase usually), the produced magnetic field penetrates inside the liquid metal and induces electric current inside of it (it is also called *eddy current*); interaction between magnetic field and induced currents produces a certain distribution of electromagnetic force, which determines liquid metal motion with a certain flow pattern. Therefore, it is easy to notice how the stirring device makes the role of the stator of an electric motor while liquid metal represents the rotor. Generated force is named *Lorentz force* (see equation 2.7) and it depends from four main factors:

- intensity of the supply current
- number of windings forming the coil
- frequency
- system's design.

Low frequency (*i.e.* few [Hz]) is always applied for generating deep-penetrating field and assure more uniform fluid's motion; on the other hand, other electrical and geometrical parameters strongly depend from stirring desired pattern and fluid's velocity which wants to be provided. Supply current directly influences velocity of the fluid, which is usually included in a range of $0.1 \div 1$ [m/s].

Three possible stirrer configurations in a continuous casting machine are present, according to the position and the required effects on the cast product (Fig.1.10):

- ***mold-electromagnetic stirrer*** (*M-EMS*) is usually installed in the immediately lower part of the mold for stirring the liquid metal at the very beginning of its solidification. It improves surface, sub surface and inner strand quality. M-EMS is either of round or square design and it can be installed internally or externally; it provides rotating magnetic field.

  In many industrial applications, in order to achieve flexible control of stirring speed in the mould meniscus, dual coil M-EMS has been developed; it consists of two independent EMS. The upper one is meant for flow control in the meniscus while the lower EMS performs the stirring of main metal in the mould. Such a design of dual M-EMS widens the opportunities for using the EMS technique under various conditions of continuous casting of metals.

- ***strand-electromagnetic stirrer*** (*S-EMS*) produces a stirring force that pushes the liquid steel horizontally along the cast product width and generates a butterfly type flow pattern in the liquid metal; travelling magnetic field is produced (Fig.1.11). It is placed at a certain distance from the meniscus where metal solid fraction is rapidly increasing. Low frequency ensures of the stirrer force through the strand. Stirrer device design determines transverse stirring effect, which is usually used in combination with M – EMS. Strand – EMS can be of either linear or rotary type; it is installed behind support rollers or into them; in this last case, bigger roller diameter is required and stirring action is less effective. Linear stirrer is easy to install and protect against heat radiation and possible breakouts, therefore it is really common. Strand-stirrer removes superheat effectively.

- ***final-electromagnetic stirrer*** (*F-EMS*); there is equally strong interest in using EMS to stir far below the mold in the final solidification zone of a continuous casting strand. However, conventional EMS systems have proven to be somewhat ineffective when applied in this region. As a potential solution, there recently has been considerable interest in applying modulated Lorentz forces in an effort to develop distributed vigorous stirring in the final zone. F-EMS is generally installed in combination with mold-EMS or strand-EMS to reduce and cut peaks in centre segregation. F-EMS is particularly efficient when casting high carbon or high alloy steel grades. With the use of F- EMS, solidification structure of the cast product is improved due to the increase in the ratio of the equiaxed structure. Shrinkage

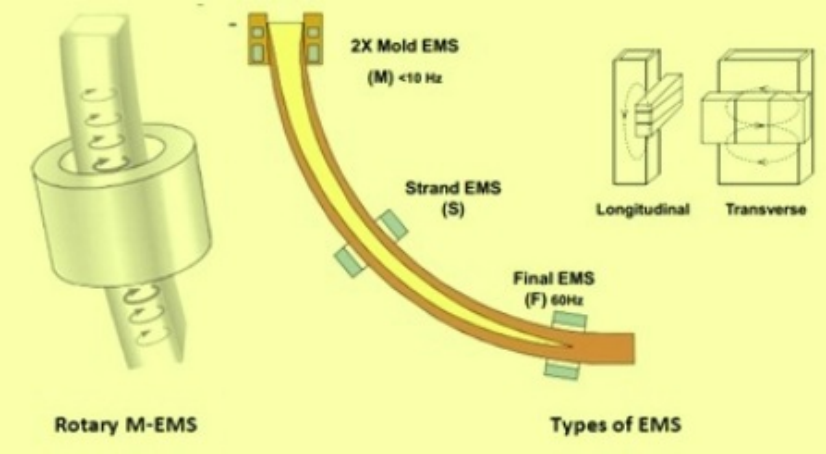

Fig. 1.10: Types of EM stirrers along the continuous casting line

and central segregation are reduced, enhancing the quality of the cast product at the end of its solidification process. Final electromagnetic stirrer provides rotating magnetic field.

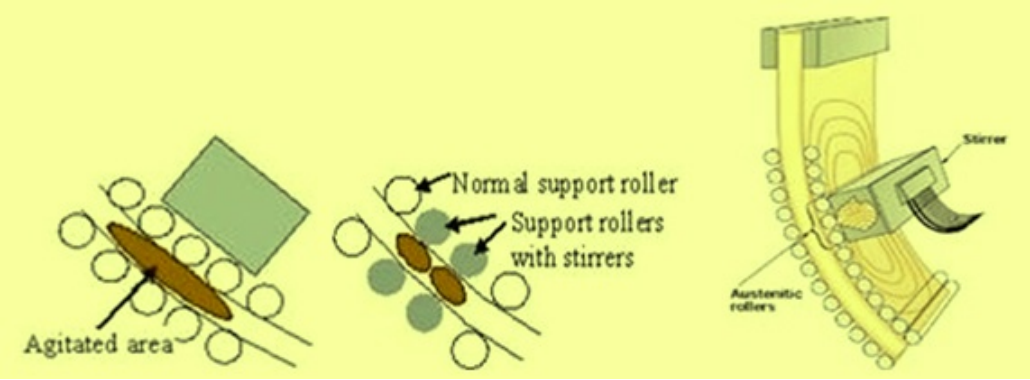

Fig. 1.11: Strand electromagnetic stirrer: location and design

All of the previous EM stirring systems are equipped with a transformer, frequency converter and a controller, to guarantee power supply and manage the electrical parameters like current, voltage and frequency; the frequency converter is specifically designed for operating with low frequencies involved with the stirring equipment.

The main element of each electromagnetic stirrer is represented by its coil, usually made with copper or aluminium; EM stirrers for continuous casting lines also include magnetic core to guide magnetic field lines, a shielding and cooling system for protecting the device from hot temperature of molten metal. It is easy to notice that electromagnetic stirrers have simple and compact design which permits no direct contact with the liquid, this is a significant advantage, considering the aggressiveness of liquid metals. The magnetic field acts as a non intrusive stirring device, thus not affecting purity of the

cast material. No moving parts are present, making the system more reliable, reducing its maintenance costs and increasing leaning life of the casting line. Induction systems always assure low energy consumption, thus high efficiency; the high initial cost of stirrer's installation and immediate price of current are always supplied by an attractive pay-back time. Great flexibility has recently been achieved thanks to the development of solid-state power converters. EM stirring process can be easily and instantaneously controlled: intensive melt flow is always produced and flow pattern can be modified by changing magnitude and frequency of the supply current to the coil. Thanks to different inductors' design, different kinds of magnetic fields can be generated inside the melt (Fig.1.12), thus affecting its motion:

a. ***travelling magnetic field*** (*TMF*) moves along the same direction of the casting line and is generated by three-phase inductor surrounding molten material. Resulting Lorentz force produces a unique, toroidal vortex inside the melt, whose dimension can be varied with the change of the supplied current. Intensity of the flow and its direction can be controlled precisely while intensive heat and mass transfer are absent in the central zone of melt volume.

b. ***rotating magnetic field*** (*RMF*) is produced by single or three-phase stirrers when their inductor is made of single groups of coils fixed around the casting line. Two main flow patterns are generated inside molten metal: the first, and the principal one, is melt's rotation around its axis while two secondary toroidal vortices are generated next to the top and the bottom of stirrer device.

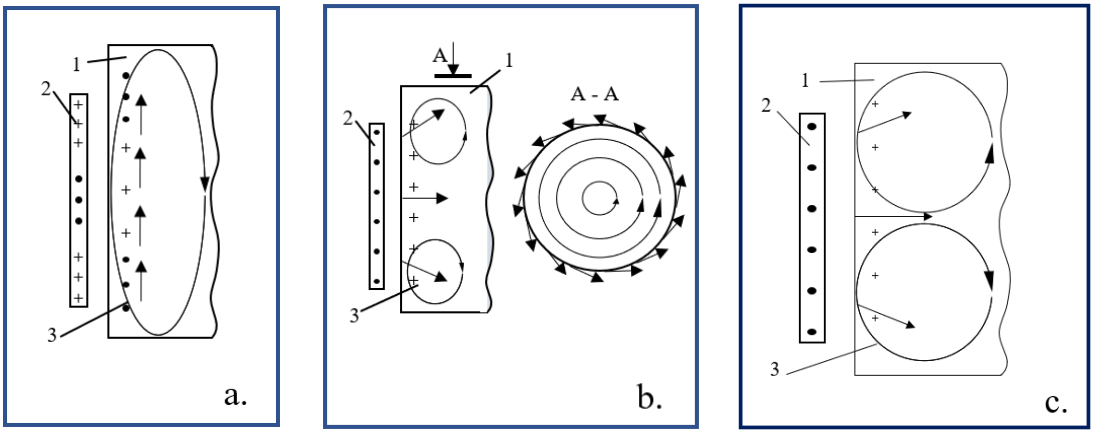

Fig. 1.12: Flow patterns produced by different magnetic field solutions (a. travelling magnetic field; b. rotating magnetic field; c. alternating magnetic field). In every picture it is possible to recognize 1- flowing molten metal, 2- inductor and 3- flow pattern of the liquid. No magnetic field lines have been represented while induced currents are in evidence with + or • symbols

c. ***alternating magnetic field*** (*AMF*) is generated by a coil around the fluid and motion of liquid metal is represented by two toroidal eddies which have almost the same average velocity and energy but opposite directions; the two vortices are symmetrical to the centre of the inductor. At the difference of other configurations, AMF assures intensive heat and mass transfer between vortices, in the central zone of melt volume. The intensity of the flow can be controlled only while flow pattern is obviously fixed for each magnetic field solution.

1.2.1 Stirring with AMF or PMF: objectives of this investigation

Investigation setup chosen for this thesis adopted AMF for stirring liquid metal, GalIStan in this specific case. AMF is the most applied stirring solution for continuous casting, thanks to the production of more intense motion compared with other methods, its strong possibility to increase equiaxed ratio of dendrites and intensive heat transfer, which brings to high homogenization of and thermal properties. This solution can also be easily and rapidly controlled. The inductor is always fixed at the beginning of the casting line,

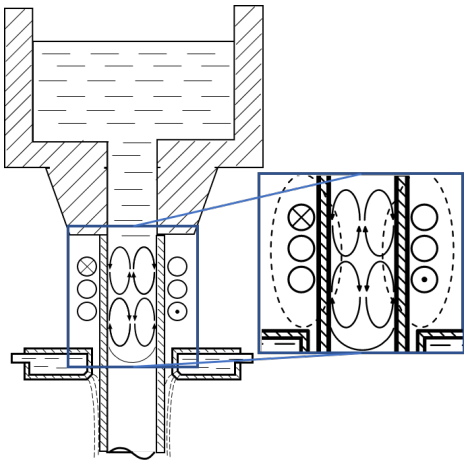

Fig. 1.13: Mould-EMS generating AMF.

below the mould but immediately before first cooling step, where the meniscus generates (Fig.1.13). This area (named *meniscus area*) significantly affects the quality of CC ingot and its surface especially [40], thus the final product. As already stated, standard configuration is not influenced from the solidification front and two similar toroidal eddies are produced in a symmetrical position with the coil; frequency of the current feeding the stirrer is low (*i.e.* less than 10 [Hz]) and sinusoidal current is almost always adopted. Previous studies on this symmetrical configuration [23] demonstrated that motion of melt can be significantly increased with pulsed magnetic field (PMF) solution instead of AMF: amplitude and rotating frequency (*characteristic frequency*, f_{ch}) of vortices were calculated,

thus alternated current was substituted with pulses with the same frequency of eddies (*pulsed frequency*, f_p); each pulse was made anyway with sinusoidal waves with f_{ch} and lasted for half of the *pulsed period*, T_p. Main aim of this investigation was to achieve strong interaction between electromagnetic and mechanical parameters, thus ***resonance*** of current supplied to the coil with the two toroidal eddies. In this case, ***higher efficiency*** of the stirring process was evidently obtained, which can lead to two main consequences:

1. more intense motion of the liquid metal with the same amount of supplied electrical power;

2. same intensity of motion with less supplied electrical power.

PMF solution interacted with pulsed component of velocity of the flow and the investigation also demonstrated that strong motion of melt was achieved not with resonance frequency f_p only but with the application of a frequency around resonance too (Fig.1.14 shows in the red circle resonance consequences when frequency was around f_p).

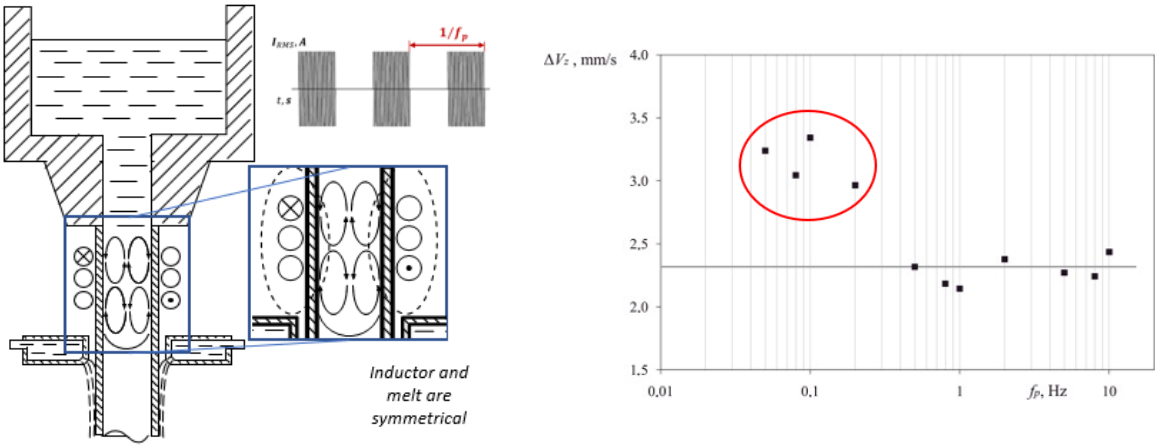

Fig. 1.14: Investigation results for PMF application. Diagram on the right shows the intensity of pulsed component of velocity over frequency variation of current. Pulsed current can be noticed above the stirring system.

Main objective of this thesis was to carry on with the previous investigation and apply PMF solution instead of AMF in the case of not standard stirring conditions (Fig.1.15): global knowledge of meniscus area is fundamental to optimize the action of stirrer on molten metal and the meniscus is commonly located at the same height of solidification zone; in some industrial casting applications thought, movement of meniscus can occur, thus relative position between melt and inductor is not symmetric anymore and strong asymmetry between toroidal eddies can be observed too. This working condition brings to a transition from two similar vortices in amplitude and velocity, to the generation of

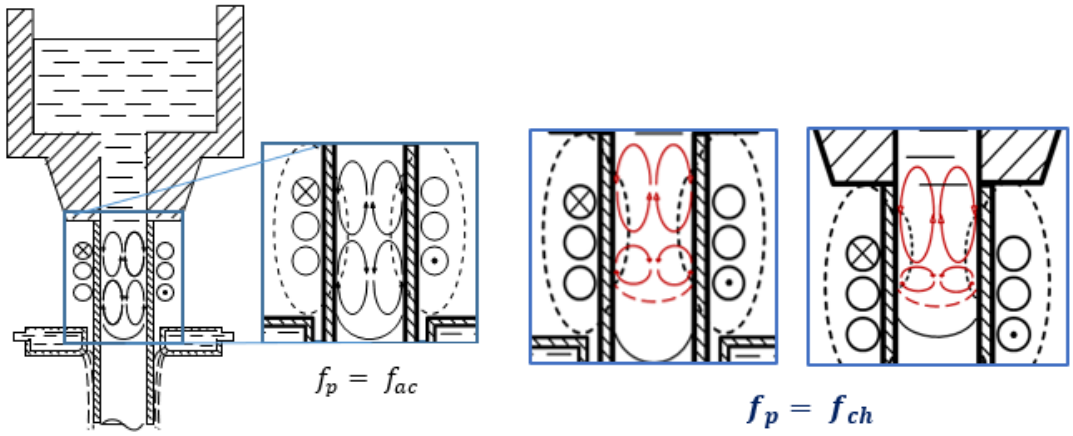

Fig. 1.15: Schematic representation of *two-to-one transition*.

a couple of vortices in which one of them is much bigger and energetic than the other; ***two-to-one transition*** is due to two main causes:

- strong asymmetry between melt and the surrounding inductor. This condition is the topic of this investigation and is determined from strong cooling rate, which increases speed of solidification.
- decrease in the ratio $height/diameter$ of melt, thus movement of relative position of metal liquid phase respect to the coil.

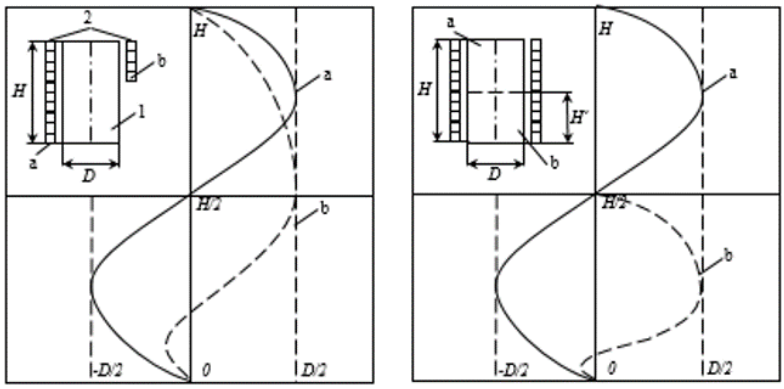

Fig. 1.16: Causes of the transition. Curve *a* refers to velocity profile in symmetrical conditions, curve *b* is the one after symmetry is lost.

This thesis focused on the region where stirrer is located in order to investigate consequences of the transition on melt flows and the possibility to optimize stirring action in such conditions. Firstly, ***if*** the transition happened was investigated, then ***when*** it occurred was analysed, with the objective to apply PMF with the same frequency of bigger vortex and achieve resonance condition, thus higher efficiency even during the shift of

solidification front. Simulation of the transition was carried out with a 6-turns inductor surrounding melt with cylindrical shape; relative movement between the two of them was realized with shifting upward the coil, while axial component of flows velocity was measured to quantify motion of melt. Chosen molten metal for the investigation was GalInStan. AMF was initially applied during inductor's movement, then the transition was analysed and finally optimization of the stirring effect was achieved with the application of PMF.

Chapter 2

Theoretical background

2.1 Electromagnetic systems and their numerical modelling

The present work deals with liquid metals flows, driven by electromagnetic forces. These kind of flows are often observed in various metallurgical processes of different scale: from experimental centimetre-sized installations for melting of high-purity alloys, up to industrial furnaces with several meter in diameter. All of the previous systems share the fact that melt moves in closed domain, with no inlets and outlets and this domain keeps a relatively stable form for the considered period of time. When an alternating harmonic electric current $i(t) = I_{max} \sin(\omega t + \phi)$ feeds the inductor, energy is supplied to the system and generates fluid's motion. Magnetic field is induced by the current into the melt and spreads according to Maxwell's equations:

$$\nabla \cdot \mathbf{E} = \frac{\rho_e}{\varepsilon} \qquad \text{(Gauss' law)} \tag{2.1}$$

$$\nabla \cdot \mathbf{B} = 0 \qquad \text{(Gauss' law for magnetism)} \tag{2.2}$$

$$\nabla \times \mathbf{E} = -\frac{\partial \mathbf{B}}{\partial t} \qquad \text{(Faraday's law)} \tag{2.3}$$

$$\nabla \times \mathbf{B} = \mu \left(\mathbf{J} + \varepsilon \frac{\partial \mathbf{E}}{\partial t} \right) \qquad \text{(Ampere's law)} \tag{2.4}$$

where $\mu = \mu_r \mu_0$ is the product of relative permeability of the material and the permeability of free space and $\varepsilon = \varepsilon_r \varepsilon_0$ is the permittivity. All of the equations above have thus be

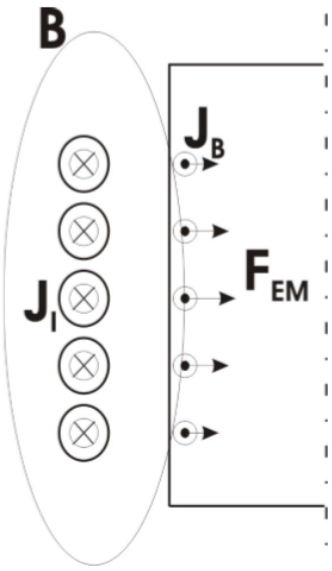

Fig. 2.1: Scheme of an axisymmetric induction system

taken into account in their general case, where ρ_e is the total electric charge density; from now on, the specific case of no free electric charges in the domain $\rho_e = 0$ will be taken into account and equation (2.1) becomes $\nabla \cdot \mathbf{E} = 0$. The following expressions will be written in free space. The set of Maxwell's equations is completed by:

$$\nabla \cdot \mathbf{J} = 0 \qquad \text{(Charge conservation)} \tag{2.5}$$

$$\mathbf{J} = \sigma(\mathbf{E} + \mathbf{v} \times \mathbf{B}) \qquad \text{(Ohm's law)} \tag{2.6}$$

$$\mathbf{f}_{EM} = \mathbf{J} \times \mathbf{B} \qquad \text{(Lorentz force)} \tag{2.7}$$

and by *constitutional equations*:

$$\mathbf{J} = \sigma \mathbf{E} \tag{2.8}$$

$$\mathbf{D} = \varepsilon_0 \mathbf{E} \tag{2.9}$$

$$\mathbf{B} = \mu_0 \mathbf{H} \tag{2.10}$$

The divergence of magnetic induction field **B** is always equal to zero (2.2) and therefore a magnetic vector potential **A** can be introduced:

$$\mathbf{B} = \nabla \times \mathbf{A} \tag{2.11}$$

Using Faraday's law (2.3), electric field intensity can now be expressed as:

$$\nabla \times \mathbf{E} = -\nabla \times \frac{\partial \mathbf{A}}{\partial t} \tag{2.12}$$

Integrating this expression, leads to:

$$\mathbf{E} = -\frac{\partial \mathbf{A}}{\partial t} - \nabla \varphi, \tag{2.13}$$

where the last term on the right represents the integration constant and a new scalar term is introduced - the electric vector potential φ. The equation for vector potential **A** can be achieved by substituting equations number (2.11), (2.13) and (2.3) into the equation number (2.6) and by neglecting displacement current $\mathbf{J} \gg \varepsilon_0 \frac{\partial \mathbf{E}}{\partial t}$:

$$\frac{\partial \mathbf{A}}{\partial t} = \lambda_m \nabla^2 \mathbf{A} - \nabla \varphi + \mathbf{v} \times \nabla \times \mathbf{A} \tag{2.14}$$

Here the magnetic vector potential was derived using the Coulomob gauge $\nabla \cdot \mathbf{A} \equiv 0$, i.e. in divergence-free form and therefore using the nabla formalism the next expression is correct: $\nabla \times \nabla \times \mathbf{A} = \nabla(\nabla \cdot \mathbf{A}) - \nabla^2 \mathbf{A} = -\nabla^2 \mathbf{A}$. Parameter $\lambda_m = 1/\mu_0 \sigma$ is called *magnetic diffusivity*. The last term of (2.14) is usually negligible because of its insignificance in the examinated flows. Displacement current is negligible in the hypothesis of slow varying and periodic fields with frequency up to 10 [kHz]; more precisely, deciding whether displacement current can be neglected or not depends from the wavelength of electrical quantities in the frequency domain: in the case it is large compared to physical dimensions of the problem, displacement current can be neglected. In this condition, we talk about ***quasi-stationary*** fields and most of the electrical engineering issues can be described with quasi-static phenomena. When $\partial D/\partial t \approx 0$, Ampere's law (2.4) can be written as:

$$\nabla \times \mathbf{H} = \mathbf{J} \tag{2.15}$$

and **A** formulation can be derived for quasi-stationary magnetic fields in time-domain:

$$\nabla \times \left(\frac{1}{\mu_0} \nabla \times \mathbf{A} \right) + \sigma \frac{\partial \mathbf{A}}{\partial t} = \mathbf{J} \tag{2.16}$$

Taking into account Coulomb gauge condition $\nabla \cdot \mathbf{A} = 0$, the equation above becomes:

$$\nabla^2 \mathbf{A} - \mu_0 \sigma \frac{\partial \mathbf{A}}{\partial t} = -\mu_0 \mathbf{J} \tag{2.17}$$

and the resulting equation is function of magnetic vector potential **A** only.

In a phasorial domain partial derivative $\frac{\partial \mathbf{A}}{\partial t} = j\omega \mathbf{A}$; thus, Ampere's equation (2.17) can be rewritten as:

$$\nabla^2 \mathbf{A} - j\omega \mu_0 \sigma \mathbf{A} = -\mu_0 \mathbf{J}. \tag{2.18}$$

In the most general case displacement current is not negligible from equation (2.4), thus magnetic vector potential and its properties can be substituted in equation (2.4):

$$\nabla \times \nabla \times \mathbf{A} = \mu_0 \mathbf{J} + \mu_0 \varepsilon_0 \frac{\partial \mathbf{D}}{\partial t} \tag{2.19}$$

$$\nabla \left(\nabla \cdot \mathbf{A} \right) - \nabla^2 \mathbf{A} = \mu_0 \mathbf{D} + \mu_0 \varepsilon_0 \frac{\partial \mathbf{D}}{\partial t}. \tag{2.20}$$

The use of constitutional equation and substitution of (2.13) inside (2.20) brings to:

$$\nabla \left(\nabla \cdot \mathbf{A} \right) - \nabla^2 \mathbf{A} = \mu_0 \mathbf{J} - \mu_0 \varepsilon_0 \nabla \frac{\partial V}{\partial t} - \mu_0 \varepsilon_0 \frac{\partial^2 \mathbf{A}}{\partial t^2}; \tag{2.21}$$

assuming Lorentz condition $\nabla \cdot \mathbf{A} = -\mu_0 \varepsilon_0 \frac{\partial V}{\partial t}$:

$$\nabla^2 \mathbf{A} - \mu_0 \varepsilon_0 \frac{\partial^2 \mathbf{A}}{\partial t^2} = -\mu_0 \mathbf{J}. \tag{2.22}$$

Using constitutional equation and substitution of (2.12) inside Gauss' law (2.1) brings to:

$$\nabla^2 V - \mu_0 \varepsilon_0 \frac{\partial^2 V}{\partial t^2} = -\frac{\rho}{\varepsilon_0}; \tag{2.23}$$

Equations (2.22) and (2.23) take the name of ***non homogeneous wave equations***; In addition to Lorentz condition, they are equivalent to the set of the four Maxwell equations and they are valid anywhere. It is finally possible to notice the appearance of an unknown function, multiplied by μ_0 and ε_0, on the left side, while the known source appears on the right side.

Considerable magnetic field penetrates into the melt in the depth of skin layer only; the skin depth shows how deep the magnetic field diffuses into the conducting medium and it depends on λ_m coefficient and on frequency of the electromagnetic field:

$$\delta_{em} = \sqrt{\frac{1}{\pi f \sigma \mu_r \mu_0}} \tag{2.24}$$

Combinig Faraday's law (2.3) and Ohm's law (2.6) together, induction equation can be obtained:

$$\frac{\partial \mathbf{B}}{\partial t} = \lambda_m \nabla^2 \mathbf{B} + \nabla \times (\mathbf{v} \times \mathbf{B}) \tag{2.25}$$

If the last term of the equation vanishes (the conductor motion is suppressed), the induction equation takes the same form of the diffusion equation and it can be shown that a magnetic field diffuses inwards by a distance of under $(2\lambda_m t)^{1/2}$ in a time t.

Lorentz force is extremely important for the conducting melt convection and motion inside stirrers of casting lines and in crucibles; it will be explained more in detail. Equation number (2.7) can be written using Ampere's law (2.4):

$$\mathbf{F}_{EM} = \frac{1}{\mu_0}(\nabla \times \mathbf{B}) \times \mathbf{B}, \tag{2.26}$$

which can be decomposed into a pressure term and a driving part:

$$\mathbf{F}_{EM} = +\frac{1}{\mu_0}(\mathbf{B} \cdot \nabla)\mathbf{B} - \nabla(\frac{\mathbf{B}^2}{2\mu_0}) \tag{2.27}$$

The first term of the right side in the above expression is the melt driving part (rotational) and can be written using index notation as $\partial m_{ij}/\partial x_j$, where $m_{ij} = (1/\mu_0)B_i B_j$ is the *Maxwell tensor*. The latter term represents the *electromagnetic pressure*, which, in form of gradient, can be included into the modified pressure in Navier-Stokes equation. This electromagnetic pressure therefore can change pressure equilibrium only and can cause free surface deformations in liquid domain.

If the magnetic field is harmonic $\mathbf{B} = \mathbf{B}_c \cos(\omega t) + \mathbf{B}_s \sin(\omega t)$, then the electromagnetic force can be decomposed into a mean (average) part and an oscillating part, where oscillating frequency is twice the electromagnetic field frequency. It can be illustrated on EM pressure term from the equation (2.27):

$$\frac{B^2}{2\mu_0} = \frac{1}{4\mu_0}({B_c}^2 + {B_s}^2 + ({B_c}^2 - {B_s}^2)\cos(2\omega t) + \mathbf{B}_c \cdot \mathbf{B}_s \sin(2\omega t)) \tag{2.28}$$

The mean part is responsible for the motion of the flow in its core while the oscillating part introduces surface instabilities and waves to the melt flow. However, the oscillating

part should be taken into account if the field frequency is very low only (about several Hz), because of inertia impeding the melt to respond to alternating forces at higher frequencies, which are typical for induction heaters. Some simulation experiments show that, for induction stirring problems, the flow is no longer sensitive to the oscillating part of Lorentz force when the applied magnetic field frequency exceeds approximately $5 \div 10$ [Hz]. Free surface deformation under the influence of electromagnetic pressure of (2.27) can be calculated with the help of the following equation:

$$\rho g z + \gamma K + \frac{\mathbf{B}^2}{2\mu_0} = const, \tag{2.29}$$

where first term on the left side represents hydrostatic pressure and $K = 1/R_1 + 1/R_2$ is equal to the curvature of the free surface.

The magnetic Reynolds number, which is defined as

$$Re_m = \mu_0 \sigma v L, \tag{2.30}$$

usually has a value of $Re_m < 1$ in typical metallurgical applications involving liquid metal flows. Therefore, the magnetic field distribution in the melt has mainly diffusive character and the magnetic field lines are not deformed by the motion of the conducting liquid. This allows us to neglect the fluid motion in electromagnetic calculations.

When the system is ***axisymmetric*** (what is really common for EM stirring and induction crucible furnaces), equation (2.14) can be solved with numerical methods in 2D cylindrical coordinates. Vector **A** has one component only - tangential - while $A_z = A_r = 0$ and $\nabla\varphi$ is zero:

$$\mu_0 \sigma \frac{\partial A_\theta}{\partial t} = \frac{1}{r}\frac{\partial}{\partial r}\left(r\frac{\partial A_\theta}{\partial r}\right) + \frac{\partial^2 A_\theta}{\partial z^2} - \frac{A_\theta}{r^2} \tag{2.31}$$

The field values, derived from (2.11):

$$B_z = \frac{1}{r}\left(r\frac{\partial A_\theta}{\partial r}\right) \qquad\qquad B_r = -\frac{\partial A_\theta}{\partial z} \tag{2.32}$$

Also, using (2.6) and (2.13):

$$J_\theta = -\sigma \frac{\partial A_\theta}{\partial t} \tag{2.33}$$

Finally, non-zero Lorentz force components:

$$F_r = J_\theta B_z \qquad\qquad F_z = -J_\theta B_r \tag{2.34}$$

where it is possible to observe that current density is made of one component only.

In the case of ***harmonic analysis***, the solution variable A_θ can be written as the summation of real and imaginary part $A_\theta = A_{re}\cos(\omega t) A_{im}\sin(\omega t)$. Therefore, current density will be:

$$J_{\theta,re} = \omega\sigma A_{im} \qquad J_{\theta,im} = \omega\sigma A_{re} \tag{2.35}$$

The time-average magnitude of the Lorentz force and Joule heat density can be obtained from the results of the numerical analysis as:

$$F_r = \frac{1}{2}\left(J_{\theta,re}B_{z,re} + J_{\theta,im}B_{z,im}\right) \quad F_z = -\frac{1}{2}\left(J_{\theta,re}B_{z,re} + J_{\theta,im}B_{z,im}\right) \tag{2.36}$$

$$Q = \frac{J_{re}^2 + J_{im}^2}{2\sigma} \tag{2.37}$$

These values appear then in the hydrodynamic and energy equations as source terms.

2.2 Fluid flow features and actual turbulence models

Incompressible fluid flow is defined by the laws of *conservation of mass* and *momentum*. These laws are expressed in terms of partial differential equations:

$$\nabla \cdot \mathbf{v} = 0 \tag{2.38}$$

$$\rho\frac{\partial \mathbf{v}}{\partial t} + \rho\left(\mathbf{v}\nabla\right)\mathbf{v} = -\nabla p + \mu\Delta\mathbf{v} + \rho\mathbf{g} + \mathbf{f} \tag{2.39}$$

where $\vec{\mathbf{g}}$ is gravity acceleration, ρ is the fluid density and μ is the dynamic viscosity; $\mathbf{v}$ is the velocity of the fluid. The last two terms on the right represent forces responsible for the movement of the fluid. Density in liquid metals usually depends on temperature as $\rho = \rho_0(1 - \beta(T - T_0))$, where β is the thermal expansion coefficient and T_0 some reference temperature. This is particularly true in the case of small temperature deviation. Furthermore, considering that $\rho_0\vec{\mathbf{g}}$ is constant in the whole domain (and it can also be considered as a part of the operating pressure p in form of $\rho_0 gz$), the corresponding term in (2.39) becomes $-\rho_0\vec{\mathbf{g}}\beta(T - T_0)$. This is called *buoyancy force*. More famous *Navier-Stokes* equation can be derived as a particular form of momentum equation (2.39) and, for

incompressible fluids, it can be written as:

$$\frac{\partial v_i}{\partial t} + v_j \frac{\partial x_i}{\partial x_j} = -\frac{1}{\rho_f}\frac{\partial p}{\partial x_i} + \nu \frac{\partial^2 v_i}{\partial x_j \partial x_j} + f_i, \quad i = 1, 2, 3 \tag{2.40}$$

where $\nu = \mu/\rho$ is the kinematic viscosity and indices take the values 1, 2 and 3, which correspond to x, y and z directions. Using the rate of strain $2S_{ij} = \partial v_i/\partial x_j + \partial v_j/\partial x_i$, Navier-Stokes equation becomes:

$$\frac{\partial v_i}{\partial t} + v_j \frac{\partial x_i}{\partial x_j} = -\frac{1}{\rho_f}\frac{\partial p}{\partial x_i} + \frac{\partial}{\partial x_j}\left[\nu\left(\frac{\partial v_i}{\partial x_j} + \frac{\partial v_j}{\partial x_i}\right)\right] + f_i \tag{2.41}$$

where gravitation and EM force are typical forces acting on the fluid during induction processes. Electromagnetic force can be expressed as $\mathbf{F}_{EM} = 0.5\Re e(\mathbf{J} \times \mathbf{B})$, where $\mathbf{J}$ is the induced current density and $\mathbf{B}$ is the intensity of external magnetic field. Using Ohm's law, electromagnetic force can be estimated as:

$$f_{em} \sim \sigma v B^2 \tag{2.42}$$

In the absence of the external forces, dimensionless Grashof number becomes an important parameter in order to put in evidence the ratio between buoyancy and viscous forces:

$$Gr = \frac{\rho_0 g \beta (T - T_0) L^3}{\mu} \tag{2.43}$$

in typical induction applications its order of magnitude is about 10^4, much lower than the critical value of 10^8, when natural convection becomes turbulent. Dimensionless Reynolds number is introduced to estimate the ratio between inertial and viscous forces:

$$Re = \frac{UL\rho}{\mu} = \frac{UL}{\nu} \tag{2.44}$$

In the case of inertial effects great enough than viscous effects, Reynolds number is above 2000-3000 and the flow is assumed to be turbulent; velocity fluctuates at every point of the flow field. In that case, instantaneous velocity can be expressed in terms of a mean value and a fluctuating component:

$$\mathbf{v} = \bar{\mathbf{v}} + \mathbf{v}' \tag{2.45}$$

where $\bar{\mathbf{v}}$ is the mean component of velocity in x-direction and $\mathbf{v}'$ is the fluctuating component along x again. The time-average of fluctuating component is zero:

$$\frac{1}{\delta_t}\int_0^{\delta_t} \mathbf{v}' dt = 0, \tag{2.46}$$

where δ_t is a proper interval of time, chosen for making the expression true and so that transient effect does not affect this integration. After the substitution of (2.45) in momentum equations (2.39), time averaging leads to additional terms like this:

$$\sigma_x^R = -\frac{\partial}{\partial x}\left(\overline{\rho v_x' v_x'}\right) - \frac{\partial}{\partial y}\left(\overline{\rho v_x' v_y'}\right) - \frac{\partial}{\partial z}\left(\overline{\rho v_x' v_z'}\right) \tag{2.47}$$

where σ^R is Reynolds stress term. These terms can not be calculated directly and, therefore, they introduce new unknowns into the momentum equation. They are assumed to be equivalent of a viscous stress term with an unknown coeffcient:

$$-\overline{\rho v_i' v_j'} = \mu_t \left(\frac{\partial v_i}{\partial x_j} + \frac{\partial v_j}{\partial x_i}\right) \tag{2.48}$$

This approach to turbulence modelling allows to combine diffusion terms in the original equation (2.39) if the effective viscosity is defined as the sum of laminar and turbulent viscosities:

$$\mu_{ef} = \mu + \mu_t \tag{2.49}$$

The solution of turbulence problem provides an estimation of the turbulent viscosity for Navier-Stokes equation. It is a partial differential equation, boundary and initial conditions should be included to the model. Two kinds of fluid boundaries will be described, the ones that will be taken into account during the following simulations: smooth solid wall and free surface of the fluid. *Wall* means that no fluid may pass through it and therefore normal velocity to the boundary must be equal to the velocity of the wall:

$$\mathbf{v} \cdot \mathbf{n} = \mathbf{V}_S \cdot \mathbf{n} \tag{2.50}$$

where $\mathbf{V}_S$ is the velocity of the wall and $\mathbf{n}$ is surface normal vector. Tangential velocity component on the wall must be zero because of viscosity of the fluid (no-slip boundary condition). On the other hand, *free surface* of the fluid allows existence of tangential velocity component and it can be expressed with the boundary condition:

$$\mathbf{v} \times \mathbf{n} = \mathbf{V}_S \times \mathbf{n} \tag{2.51}$$

Several ways has been developed for modelling the turbulent flow. The most simple case is to set constant turbulent viscosity, which is much larger than molecular viscosity.

$k - \varepsilon$ model is more advanced and thus it is the most spread in engineering applications; it has been then modified in many different ways to adapt it to various flow conditions. In standard $k - \varepsilon$ model, turbulent viscosity is calculated with the help of the

following expression:

$$\mu_t = C_\mu \rho \frac{k^2}{\varepsilon} \tag{2.52}$$

where k is the *turbulent kinetic energy*, ε is the *dissipation rate* of turbulent kinetic energy and $C_\mu = 0.09$ is a constant term. Two differential transport equations can be described for k and ε:

$$\rho \frac{\partial k}{\partial t} + div(\rho \mathbf{v} k) = \nabla \left(\frac{\mu_t}{\sigma_k} \nabla k \right) + G - \rho\varepsilon \tag{2.53}$$

$$\rho \frac{\partial \varepsilon}{\partial t} + div(\rho \mathbf{v} \varepsilon) = \nabla \left(\frac{\mu_t}{\sigma_\varepsilon} \nabla \varepsilon \right) + C_{1\varepsilon} \frac{\varepsilon}{k} G - C_{2\varepsilon} \rho \frac{\varepsilon^2}{k} \tag{2.54}$$

The three terms on the right side of the equations are, respectively, the diffusion, generation and dissipation terms, where G is responsible of the generation of kinetic energy of the turbulence:

$$G = \mu_t \left(\frac{\partial v_i}{\partial x_j} + \frac{\partial v_j}{\partial x_i} \right) \frac{\partial v_i}{\partial x_j} \tag{2.55}$$

where the semi-empirical coefficients:

$$C_{1\varepsilon} = 1.44, \quad C_{2\varepsilon} = 1.92, \quad \sigma_k = 1.0, \quad \sigma_\varepsilon = 1.3. \tag{2.56}$$

The solution of these turbulence equations allows to calculate effective viscosity and thermal conductivity:

$$\mu_{ef} = \mu + C_\mu \rho \frac{k^2}{\varepsilon} \tag{2.57}$$

$$\lambda_{ef} = \lambda + \frac{\mu_t c_p}{Pr_t} \tag{2.58}$$

where c_p is the specific heat and Pr_t is a turbulent Prandtl number. The dimensionless Prandtl number shows the ratio of impulse and heat diffusivity. In laminar flows its value is calculated with following expression:

$$Pr = \frac{\mu c_p}{\lambda} \tag{2.59}$$

Turbulent Prandtl number used in (2.58) has a constant value which varies in the standard model from 0.7 up to 1.0 depending on numerical realization. Several modifications of

this basic model have been developed; they usually differ in either the C_μ term or in the source term of the dissipation equation. One of them is the Renormalized-Group (RNG) model, where the expression for turbulent viscosity (2.52) is replaced with the following differential equation:

$$d\left(\frac{\rho^2 k}{\sqrt{\varepsilon\mu}}\right) = 1.72\frac{\hat{\nu}}{\sqrt{\hat{\nu}^3 - 1 + C_\nu}}d\hat{\nu} \tag{2.60}$$

where $\hat{\nu} = \mu_{ef}/\mu$ and $C_\nu \approx 100$. In the case of high Reynolds number this equation gives the same result as (2.52). An option to take into account the effect of rotation in the mean flow is also provided by the RNG model, so that, these and several other features the RNG more accurate than $k - \varepsilon$ model for some specific classes of flows.

The $k - \omega$ model is another widely spread turbulence model, which is based on transport equations for the turbulence kinetic energy k and the specific dissipation rate ω, which is defined as the ratio between ε and k. These equations are similar to those of the $k - \varepsilon$ model. Coefficient α^* is introduced, which damps the turbulent viscosity causing low-Reynolds-number correction:

$$\alpha^* = \alpha^*_\infty\left(\frac{\alpha^*_0 + Re_t/R_k}{1 + Re_t/R_k}\right) \tag{2.61}$$

where

$$Re_t = \frac{\rho k}{\mu\omega}, \quad R_k = 6, \quad \alpha^*_0 = \frac{\beta_i}{3}, \quad \beta_i = 0.072 \tag{2.62}$$

In the case of high-Reynolds-number flow α^* becomes 1.

The combination of $k - \omega$ model in the inner part boundary layer and $k - \varepsilon$ model in the outer part is called shear-stress transport (SST) $k - \omega$ model. This last one includes modified turbulent viscosity formulation to take into account transport effects of the principal turbulent shear stress. A cross-diffusion term in the ω equation has then been included, plus a blending function to ensure that model equations behave appropriately in both the near-wall and far-field zones.

All of these two-equations turbulence models belong to one class, which is based on the RANS approach and, therefore, have some common advantages and disadvantages when applied in the induction field. Their positive sides are the good prediction of flow pattern even on relatively coarse meshes and short time required for achieving steady-state solution. On the other hand, because of Reynolds time-averaged equations, they all include assumptions about isotropy of the turbulence and stability of the flow (at least when boundary conditions are time-constant). These two last conditions are not always applicable, especially in the case of rotating flows (*i.e.* EM stirring).

2.3 Energy balance in turbulent flows

Energy equation for the single-phase flow has the following form:

$$\frac{\partial}{\partial t}(\rho E) + \nabla \cdot (\mathbf{v}(\rho E + p)) = \nabla \cdot (\lambda_{ef} \nabla T + (\bar{\bar{\tau}}_{ef} \cdot \mathbf{v})) + Q \tag{2.63}$$

where the first two terms on the right side of the equation are responsible for conductive energy transfer and viscous dissipation. $\bar{\bar{\tau}}_{ef}$ is called deviatoric stress tensor:

$$\bar{\bar{\tau}}_{ef} = \mu_{ef} \left(\frac{\partial v_i}{\partial x_j} + \frac{\partial v_j}{\partial x_i} \right) - \frac{2}{3} \mu_{ef} \frac{\partial v_i}{\partial x_j} \delta_{ij} \tag{2.64}$$

Energy E is:

$$E = h - \frac{p}{\rho} + \frac{v^2}{2} \tag{2.65}$$

and λ_{ef} is the effective conductivity ($\lambda + \lambda_t$ are material and turbulent thermal conductivities). Enthalpy h in incompressible flow is:

$$h = \int_{T_{ref}}^{T} c_p dT + \frac{p}{\rho} \tag{2.66}$$

Last term Q in (2.63) is the density of heat sources, which is represented by Joule heat in the case of induction processes.

Turbulent motion of the fluid greatly increases energy transfer in the normal direction to the averaged flow streamlines. Correct estimation of its contribution is vital for final results of temperature distribution. The estimation of its quantitative value is closely correlated with the estimation of the turbulence intensity (which is the main task of any turbulence model). The effective thermal conductivity λ_{ef} directly depends on turbulent viscosity and turbulent Prandtl number Pr_t in the case of $k - \varepsilon$ turbulence model. While turbulent viscosity distribution is the product of turbulence modelling, Pr_t is a user-defined constant. Values between 0.7 and 1 are usually taken for it. An analytical expression for estimating turbulent Prandtl number is often adopted and it is given by the ratio of eddy diffusivity for momentum transfer ε_M and heat transfer ε_H:

$$Pr_t = \frac{\varepsilon_M}{\varepsilon_H} \tag{2.67}$$

Considering, that turbulent viscosity is usually several times higher than molecular one, the value of this dimensionless number has important influence on resulting effective thermal conductivity and, therefore, on heat transfer and temperature distribution predicted by $k - \varepsilon$ turbulence model. The concept of eddy diffusivity looses its meaning in the

case of three-dimensional or/and recirculating flows, thus restricting the application of Prandtl number to the two-dimensional boundary layers. But even there number's meaning is significantly reduced when liquid metals are the subject of modelling: relatively high molecular thermal conductivity of metals makes the influence of Pr_t negligible and it can be taken as unity.

LES method implements the same approach of effective thermal conductivity with the important difference that sub-grid viscosity, which replaces turbulent viscosity, is much smaller and, hence, the value of Pr_t has less influence on modelling results. Additionally, due to the transient modelling approach, main contribution to the heat exchange is resolved directly as convective energy transfer. The finer the mesh becomes, the lower gets the term representing heat conduction by molecular viscosity and sub-grid turbulence. The same rules are applied for transport of scalar quantities in the flow, like alloy additives, with the condition of them being fine enough and not influencing flow pattern.

2.4 Thermal fields

In electromagnetic systems, several sources of heat exist, like Joule heat and magnetic hysteresis. The three heat transfer principles are briefly explained as follows:

Conduction is a process where heat is transmitted between bodies having physical contact. *Fourier's equation* describes this phenomenon:

$$C\frac{\partial T}{\partial t} + \nabla\left(-\lambda \nabla T\right) = Q, \tag{2.68}$$

where T is the temperature, c thermal capability, λ the thermal conductivity and Q thermal source volumetric density. Since λ is assumed constant, (2.68) can be rewritten as:

$$\nabla^2 T - \frac{c}{\lambda}\frac{\partial T}{\partial t} = -\frac{Q}{\lambda}, \tag{2.69}$$

which is similar to (2.22) and can also be solved in the same way. For instance, Q can be written as Joule's effect source by $Q = J^2/\sigma$.

Convection occurs when a fluid has a contact with a heated solid body; hotter particles of the fluid rise up because of their lower density and they are replaced by cooler ones, with higher density, generating a constant motion of the fluid. *Forced convection* can also be produced; in this case the circulating process is not driven by density difference between particular sections of the fluid but convection is artificially driven by e.g. fun or

a pump. Heat is transmitted from the body to the fluid according to:

$$\lambda \frac{dT}{ds} = -h(T - T_a), \tag{2.70}$$

where h stands for the heat transfer coefficient by convection, T is the temperature of the heated element and T_a the temperature of the fluid far from the element.

Every element with temperature higher than zero [K] emits radiation through electromagnetic waves; this phenomenon is called ***radiation***. In this case heat transfer from a body at the temperature T to a second body at temperature T_a follows the equation:

$$\lambda \frac{dT}{ds} = -\varepsilon\gamma \left(T^4 - {T_a}^4\right), \tag{2.71}$$

where ε is the emissivity of the body and γ represents Stefan Boltzmann constant.
Generally talking, these three heat transfer phenomena act together and combined in a heating setup, excpet from vacuum spaces, where radiation only takes place.

2.5 GalInStan usage in research laboratory

GalInStan is an eutectic[1] metal alloy, which has been successfully used during experimental activities described in this thesis, for reproducing thus investigating liquid metal behaviour during continuous casting process. This metal alloy is really interesting for its benign properties (non-toxic metal) and for its low melting temperature, which allow experimental activities with its liquid at room temperature (see Table 2.1). In the frame of magneto and thermofluid research, many important Universities choose GalInStan for their experiments and cooling applications; from the experience gained in these institutions, instructions and observations about its usage have then been described.

GalInStan is a low-temperature, liquid metal alloy, made of 68% Gallium $[Ga]$, 20% Indium $[In]$ and 12% Tin $[Sn]$ by volume, though exact composition could vary because its patent belongs to the German company *Geratherm Medical AG*. Unlikely many metals, GalInStan is chemically compatible with a wide variety of metals, plastic, rubbers and glasses at low temperatures. It also has more attractive cooling and handling properties than those of Hg, Pb (lead) and Pb alloys. GalInStan and its variant alloys have potential uses in electrical engineering, energy research engineering, medicine and other applications. Universities of California and Princeton have been conducting various magnetohydrodynamic experiments [19] with relevance to basic physics and fusion reactor

[1] an *eutectic system* is a homogeneous solid mix made of two or more chemical species whose melting temperature is lower than the one of each substance making the system. The name comes from Greek and it means “easy to melt”.

GalInStan:	Gallium, 68%	Indium, 20%	Tin, 12%
Property	***Notation***	***Unit***	***Value***
colour			silver
odour			odourless
boiling temperature	ϑ	$°C$	> 1300
melting temperature	ϑ	$°C$	$+4$
density	ρ	kg/m^3	6440
dynamic viscosity	μ	$Pa \cdot s$	0.0024
surface tension	γ	N/m	0.718
electrical conductivity	σ_e	S/m	$3.46 \cdot 10^6$
speed of sound in the medium	V_c	m/s	2730
solubility			insoluble

Table 2.1: GalInStan general properties; $20°[C]$ temperature reference

cooling since 2002. One of the main drawbacks to Gallium and its alloys is price, which can vary widely with word market demand and it is a major constraint in the design of experiments. When GalInStan is exposed to air, it slowly oxidises to form Ga_2O_3 contamination. Furthermore, most liquid metal do not easily "wet" new surfaces; a primary reason is surface oxides on the metal. Ga and GalInStan easily wet glass surfaces at room temperature but in practice do not readily wet metal surfaces. GalIStan is not chemically reactive like liquid Ga and is compatible with most metals and plastics, which makes handing easier. Notable exceptions of incompatible metals include aluminium, which is readily attacked at room temperature, and copper, which is attacked over long times at elevated temperatures (> 100 [°C]). GalInStan is a chemically benign metal alloy and its components all have very low vapour pressures at elevated temperatures, on the order of 10-9 [atm] at 538 [°C] and virtually zero at room temperature. Therefore, this alloy spills do not evolve respirable metal vapours. In order to check what kind of reactions GalInStan alloy would form at room temperature with ambient air, computer simulations have been realized: they showed that significant quantities of Ga_2O_3 are not produced

while In_2O_3 and SnO_2 are very little. Only trace amounts of GaN would be produced. Thanks to its non-toxic properties, GalInStan is also strongly used to replace mercury in miniature devices.

Table (2.1) summarizes main properties of GalInStan metal. Exact value of its melting temperature is still unknown: some articles declare lower values, like -19 [°C], while few others confirm the one in table. Anyway GalInStan melting point is much lower than its components'; Gallium melts at 29.76 [°C] while Indium and Tin over 100 [°C]. Speed of sound is a fundamental parameter for proper setting of flow velocity measurement system (UDV); detailed description is present in the following section.

2.6 Velocity measurement of liquid metal flow

Ultrasonic Doppler Velocimeter (UDV) has been part of the setup of the experimental activities carried on for this thesis work; it was used for determining flow parameters of molten GalInStan. Doppler ultrasound technique, was originally applied in the medical field and dates back more then 30 years. As the name implies, its operating principles are based on the Doppler effect, $i.e.$ on changing the frequency of the ultrasonic wave emitted and received by the sensor by the wave is reflected by the microparticles distributed in the fluid. The particle drift velocity within the ultrasonic beam is determined by difference between the frequencies of the emitted and reflected waves, thus finding the Doppler frequency in the received signal. This method is widely used for finding the flow parameters in low-melting liquid metals and model fluids [23].

In the experiment described, a DOP3010 Ultrasonic Doppler velocimeter (Signal Processing SA, Switzerland) was adopted; in this device, traditional Doppler ultrasound technique has been extended with the use of pulsed emissions (Fig.2.2): instead of emitting continuous ultrasonic waves, an emitter periodically sends a short ultrasonic burst; when burst reaches the particle, an echo is generated (*scattering effect*[2]) when the particle is much smaller than wave length, and each echo is then continuously collected by the ultrasonic beam, while main energy continues it propagation. Travelling time of the echo

[2]Ultrasonic waves generated by the transducer are confined in a narrow cone. As they travel in this cone they may be reflected or *scattered* when they meet a particle having a different acoustic impedance. The acoustic impedance is defined by the product of the density of particle's material and its sound velocity $Z = \rho \cdot c$. If size of the particle is bigger than wave length, the ultrasonic waves are reflected and refracted by the particle. In such a case the direction of propagation and the intensity of the ultrasonic waves are affected. But if the size of the particle is much smaller than the wave length an other phenomena appears, which is named scattering. In such a case, a very small amount of the ultrasonic energy is reflected back to the transducer (backward scattering). The intensity and the direction of propagation of the incoming waves are practically not affected by the scattering phenomena. Ultrasonic Doppler velocimetry needs therefore particles smaller than the wave length.

form particle to the transducer is the key element for calculating depth of the particle in the fluid:

$$depth = \frac{c}{2 \cdot \Delta t}, \qquad \Delta t = t_t - t_e \tag{2.72}$$

where c is sound velocity of the acoustic wave in the liquid, t_t the moment when the echo reaches the transducer while t_e the time when burst is emitted. Δt is the travelling time. As already stated, ultrasonic bursts are emitted periodically and, following each emission, echo signal is sampled at a fixed delay after the emission. From equation (2.72) above, this delay defines the depth. If the particle moves between successive emissions, sampled values taken at a certain time T_s will change over the time. Depending of the shape of the emitted signal, these values may form a sinusoidal wave. Its frequency is named *Doppler frequency* (f_d) and is directly linked to particle's velocity, given by Doppler equation:

$$\upsilon = \frac{f_d \cdot c}{2 \cdot f_e \cdot \cos \delta} \tag{2.73}$$

where f_e is the emitted frequency of the emitted burst and δ is the angle between transducer's direction and particle's velocity direction (Doppler angle). In a real fluid system,

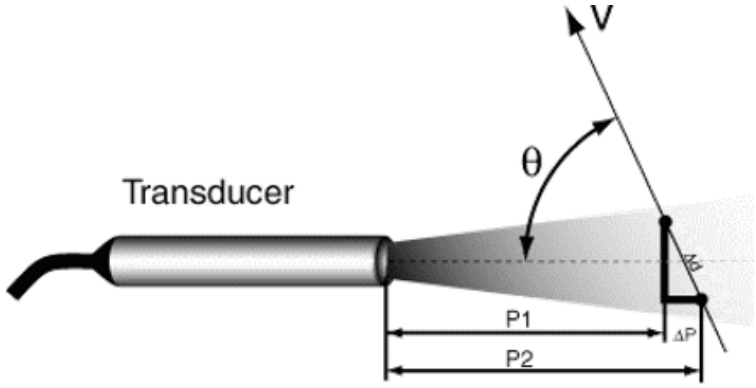

Fig. 2.2: General scheme of the Ultrasound Doppler Velocimeter (UDV) system.

particles are randomly distributed inside the liquid, thus giving a random echo signal; specific algorithms have been developed to extract global velocity information and they are based on the high degree correlation existing between different emissions. Pulsed Doppler ultrasound produces and instantaneous and complete velocity profile but, as the information is available periodically only, this technique suffers from the Nyquist condition. Maximum velocity from each pulse repetition frequency (f_{prf}) is:

$$\upsilon_{max} = \frac{f_{prf} \cdot c}{4 \cdot f_e \cdot \cos \delta} \tag{2.74}$$

which determines

$$depth_{max} = \frac{c}{2 \cdot f_{prf}} \tag{2.75}$$

as maximum measurable depth. During the experimental activities carried out for thesis, the sensor (8 [mm] in diameter) was placed directly into the fluid through the free surface to a depth of 1 - 2 [mm] and fixed in that position throughout the entire activity. Frequency of the signal transmitted by the sensor was 1428 [Hz] at the speed of sound in the melt equal to 2730 [m/s]. Measured velocity components had a negative value if the flow parallel to the signal beam was directed toward the sensor and a positive one if particles in the fluid were moving away from the sensor.

Chapter 3

Numerical model

3.1 Finite Element Analysis

In the solution of complex engineering problems, application of conventional analytical methods may be impossible or impractical. Analysis and design of electrical equipment is a difficult task due to several aspects, like complex geometry, non-linear characteristics of materials, interaction with thermal and mechanical phenomena, dynamic phenomena. Therefore, the first step of each analysis must be an accurate selection of which aspects are taken into account and which not: this initial step takes the name of *modelling*. A clear example is the choice between static and dynamic analysis. Choosing a proper numerical method for solving the problem represents the second step and it is called *discretisation*; in this case, an example is the choice between a system of ordinary or partial differential equations (PDE). In the following description of this dissertation, we will refer to FEMethod only, which is one of the most common. The third and final step is the computation of additional results and the analysis of the *solution*; in the case of clearly wrong or not satisfying results, the analysis must be repeated with different parameters.

3.1.1 PDE solution

Usually, direct solution of PDE is possible for simple cases only or under restrictive assumptions. Therefore, numerical methods are often the only practicable alternative for solving detailed and realistic models. The main objective of a numerical model is to solve PDEs on a discrete set of points of the solution domain; in order to do so, the domain in which the solution wants to be solved is divided into subdomains, having the discretization points as vertices. Distance between two adjacent vertices is the *mesh size*. Time is

also subdivided into discrete intervals and the interval between two consecutive instants at which the solution is calculated is called *time step*. PDE is approximated, or discretized, in order to achieve a system of algebraic equations where unknowns are the solution values at the discretization points; the set of algebraic equations can be solved with iterative techniques. After the discretization, it is necessary to check if the approximation gave an appropriate result. For a successful solution, numerical scheme must be stable, convergent and consistent. The scheme is stable if the solution stays bounded during solution procedure. It is convergent if numerical solution gets closer and closer to the real solution as mesh size and time-step tends to zero. The scheme is consistent if truncation error (error introduced by finite approximation of derivatives) tends to zero as well.

Let us call Φ the unknown PDE function: it must not only fulfil the solution inside region R - the calculation domain - but it also must satisfy certain conditions on S, R's boundary. Therefore, the choice of boundary conditions has an important influence in the final solution.

Three different kinds of boundary conditions can be imposed:

- *Dirichlet* condition is assigned by fixing a determined value of the potential on a given boundary curve. In this way, the curve is characterized by a constant value of potential; thus, equipotential lines result tangential to such a boundary

$$\Phi(r) = f(r) \qquad r \quad on \quad S \tag{3.1}$$

- *Neumann* condition is assigned by fixing the normal derivative of the potential on a given boundary curve. In other words, the line crosses the boundary in a known way and the following condition is satisfied:

$$\frac{\partial \Phi(r)}{\partial n} = g(r) \qquad r \quad on \quad S \tag{3.2}$$

- *Mixed* boundary condition represents a combination of the two previous cases.

PDE can be solved, thanks to the finite element method, by following two different approaches: the *Variational approach* and the *Weighted residual approach*. Their application to a PDE system produces the same set of equations to solve, but in the Variational approach, a function to be minimized (typically the energy of the system) is required, while the Weighted residual approach starts instead from the differential equations of the system. In the most general case they can be written as:

$$L(\Phi) - f = 0, \tag{3.3}$$

where L is a linear operator (∇^2 for example), f is a known function (typically the source, referring to (2.22) and (2.23), and Φ the unknown function. The exact solution of the problem can be approximated by assuming that it varies according to a set of known functions, each one of them multiplied by an unknown coefficient:

$$\Phi_n = \varphi_0 + \sum_{j=1}^{n} a_j \varphi_j. \tag{3.4}$$

These approximate function coefficients can be determined by solving a set of equations, in the way it will be explained later. Function φ_0 is usually specified in order to satisfy Dirichlet boundary condition.

Introducing the so called *residual* R_n

$$L(\Phi_n) - f = R_n, \tag{3.5}$$

the residual function R varies in the domain Ω. Coefficients a_j are calculated by orthogonalization of residual R_n to a certain set of n weighting functions w_i, i.e. by zeroing the inner product:

$$\langle R_n, w_i \rangle = \int_\Omega R_n w_i d\Omega = 0 \qquad\qquad i = 1, 2, ..., n \tag{3.6}$$

where a possible choice is $w_i = \varphi_i$, i.e. weighting function equal to approximation function. This procedure takes the name of *Galerkin method*. Substitution of (3.4) and (3.5) in (3.6) produces a set of n simultaneous linear algebraic equations that can be solved taking into account boundary conditions.

3.1.2 ANSYS Mechanical APDL

The software used to carry out part of the analysis is ANSYS© Mechanical APDL. It does not permit to perform structural analysis only or solve mechanical issues in general, but it also allows thermo-structural and electro-thermal tasks.

The model in analysis is considered to be axisymmetric, i.e. every phenomenon is supposed to be identical on each semi-plane; the 3D view of the whole body is obtained by rotation of one semi-plane around **z** symmetry axis. With reference to a magnetostatic problem, for every 2D axisymmetric model the following conditions can be achieved by adopting a cylindrical coordinate system (r, φ, z):

- current density is made of the φ component only: $\mathbf{J} = (0, J_\varphi, 0)$; let us observe that J_φ component is function of r and z coordinates;

- magnetic vector potential **A** has one component only and it is parallel to vector **J** again: $\mathbf{A} = (0, A_\varphi, 0)$. As **J**, A_φ varies with **r** and **z**;
- thanks to the definition of magnetic vector potential (2.14), flux density vector **B** is made of two components along (r, z) plane:

$$\mathbf{B} = \left(\frac{\partial A_\varphi}{\partial z}, 0, \frac{1}{r} \frac{\partial}{\partial r}(r A_\varphi) \right). \tag{3.7}$$

2D *harmonic analysis* has been adopted, it calculates the effect of alternating current (AC) or voltage excitation on electromagnetic devices and moving conductors. Between these effects, the following are included:

- eddy currents,
- skin effect (eddy currents in current conductors carrying an impressed current),
- power loss due to eddy currents,
- forces and torque,
- two contacting bodies with dissimilar mesh.

Permanent magnets are not allowed in harmonic analysis because material hysteresis effects are neglected.

Anyway, for low-saturation cases a linear time harmonic analysis can be run in the condition of assumed constant permeability properties. In moderate to hight saturation cases, an analyst is most interested in obtaining global electromagnetic force, torque and power losses in a magnetic device under sinusoidal steady state excitation, but less concerned with the actual flux density wave form. Under such circumstances, an approximate nonlinear time harmonic procedure may be pursued: it can predict time averaged torque and power losses with good accuracy and yet at much reduced computational cost to the transient time-stepping procedure.

The basic principle of this analysis is to replace the DC $B-H$ curve with a fictitious or effective $B-H$ curve based on the *energy equivalence method*. With the effective $B-H$ curve, a nonlinear transient problem can be reduced to a nonlinear time-harmonic one; in this nonlinear analysis, quantities of the field are all sinusoidal at a given frequency, in a way that is close to the linear harmonic analysis, except that a nonlinear solution is computed. Let us observe that, given a sinusoidal power source, for a nonlinear transient analysis the magnetic flux density B has a non-sinusoidal waveform, while it is assumed sinusoidal in a nonlinear harmonic analysis; even if it is not a true waveform, it rather

represents an approximation to the fundamental time-harmonic of the real flux density B waveform. The time averaged global force, torque and losses, which are determined by the approximated fundamental harmonic of fields, are the subsequent approximations of the real values.

The kinds of elements were used in the simulation:

- PLANE 13: 2D element. Quadrilateral four-nodes or triangular three-nodes. It is defined up to four degrees of freedom per node: magnetic vector potential, displacements, temperature or time-integrated electric potential;

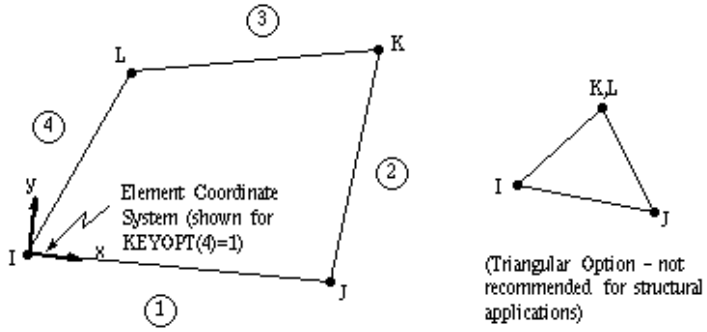

Fig. 3.1: ANSYS plane element number 13

- PLANE 53: 2D element. Quadrilateral eight-nodes or triangular six-nodes. Up to four DOF for each node: magnetic vector potential, time-integrated electric potential, current or electromotive force drop.

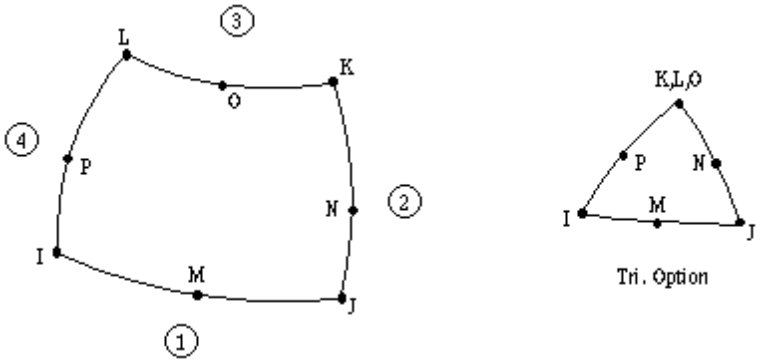

Fig. 3.2: ANSYS plane element number 53

3.1.3 FLUENT

Hydrodynamic calculations were performed with the commercial FLUENT© software, which uses control volume method for solving two- and three-dimensional problems on structured and unstructured meshes. The main idea under this numerical method is that equations to be solved describe the numerical fluxes between mesh cells by integrating the governing equations in numerical cells:

$$\oint \rho\phi\mathbf{v} \cdot d\vec{A} = \oint D_\phi \nabla_\phi \cdot d\vec{A} + \int_V S_\phi dV \tag{3.8}$$

where D_ϕ is the diffusion coefficient of the scalar term ϕ, $\vec{A}$ is the surface area vector and S_ϕ is the source term of ϕ scalar quantity per unit volume. Therefore, conservation laws are fulfilled in each local volume when solution is converged. Discretization of (2.68) in each computational cell gives:

$$\sum_f^N \rho_f \phi_f \mathbf{v}_f \cdot \vec{A}_f = \sum_f^N D_\phi (\nabla_\phi)_n \cdot \vec{A}_f + S_\phi V \tag{3.9}$$

where f is cell's face, N is the number of cell faces and subscript n refers to the magnitude of the $\nabla\phi$ normal to face f. Values of solution variables are stored in element centres, and it is necessary to obtain face values for convection terms in the discrete equations. This interpolation can be performed in several ways, which differ in speed of calculations and accuracy. The simplest first-order upwind scheme, for example, assumes that face value ϕ_f is equal to that in the centre of the cell (ϕ_c), which is located upstream relative to normal velocity $\mathbf{v}$. Second-order upwind scheme is more accurate; face values are computed using the equation:

$$\phi_f = \phi_c + \nabla\phi \cdot \vec{r} \tag{3.10}$$

where ϕ_c and $\nabla\phi$ are respectively the value in the upstream cell centre and its gradient, but $\vec{r}$ is the displacement vector pointed from the cell centre to the face centre. Central-differencing discretization scheme provides improved accuracy for the LES turbulence model. It calculates the face values as follows:

$$\phi_f = \frac{1}{2}(\phi_{c0} + \phi_{c1}) + \frac{1}{2}(\nabla\phi_0 \cdot \vec{r}_0 + \nabla_1\phi \cdot \vec{r}_1) \tag{3.11}$$

where indices 1 and 2 refer to cells adjacent to face f.

Pressure values are also stored in cell centres but the face values are required for momentum equation. The linear interpolation does not work properly when large pressure

gradient is present due to body forces acting on the fluid.

Pressure-velocity coupling scheme defines how pressure correction is performed in order to satisfy the continuity equation.

3.2 AMF application

3.2.1 Investigation setup and electromagnetic model

This thesis work has been carried out focusing on a limited section of the continuous casting line: the region immediately below the mould, where an initial stirring effect is applied and first water-cooling process starts the solidification of molten metal. Mould-electromagnetic stirrer has been taken into account and the first part of the investigation adopted an alternated-magnetic field (AMF) solution, so that two toroidal eddies were achieved with almost the same amplitude, energy and velocity inside the liquid. Both electromagnetic and hydrodynamic analysis have been carried out almost in parallel for this application and the main goal in this first setup was to investigate:

1. *if* the variation in the relative position between inductor coil and cast material, thus the movement of its solidification front, generated the transition from two-to-one toroidal vortices; the transition was supposed to happen when one of them is much bigger and energetic than the other.

2. *when* the transition happened; therefore, relative position between the inductor and melt could be determined when the transition occurred and consequent observations related to PMF application could have been stated.

As already asserted, GalInStan melt was chosen for the entire investigation thanks to its non-toxic properties and low melting temperature (see Table 2.1); any other kind of metal could be chosen, but GalInStan is liquid at room temperature and it allowed the experimental activities to be carried on with no additional heating systems for the metal, simulating properly stirrer interaction with melt during the real casting process. Furthermore, low melting temperature strongly advantaged measurement of the flow parameters.

Investigation setup included a cylindrical container made of Plexiglass in which the melt was placed; thickness of the vessel had no influence on the investigation, apart from the dissipation of heating produced by induced currents inside GalInStan melt. Height of the cylinder is almost the double of cylinder's radius (Table 3.1). For the experimental activities, a cover has been specifically designed for fixing UDV probe inside the metal during velocity measurements in transient conditions; the cover has not been taken into

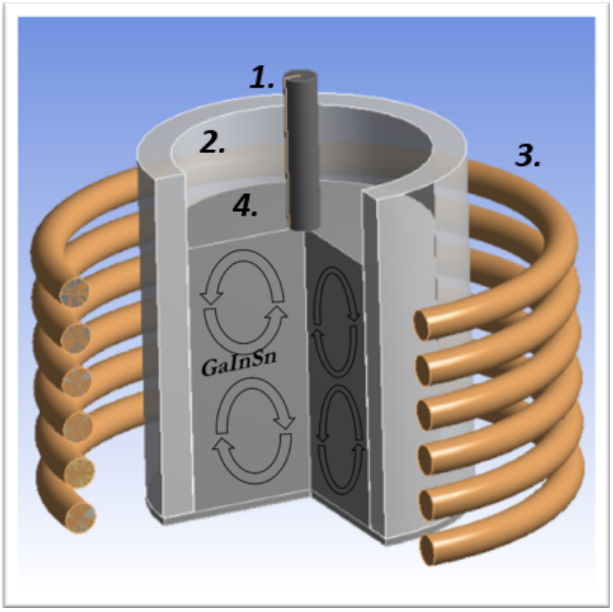

Fig. 3.3: Scheme of the investigation setup: 1- UDV transducer on the top of melt; 2- melt's vessel; 3- copper, 6-windings inductor; 4- GaInStan melt. Inside molten metal the two toroidal vortices can be noticed, generated from the interaction with the AMF.

account during numerical simulations. Initial configuration of the setup included a copper, 6-turns inductor surrounding the container and uniformly distributed over the height of the melt; horizontal axis of melt corresponded to the one of the coil. Such a symmetrical geometry has then been named *Inductor Position Zero* or *Symmetry Position*. Geometry of the inductor has been optimized for maximizing power transferred to the melt; its water-cooling system was not taken into account during the simulation and constant electrical and thermal parameters have been fixed for the inductor, supposing that its working temperature corresponded to 40 [°C]. It is common for numerical simulations to avoid modelling water-cooling system, with the advantage of achieving a more simple model, but the electrical resistivity of the coil is then evaluated in a range of temperature of $40 \div 60$ [°C]. The entire set of geometrical properties of the model has been reported in Table (3.1).

All of these data were then adopted to reproduce the electromagnetic numerical model in ANSYS© Mechanical APDL: thanks to the characteristics of the investigated system, 2-D axisymmetric model was developed; windings of the coil were represented with their transversal section only, as a circle, with no taking into account the natural slope that each turn had. Inductor's design was made so that the first and the last turn of the coil corresponded respectively to melt' surface and its bottom. Rectangular section was defined for the domain, its dimensions were sufficient for a proper evaluation of the magnetic field all around the inductor. Air properties have been associated for both this region and the

Inductor	*unit*	
number of windings		6
material		copper
further characteristics		water-cooled
radius	$[mm]$	61
winding radius	$[mm]$	4
distance between windings	$[mm]$	12.4
Melt's vessel		
shape		cylindrical
material		plexiglass
further characteristics		plexiglass cover for fixing UDV probe
external radius	$[mm]$	38.5
thickness of the wall	$[mm]$	7.5
thickness of the bottom	$[mm]$	1.5
total height	$[mm]$	98
GalInStan melt		
shape		cylindrical
material		GalInStan
internal radius	$[mm]$	23
external radius	$[mm]$	31
total height	$[mm]$	70

Table 3.1: Geometrical dimensions and main characteristics of the numerical model.

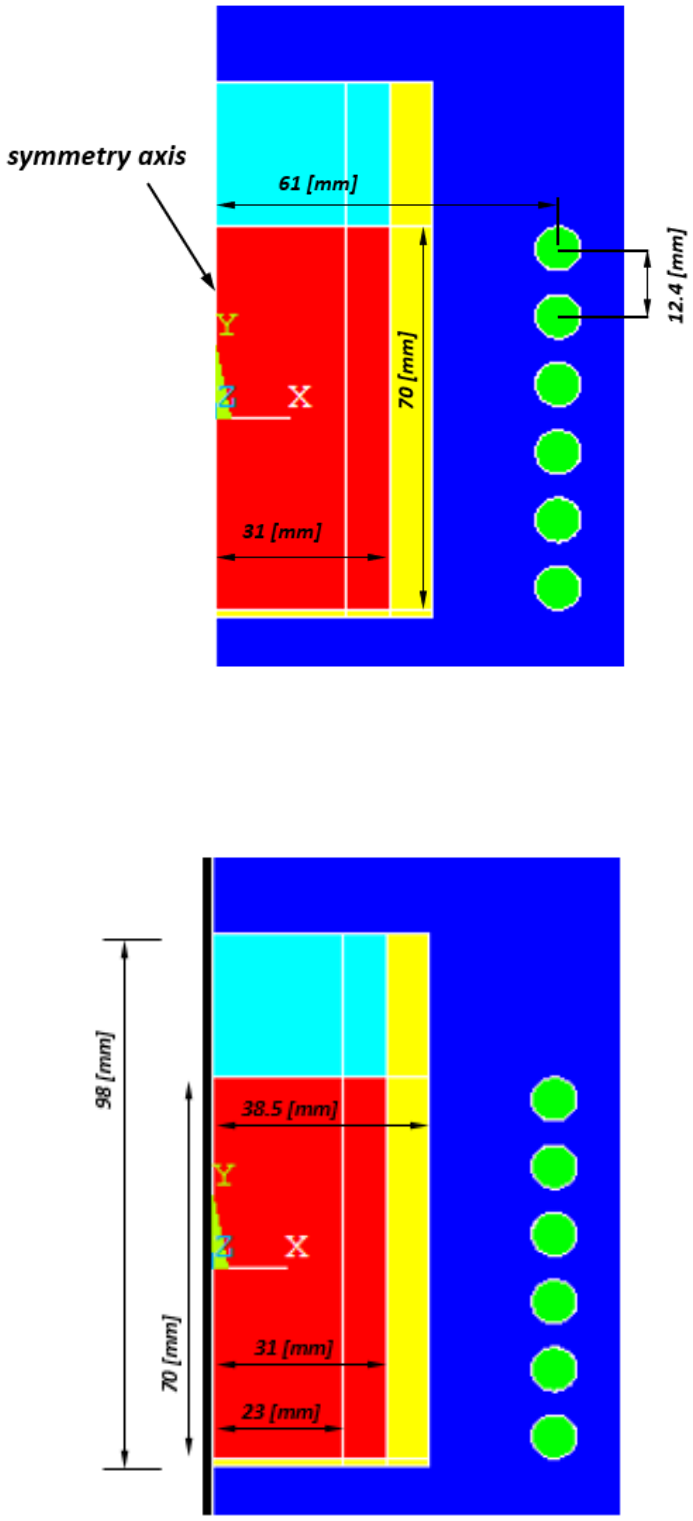

Fig. 3.4: Representation of numerical model main dimensions. Centre point of the turns was taken into account for each measure related to the inductor. Air box had a rectangular shape and no water-cooling system was modelled for the coil.

one between GalInStan melt and the superior border of the container.

Melt's movement downward along the real casting line was simulated with changing the relative position between melt and inductor: during the experimental activities in the laboratory, a platform allowed the vessel to be moved downward, while the inductor was kept on a fixed position. In numerical simulations, the relative movement was achieved with the definition of a new vertical

shifting variable = ***+12.4 [mm]***

which moved the inductor upward while fixing melt's position. Not a transient, continuous movement was produced but 7 fixed positions of the inductor have been investigated in the numerical model. It moved from a bottom position, *Symmetry*, to the top position, in which the last turn of the inductor was on the same level of melt' surface (Fig.3.5); this last configuration was named *Inductor Position 6* (the coil shifted upward of *shift* $\times$ 6 = +74.4 [mm]) and it is the last one investigated in the frame of this thesis. Geometry of air domain was naturally extended during inductor's shifting. For each position, electromagnetic and hydrodynamic solution was calculated in steady state regime. Materials associated to each region have been represented in Fig.(3.6) and electrical and magnetic properties were defined only; no dependence form temperature was taken into account, thus constant values for them were fixed. This made the model more simple reducing computational time for calculating the solution. Approximation with constant values did not produce any important computational error, especially because melt's temperature did not vary that much during laboratory experiments. The same properties were fixed for the air box above GalInStan melt and for air defining the domain, even if they have been coloured in slightly different ways to practically simplify the treatment of the model. Table (3.2) shows the set of electrical parameters applied to each region; no magnetic materials are present in the model, thus relative magnetic permeability $\mu_r = 1$ for everything. Copper's electrical resistivity is commonly approximated to $2 \cdot 10^{-8}[\Omega \cdot m]$ to consider overtemperature working condition of the inductor; $1.68 \cdot 10^{-8}[\Omega \cdot m]$ is its electrical resistivity at 20 [°C]. Great care was taken in GalInStan melt parameters choice, small variations of its electromagnetic resistivity σ_e produce strong variations of final simulation results. One white line can be noticed inside melt's region, next to its right border, and inside the air box: it was necessary to generate finer mesh for a more detailed analysis of electromagnetic quantities. Finer mesh is fundamental where quantities and fields rapidly change or where more accurate results want to be achieved. In this model, smaller mesh elements were chosen:

- inside coil's turns and in the surrounding region, for a more accurate investigation of the behaviour of the magnetic field and of its isolines;

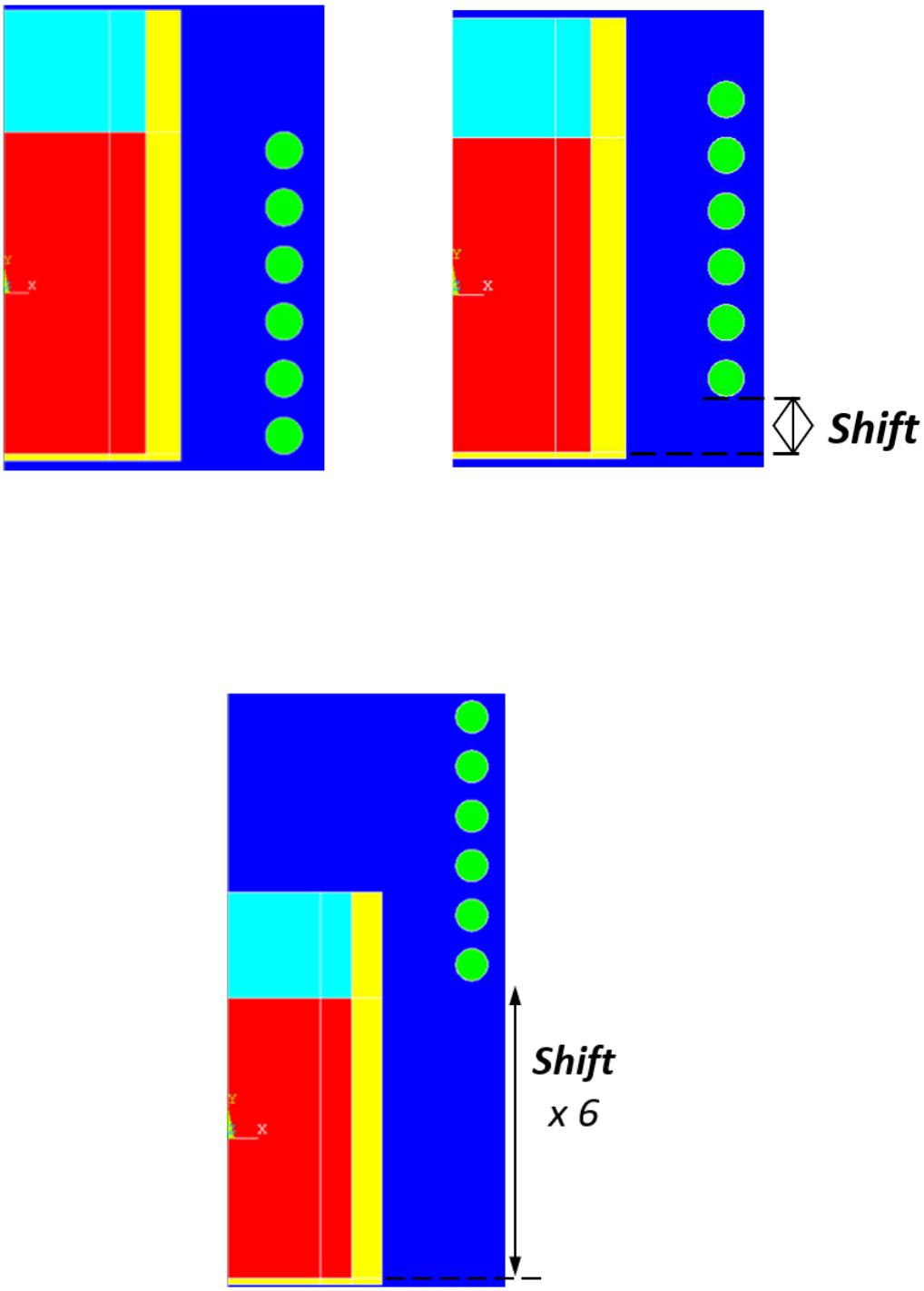

Fig. 3.5: Different configurations of the numerical model with the inductor shifting vertically; each position of the coil has been achieved with the definition of a *shifting variable* = ***+12.4*** *[mm]*. The first picture (top-left) shows the *symmetrical geometry*, while in the second one the inductor moved to *Position number 6*. The last picture represents the inductor on its maximum top position.

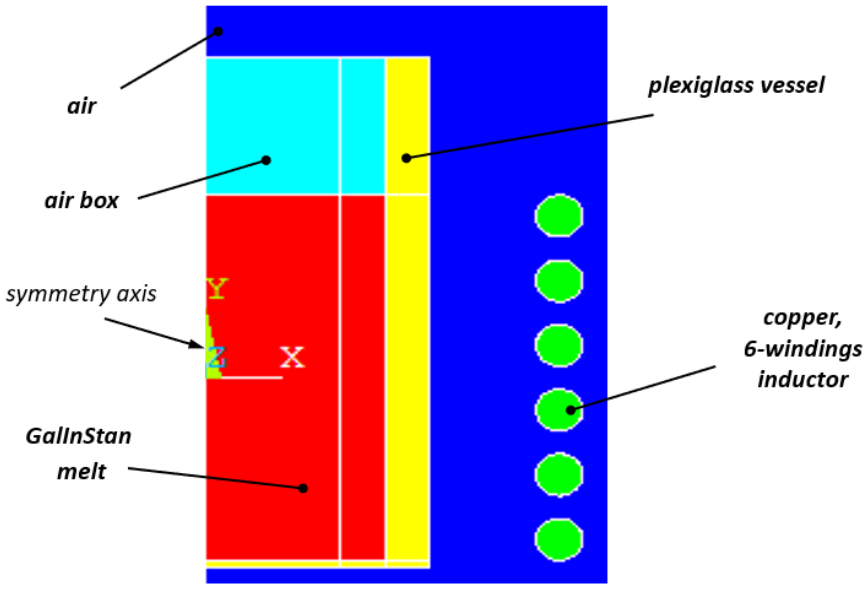

Fig. 3.6: Representation of different regions in the numerical model

Region	*Colour*	*Material*	*electrical resistivity* $[\Omega \cdot m]$
inductor	green	copper	const., $\sigma_e = 2 \cdot 10^{-8}$
melt	red	GalInStan	const., $\sigma_e = 0.435 \cdot 10^{-8}$
vessel	yellow	plexiglass	-
air (domain)	blue	air or vacuum	-
air box	light-blue	air or vacuum	-

Table 3.2: Physical properties of materials in numerical model.

- in a 8 [mm] - thick layer inside melt's region and the air box, in order to take into account skin effect inside GalInStan melt. Alternating current feeding the inductor produced a distribution of induced current inside the melt which is more concentrated on the external region of it, next to its border; this consequence must always be taken into account in numerical models, with finer mesh where concentration of current is higher, after the calculation of *skin depth*.

Sinusoidal current was supplied to the coil during the first step of this investigation, thus AMF was produced; its amplitude was $I_{RMS} = 200[A]$, with the frequency of $f_{AC} =$

$150[Hz]$. Resulting skin depth was:

$$\delta_{ac} = \sqrt{\frac{1}{\pi f_{ac} \mu_r \mu_0 \sigma}} \approx 27[mm]$$

It is possible to notice that relatively low frequency determined a skid depth which cov-

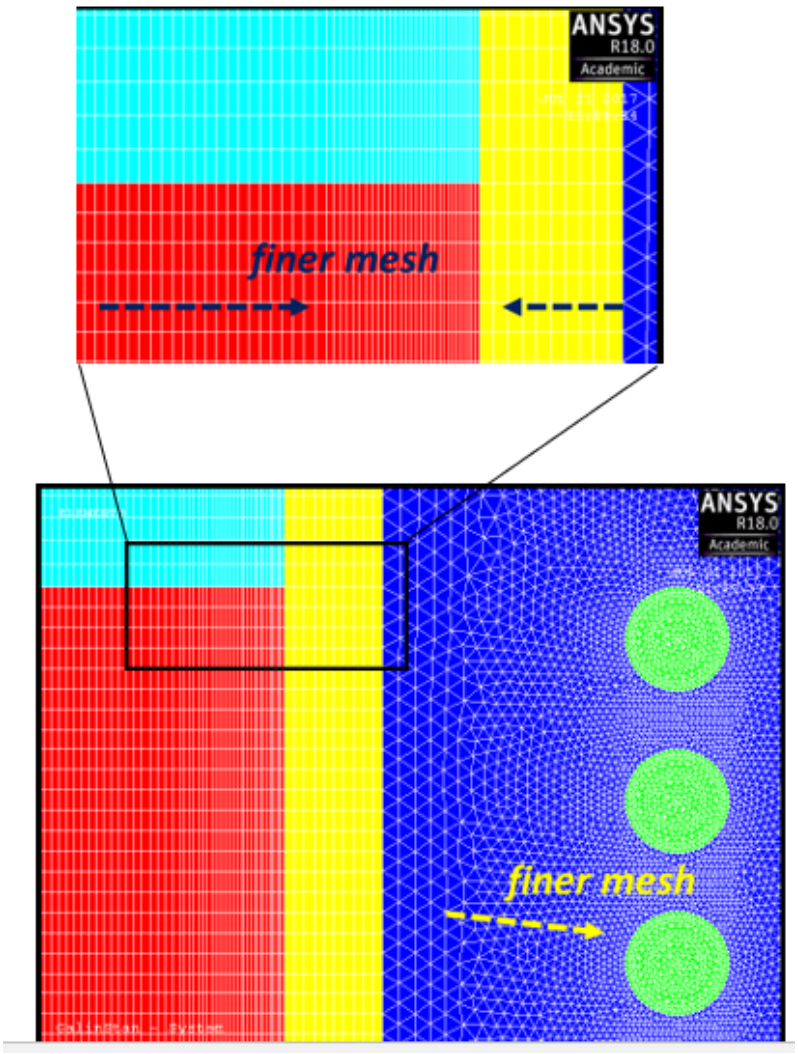

Fig. 3.7: Mesh chosen for electromagnetic numerical simulation. Finer mesh can be noticed.

ered most of GalInStan melt volume (27 [mm] over 31 [mm] of melt's radius); anyway, finer mesh (Fig.3.7) was chosen on a smaller section of the melt to reduce computational time, with a general decrease of the number of elements, and because global number of elements allowed to produce precise computational results for both the electromagnetic and hydrodynamic investigation.

Thanks to geometrical characteristics of the model, *mapped* mesh was adopted inside GalInStan melt region, air box and plexiglass vessel containing molten metal; rectangular elements have been defined with lower number of elements inside the container, because

no electromagnetic investigation was carried out inside of it. On the other hand, *automatic* mesh, thus triangular elements, has been adopted for the domain and inside regions defining turns of the inductor. Most uniform mesh possible was defined.

3.2.2 From electromagnetic to hydrodynamic solution

From a general point of view, electromagnetic simulation on ANSYS© Mechanical APDL was carried on with the aim of analysing induction effects inside GalInStan melt: while the inductor vertically moved upward for simulating casting effect, 7 fixed position of it have been investigated, each one of them in the ***harmonic regime***. As already stated, sinusoidal current was applied. For each position, *Lorentz Force* (2.7) and magnetic field distribution were calculated and their

- time average value and
- volume density distribution

have been evidenced; therefore, no global distribution was evaluated inside melt but electromagnetic results have been divided for each element's volume. Time average distribution came directly from the harmonic solution. No transient solution was necessary because electromagnetic time constant was much smaller than the hydrodynamic one.

An initial verification of electromagnetic results over *Inductor Position Zero* was based on previous studies [7, 22, 23] on the same experimental setup, to confirm that Lorentz force distribution and amplitude inside GalInStan melt were correct: when the coil was symmetrical to the molten material, symmetrical distribution of forces over x-horizontal axis was achieved and their maximum value was noticed in the middle of melt's volume. Radial component of Lorentz forces was produced but a vertical component was also present in very small regions inside the melt, corresponding to its top and bottom corners; such a behaviour was determined by the shape of magnetic field lines, which are almost vertical everywhere inside the melt, while they bend in correspondence to the previously stated zones (Fig.3.8). Flow pattern of the two toroidal vortices generated by the stirring effect was mainly influenced by Lorentz force vertical component. Magnetic field lines are perfectly vertical when inductor's length is much higher than melt's height (*e.g.* infinite-length inductors).

Electromagnetic solution was then manually exported to ANSYS FLUENT© and hydrodynamic behaviour of the flow was investigated for each position of the inductor in ***steady state*** condition: calculated Lorentz force distribution in the harmonic electrical regime became the starting point for calculating the flow pattern inside the melt. In the

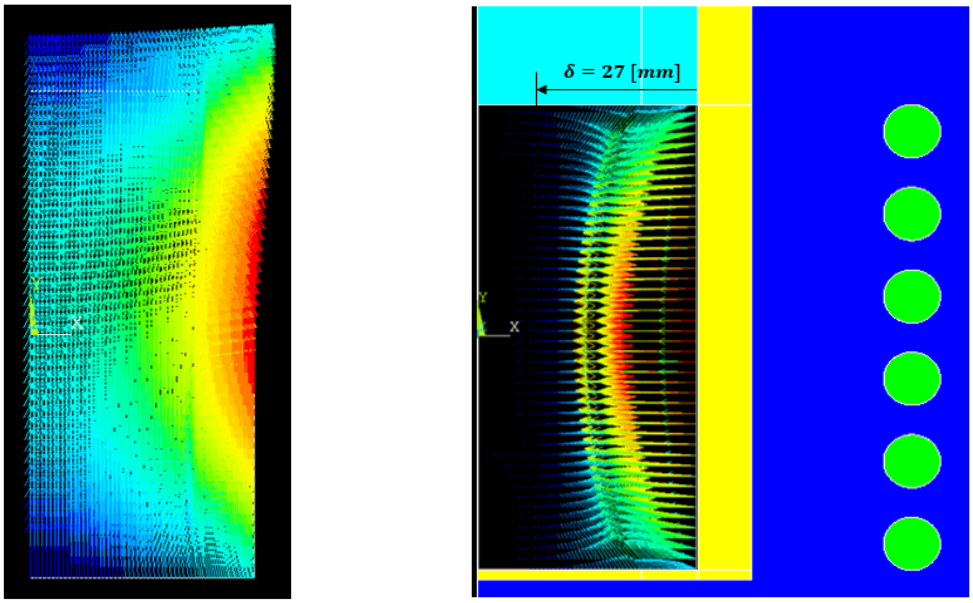

Fig. 3.8: Lorentz force volume density distribution $[N/m^3]$ on the left and magnetic field distribution $[A/m]$ on the right, inside GalInstan melt. Lorentz force amplitude range is between 10^{-8} (blue darts) and $0.5 \cdot 10^{-4}$ (red darts); magnetic field amplitude range is between $7 \cdot 10^3$ (blue darts) and $1.2 \cdot 10^4$ (red darts)

construction of FLUENT© numerical model, stirring effects inside melt's volume only were investigated; the cylinder of molten material was again modelled with a 2-D axisymmetric geometry but no other elements were useful for the simulation, so neither air nor the inductor have been taken into account. Refined mesh for hydrodynamic calculation was necessary and resulting number of mesh elements inside EM and fluid models was different: *user define function* (udf) was written to transport Lorentz forces in FLUENT© numerical model and guarantee the same distribution they had inside melt region of the Mechanical APDL model.

The main objective of hydrodynamic simulation consisted in the investigation of shape and velocity distribution of the two toroidal eddies during the movement of the inductor. In order to do that, steady state solution was calculated again, avoiding initial transient effects; standard $k - \varepsilon$ model was chosen instead of $k - \omega$. The former is valid for fully turbulent flows only and eddy viscosity is determined from a single turbulence length scale, so the calculated turbulent diffusion is that which occurs only at the specified scale, whereas in reality all scales of motion will contribute to the turbulent diffusion. Complex flows involving severe pressure gradient and separation are weakly performed; it adopts gradient diffusion hypothesis to relate Reynolds stresses to the mean velocity gradients and the turbulent viscosity. The latter allows for a more accurate near wall treatment with an automatic switch from a wall function to a low-Reynolds number formulation

based on grid spacing. It demonstrates superior performance for wall-bounded and low Reynolds number flows and it shows potential for predicting transition. $k-\omega$ performs significantly better under adverse pressure gradient conditions, thus it is appropriate for complex boundary layer flows. It can be noticed that $k-\varepsilon$ formulation perfectly suited the model under investigation, thanks to an homogeneous pressure distribution inside the melt and absence of significant velocity gradients. Furthermore, neither LES was adopted nor Volume of Fluid (VOF): while the former can be applied to 3-D models only, the latter is suitable for $k-\omega$ algorithm and in the analysis of the behaviour of two or more immiscible fluids. VOF solves a single set of momentum equations and tracks the volume fraction of each of the fluids throughout the domain. It has been widely applied in steady and transient tracking of liquid-gas interface when strong variations of it occurred; the most clear example can be found in the investigation of the meniscus for Induction Crucible Furnaces [39]. In the analysed system for this thesis, internal pressure inside the melt was so low that no significant meniscus was evidenced; the main reason for that can be found in small amplitude of the current supplied to the coil. Mathematical calculations were then verified with the experimental activities and no superficial variations of melt were noticed, apart from its oscillations.

Boundary conditions were fixed along all of the edges of melt region and they have been summarized in Table 3.3. It is well known that viscous flows locally keep the same velocity of the surface in contact with them; stationary *wall*, no slip, condition was chosen for bottom and side borders of melt, to factor the effect that a solid wall had on the flow into the calculations. No tangential component of velocity was defined for the fluid along these edges. On the other hand, stationary *wall*, but specified shear boundary condition, was applied to the free surface of the melt together with impermeability conditions; air pressure was the only constraint to verify whether Lorentz force significantly modified this surface and the two internal vortices had different internal characteristics even in symmetrical position of the coil. *Axis* boundary condition was obviously fixed to the remaining edge. Solution approach was based on pressure-velocity coupling and their relationship was calculated using COUPLED algorithm; the intense vorticity of the flow was taken into account by interpolating pressure in the calculation by PRESTO! scheme. No changes in the shape of the free surface under the effect of the magnetic field were taken into account. COUPLED algorithm enables full pressure-velocity coupling, solving the momentum and pressure-based (2.39) continuity equations together. It obtains a more robust and efficient single phase implementation for steady-state flows. PRESTO! avoids interpolation errors and pressure gradient assumptions on boundaries; this scheme suits for problems with strong body forces and hight Rayleigh number flows (e.g. natural

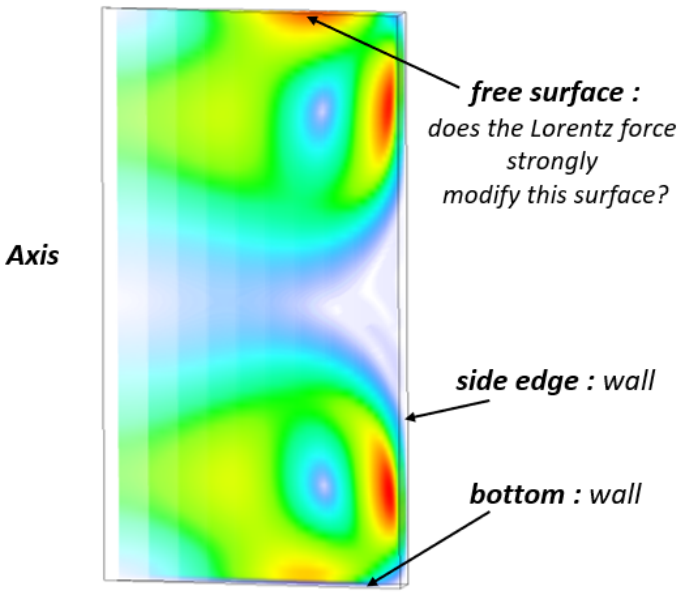

Fig. 3.9: Boundary conditions on GalInStan melt region.

Line	*Boundary condition*
side edge	stationary wall, no slip
bottom	stationary wall, no slip
symmetry axis	axis
free surface	stationary wall, specified shear

Table 3.3: Summary of fixed boundary conditions for GalInStan melt.

ventilation). Significant computational cost is though required.

After hydrodynamic solution was calculated, time average velocity distribution was evidenced inside GalInstan melt; therefore, first simulation results were checked for excluding any evident error: for symmetrical position of the inductor (*Inductor Position Zero*), two toroidal eddies were definitely achieved, with almost the same energy, amplitude and velocity (Fig.3.10); specific shear boundary condition on the free surface partially influenced liquid's behaviour in a way that it allowed the generation of superficial fluctuations and local velocity increased next to the free surface. Orthogonal velocity vectors to the bottom and side edge were absent, thus the application of other boundary conditions was correct (Fig.3.11).

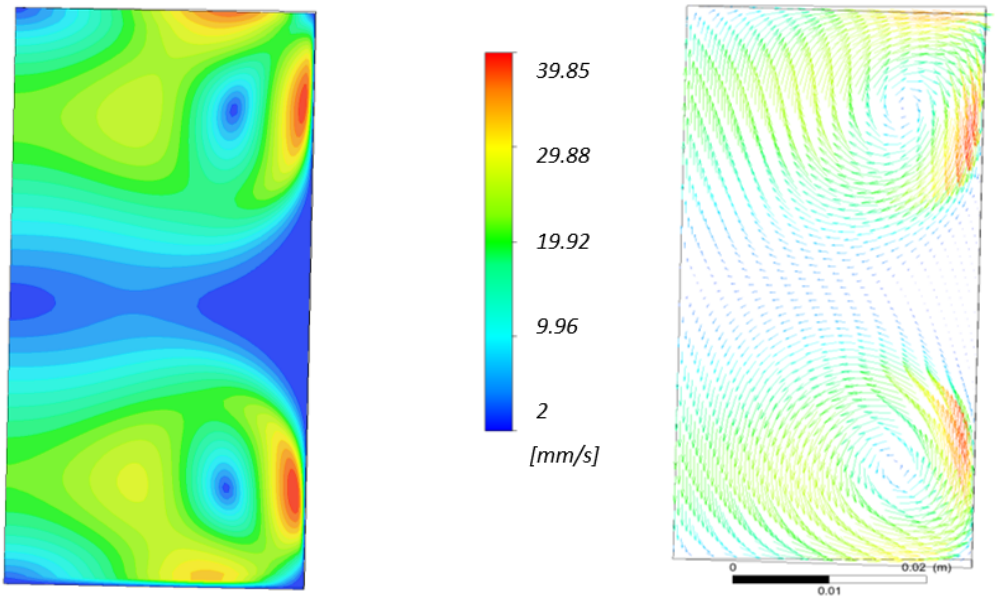

Fig. 3.10: Average velocity distribution, isosurfaces; check of hydrodynamic solution. Two toroidal vortices are evident in pictures, as expected, with almost the same amplitude. Velocity range goes from $2[mm/s]$ to $39[mm/s]$. Boundary conditions applied to bottom and side edge, correctly produce zero local velocity of the flow next to them.

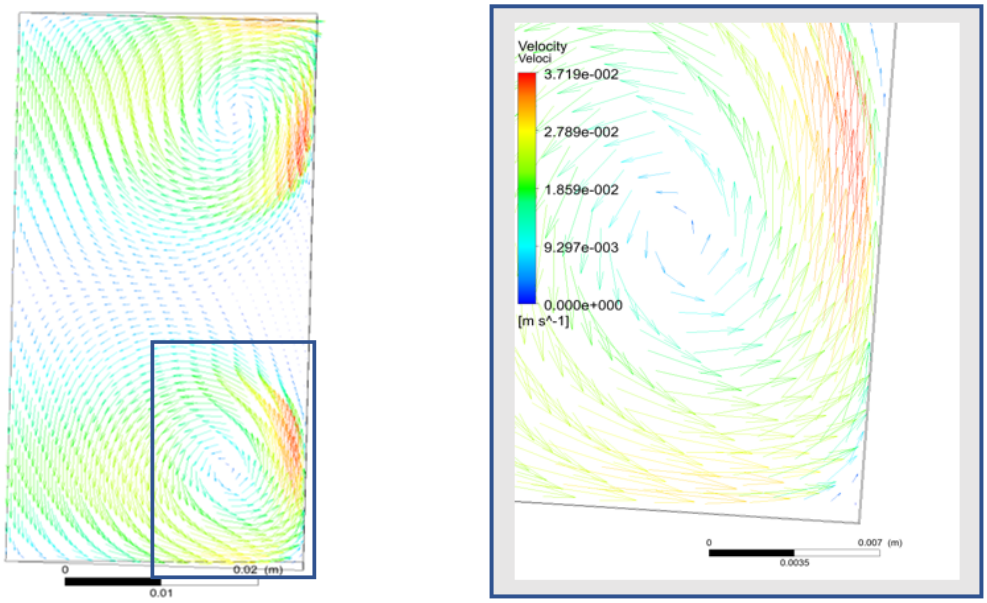

Fig. 3.11: Average velocity distribution, vectors; check of hydrodynamic boundary conditions. No velocity vectors are orthogonal to bottom or side edge.

3.2.3 Steady state solution: from *Inductor Position Zero* to *Inductor Position 6*

In this section, numerical model results will be shown. Electromagnetic and hydrodynamic simulations were coupled with the aim of investigating flow pattern inside the melt and the analysis of the transition from two-to-one vortices was carried on during inductor's upward movement. In order to do that, Lorentz force distribution in harmonic regime was firstly calculated, then time average velocity of liquid was displayed; both of them were calculated in steady state regime and for each position of the coil. With the aim of recognizing the transition though, the following results will show significant solutions only and not all of inductor's positions will be displayed.

For Lorentz force:

- amplitude
- distribution

were analysed, to evaluate its maximum magnitude and validate the shape of resulting vortices inside the liquid. For velocity of the melt:

- global distribution
- magnitude and highest velocity zones
- axial component of velocity along melt's vertical axis
- axial component of velocity next to the wall

were analysed. All of these results were necessary to put in evidence resulting flow pattern inside GalInStan melt and how the two vortices behaved. As already stated, AMF application to cylindrical crucibles produces strong motion and mixing effect in the central region of melt, along the border between the two eddies; velocity axial component was therefore evaluated along two patterns, to quantify mixing effect inside the most significant region for melt's motion. The first pattern was created along symmetry axis of the melt, while the second one was fixed along the wall of the crucible, more precisely 4 [mm] far from its border (Fig.3.12). This gap was necessary to simulate real experimental setup and take into account UDV probe physical dimensions: its diameter corresponded to 8 [mm] and produced a measurement pattern which was not exactly close to cylinder's wall. In this way, influence of the wall on melt's velocity was also skipped, thus natural turbulence was analysed. Chosen reference system along the pattern went from the free

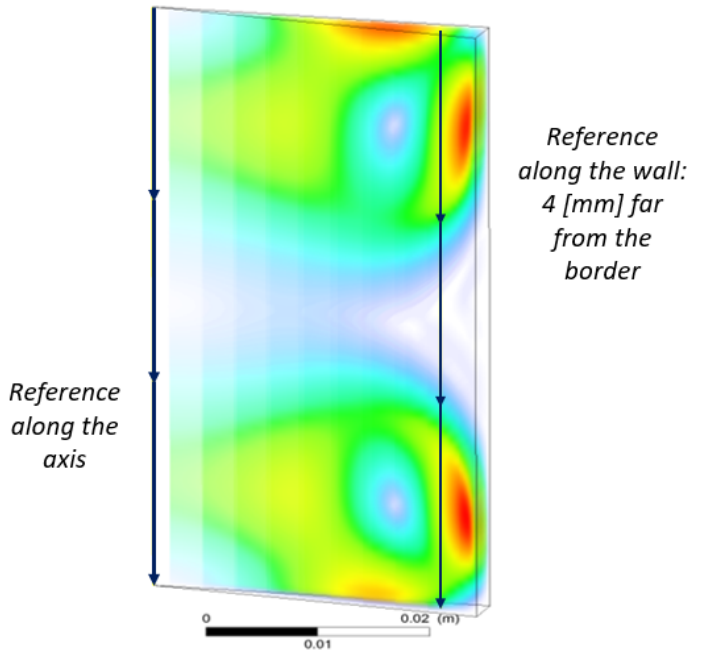

Fig. 3.12: Patterns for axial velocity measurement inside GalInStan melt. Both pattern along the axis and next to the wall have been evidenced.

surface of melt to its bottom. Tangential component of velocity to the reference was the most significant for this investigation, thus it was the only one displayed.

The following pictures (Fig.3.13-3.17) show numerical simulation results and, with the aim of investigating two-to-one vortices transition, they could be commented like that: two toroidal eddies were achieved in *Symmetry Position* of the inductor; they had almost the same energy, dimension and velocity as direct consequence of a symmetrical distribution of Lorentz force. Strong motion was generated in the central region of the melt, thus intensive heat and mass transfer was produced. *Free surface* boundary condition partially influenced turbulences development in the top of the crucible. Global range of average velocity inside GalIStan melt went from 2 [mm/s] to 39 [mm/s] and maximum velocities of the flow corresponded to around 20 [mm/s] along the axis and 25 [mm/s] along wall pattern. Symmetrical distribution of Lorentz force was not present anymore when simulation moved the inductor to *Position 1*: maximum of Lorentz force moved upward too, increasing amplitude of the lower vortex and decreasing the upper one. Velocity of the flow next to the wall reduced more in the lower vortex than for the top one but the opposite thing happened for velocity along the axis. Such a difference was more evident as the inductor shifted to its top position. Pictures below clearly show axial velocity component achieved from simulation results for different positions of the inductor: wall velocity was strongly influenced by the presence of plexiglass vessel and

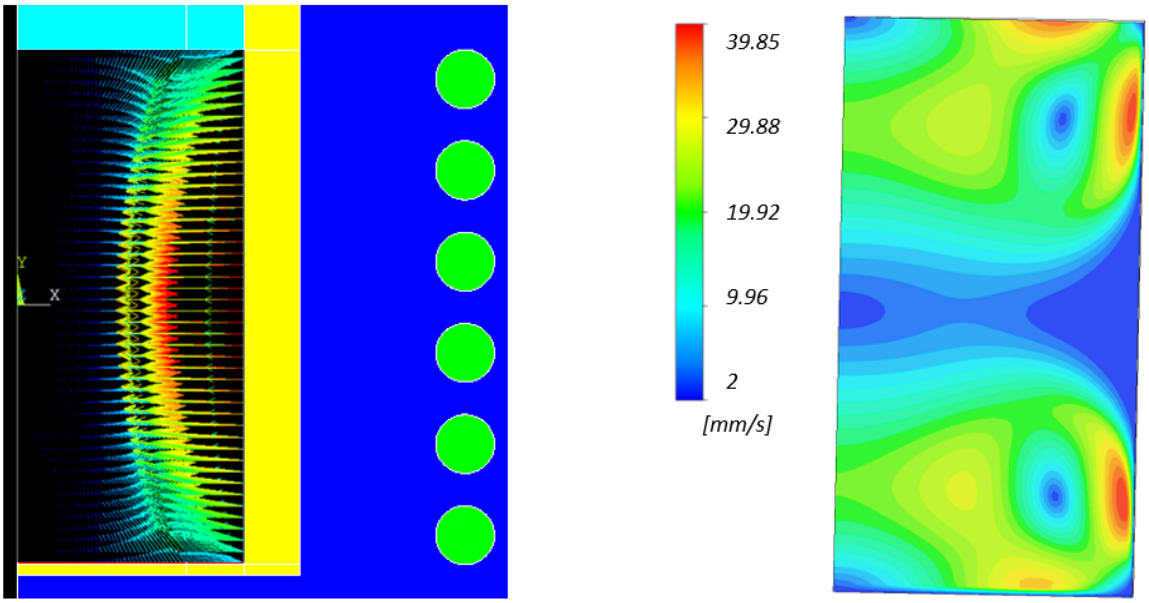

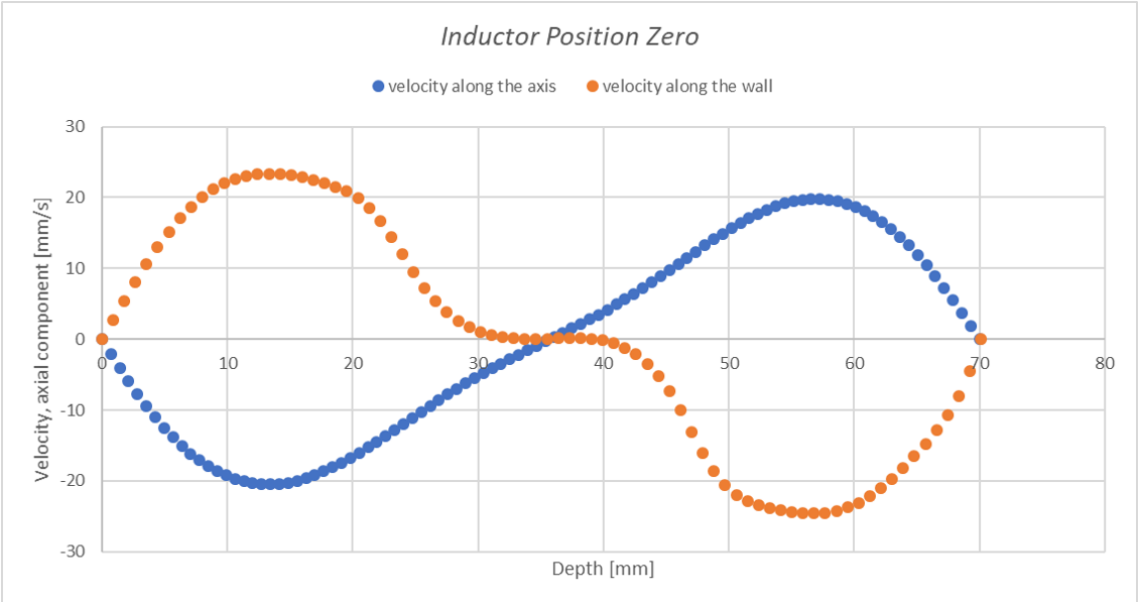

Fig. 3.13: *Inductor Position Zero*: simulation results. Lorentz force volumetric density (left) is included in a range of $[10^{-8} \div 0.5 \cdot 10^{-4}][N/m^3]$. Average velocity of the flow (right) in a range of $[2 \div 39][mm/s]$.

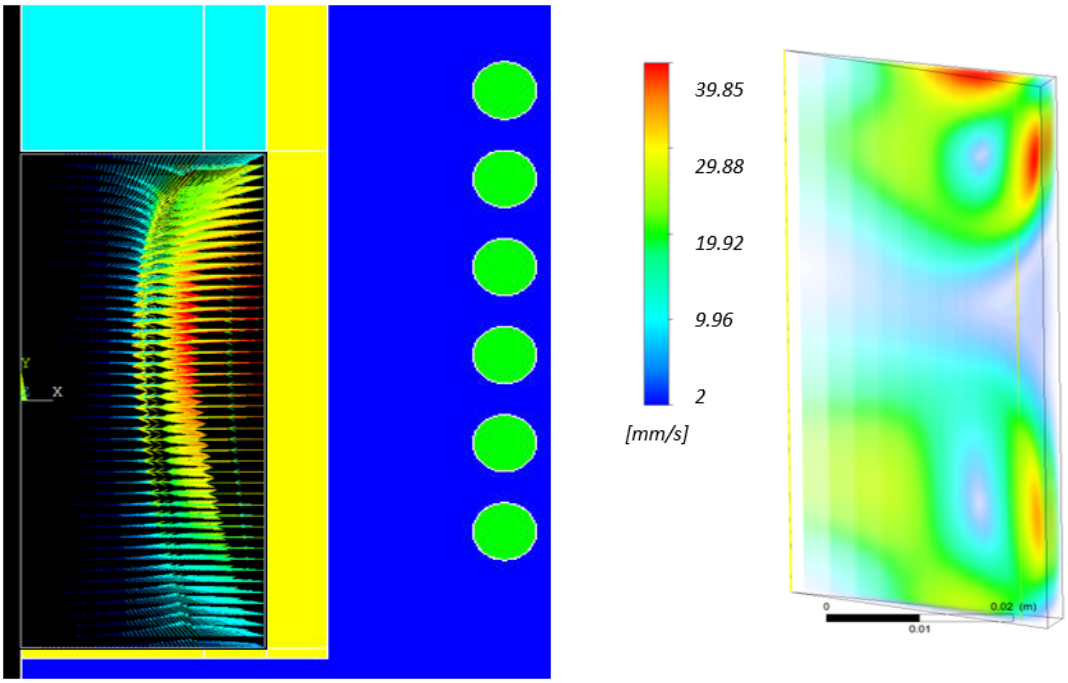

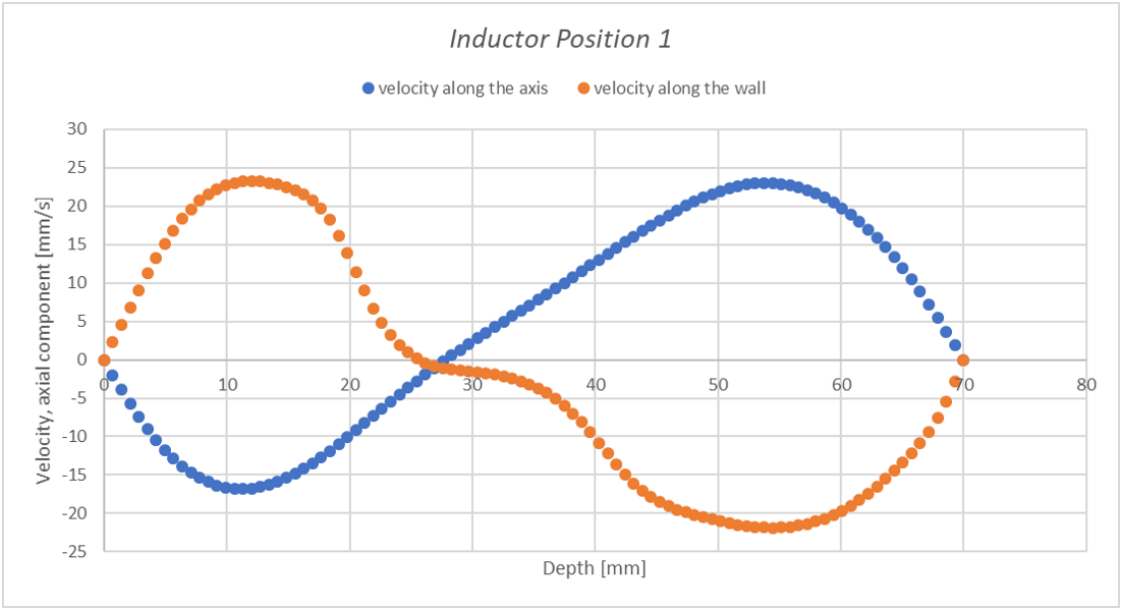

Fig. 3.14: *Inductor Position 1*: simulation results. Lorentz force volumetric density (left) is included in a range of $[10^{-8} \div 0.5 \cdot 10^{-4}][N/m^3]$. Average velocity of the flow (right) in a range of $[2 \div 37][mm/s]$.

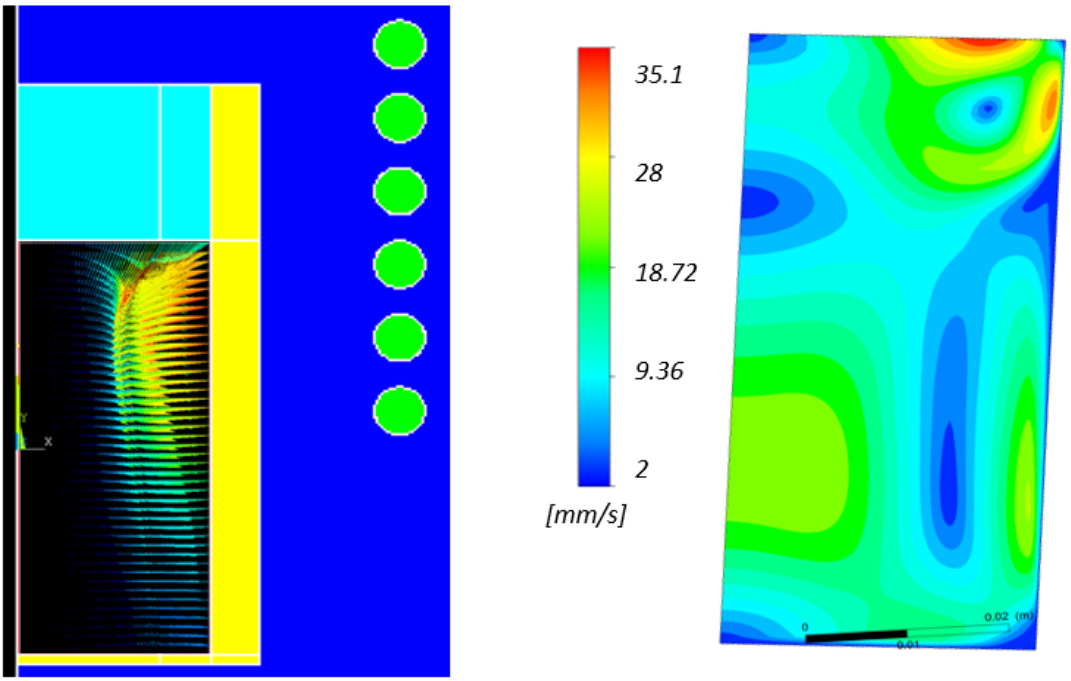

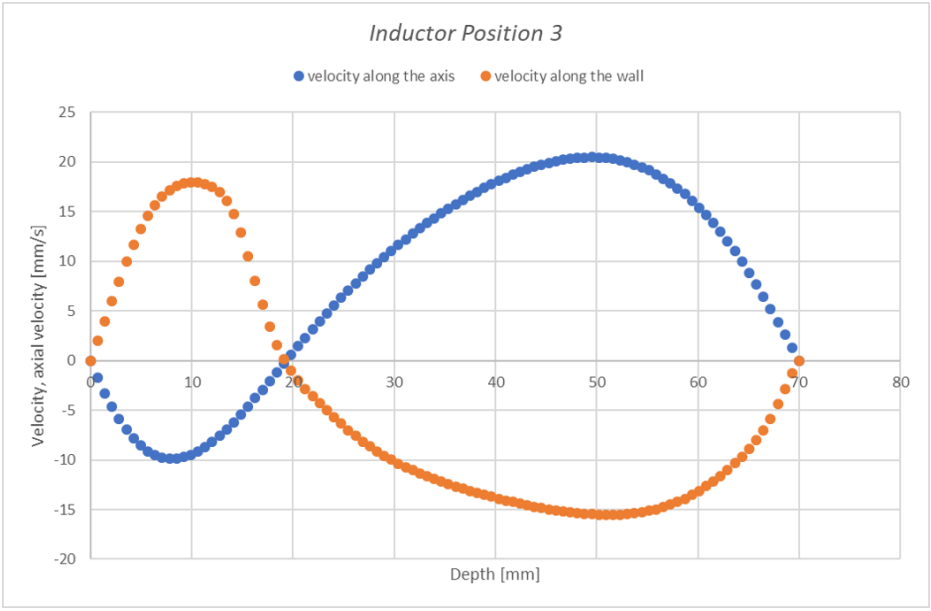

Fig. 3.15: *Inductor Position 3*: simulation results. Lorentz force volumetric density (left) is included in a range of $[10^{-8} \div 0.5 \cdot 10^{-4}][N/m^3]$. Average velocity of the flow (right) in a range of $[2 \div 35][mm/s]$.

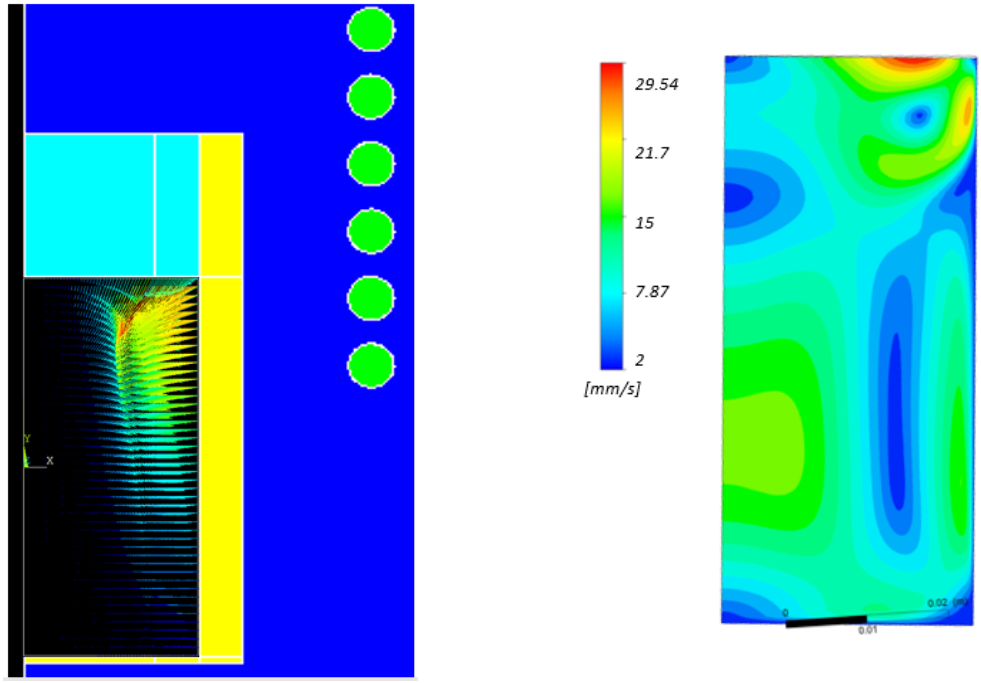

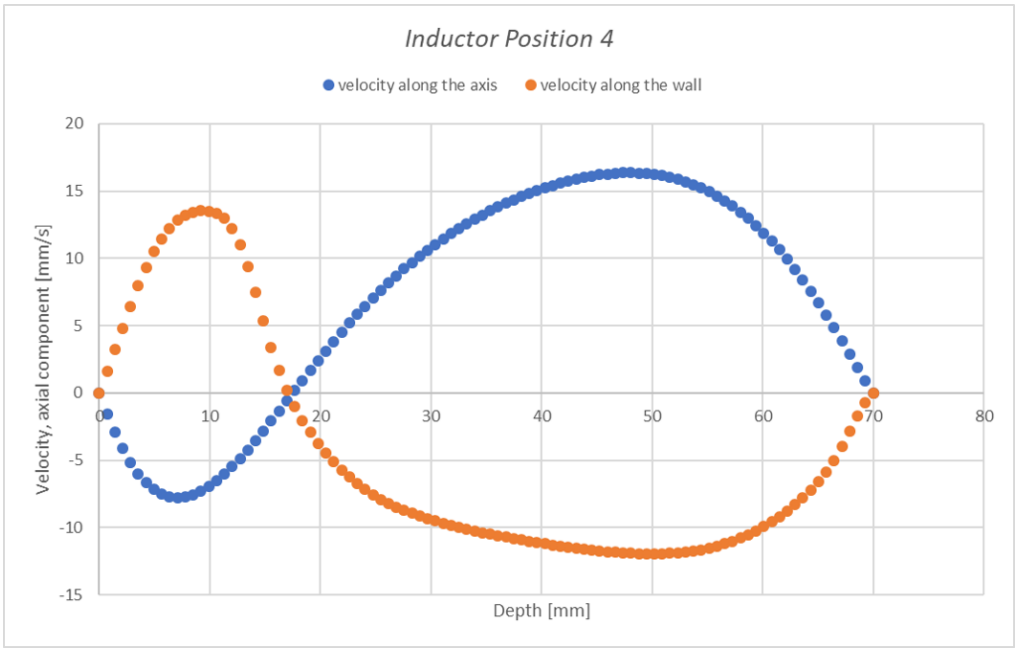

Fig. 3.16: *Inductor Position 4*: simulation results. Lorentz force volumetric density (left) is included in a range of $[10^{-8} \div 0.4 \cdot 10^{-4}][N/m^3]$. Average velocity of the flow (right) in a range of $[2 \div 29][mm/s]$.

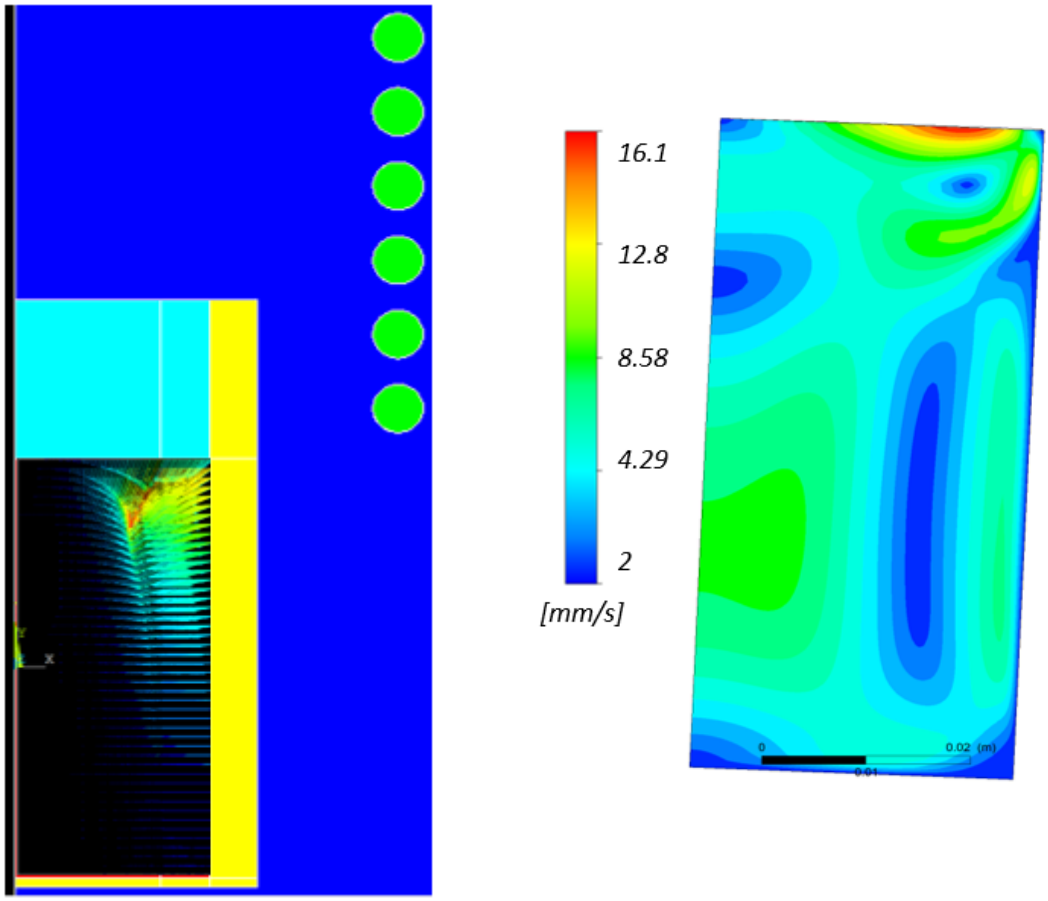

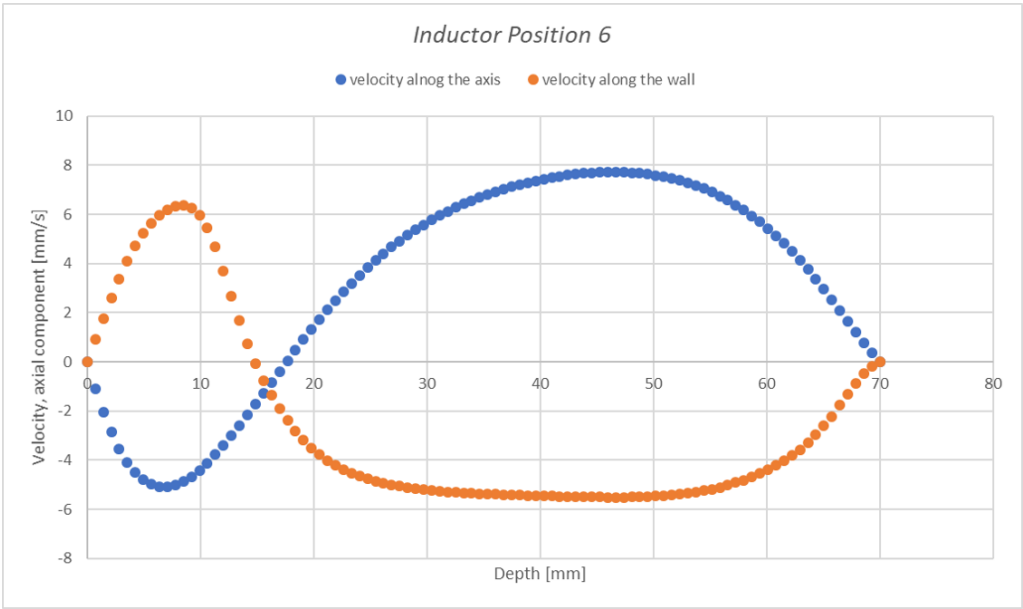

Fig. 3.17: *Inductor Position 6*: simulation results. Lorentz force volumetric density (left) is included in a range of $[10^{-8} \div 0.2 \cdot 10^{-4}][N/m^3]$. Average velocity of the flow (right) in a range of $[2 \div 16][mm/s]$.

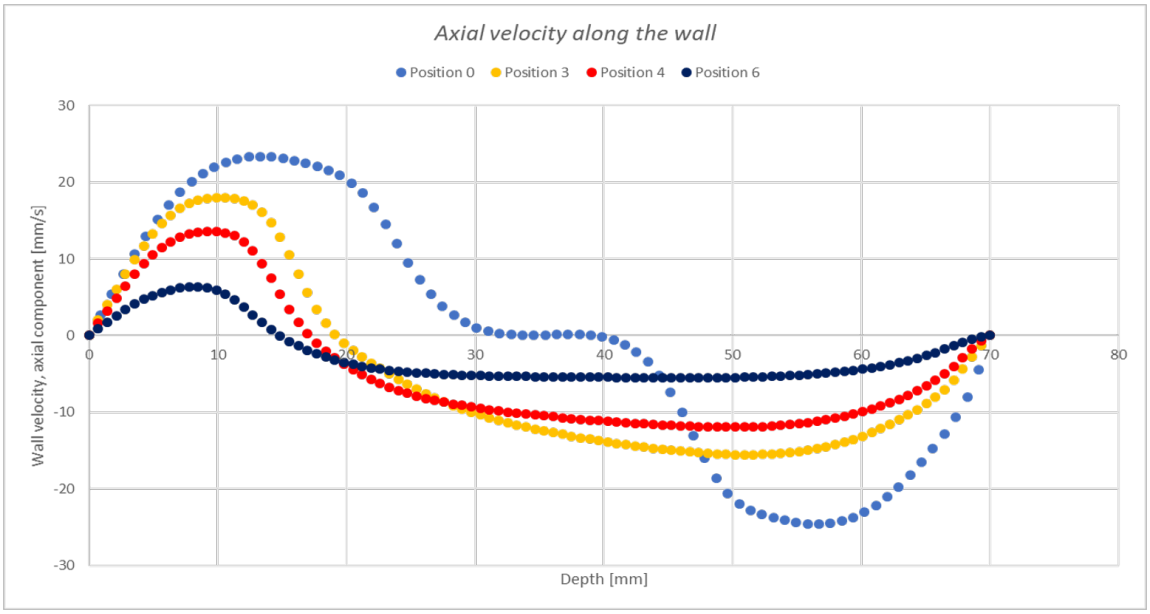

Fig. 3.18: Axial velocity component along the wall for different positions of the inductor.

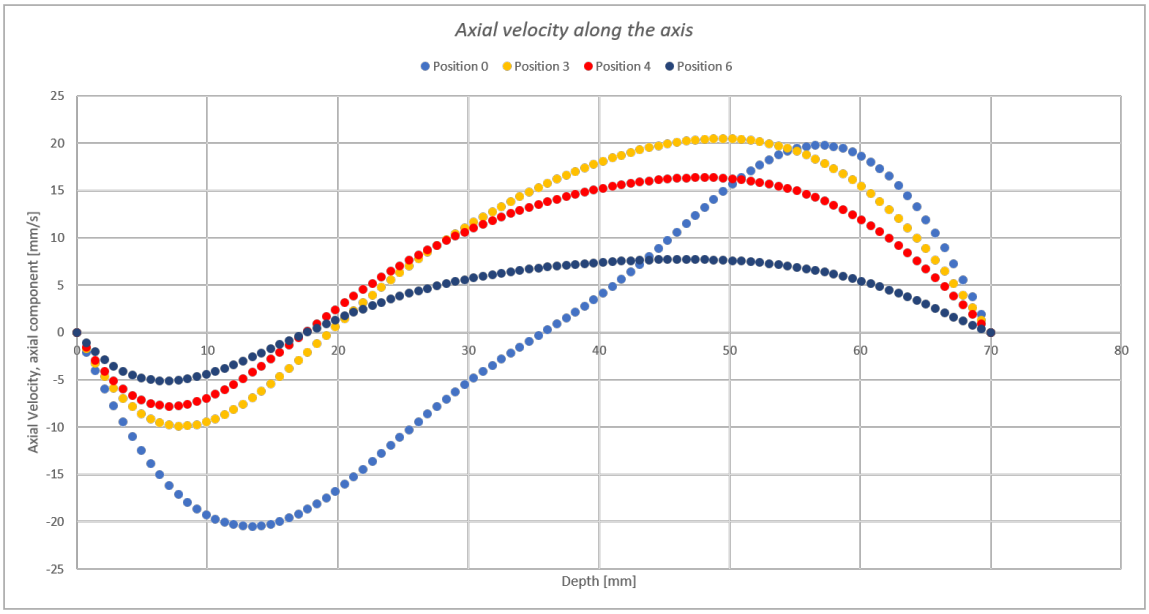

Fig. 3.19: Axial velocity component along the axis for different positions of the inductor.

rapidly decreased the more the coil shifted upward; axial velocity along the axis globally decreased too but its shape was mostly conserved. Simulation results from *Position 3* and *Position 6* empathise the initial behaviour of the system: the more the inductor got close to its top position, the more Lorentz force vectors pointed towards melt's bottom surface and the more its amplitude decreased. Therefore, lower vortex continuously increased while the upper vortex increased in their dimensions. Average velocity decreased for both of them. Maximum velocity along the wall reached 6 [mm/s] for the both eddies in last position, while lower vortex measured 8 [mm/s] along the axis.

Experimental activity on the same setup was carried out in parallel with simulations to validate numerical results: Lorentz force was not taken into account during practical activity while axial velocity of the flow was measured using the UDV probe; it was fixed on the top of plexiglass vessel thus the same measuring patterns adopted for simulations were achieved (Fig.3.20). Velocity along the pattern was measured in 80 points and the resulting curve was the average between around 1200 curves; this number was chosen to achieve uniform behaviour in the final curve. All of them have been measured after the system reached its steady state regime and, thanks to transient hydrodynamic simulation, interval of time necessary for the flow to reach steady state regime was calculated around 40 [s]. Axial velocity measured experimentally along the wall did not fit the simulated

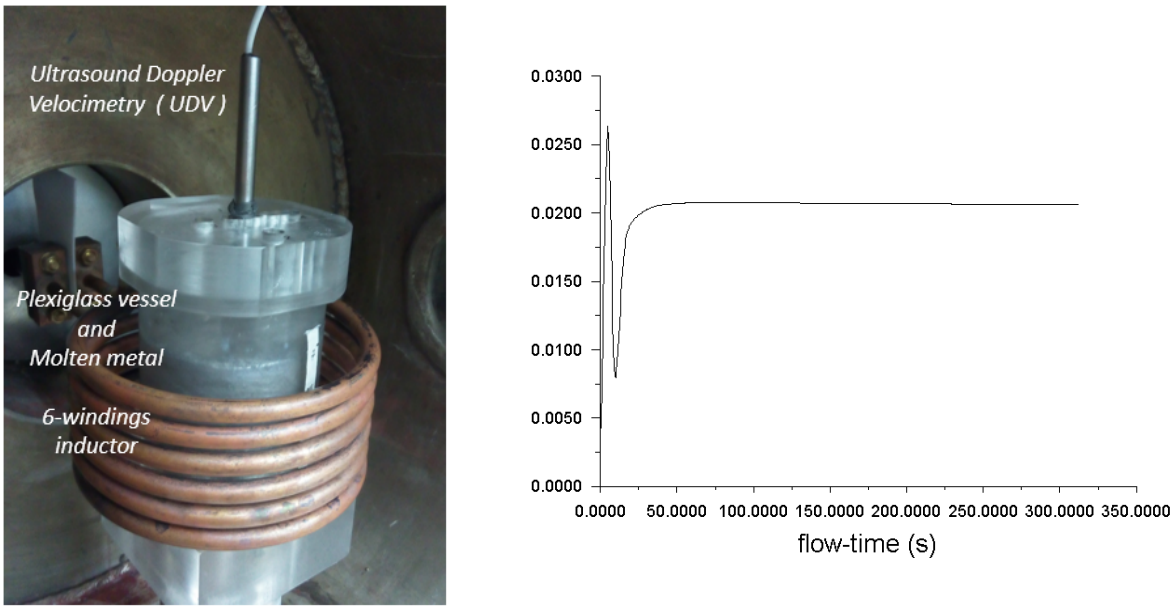

Fig. 3.20: Experimental setup for validation of simulation results (left) and velocity magnitude over time [mm/s] for steady state regime calculation (right).

one in a good way, in the bottom section of melt especially: such a gap was probably due to the same presence of the vessel, thus both the amplitude and maximum velocity of vortices were influenced. Peak velocity of the lower vortex measured during experimen-

tal activities was 33.19 [mm/s], while simulations produced 23.30 [mm/s] for the same parameter. Furthermore, the two vortices had the same velocity, amplitude and energy in simulations; lower vortex measured to be bigger and faster in experiments. The global shape of velocity along the wall was acceptable (Fig.3.21). Therefore measure for *Inductor Position Zero* was achieved only. Good results were produced from velocity along the axis (Fig.3.22-3.24): *Symmetrical* position of the inductor showed two similar vortices in both simulated and measured curve and small variations in shape depended from internal instabilities of the flow. Measured shape of the lower vortex significantly fits with the calculated curve even if vortex velocity on the top region was really difficult to measure properly; for all of the inductor positions, measured curves had a flat behaviour, corresponding to most of the upper vortex amplitude. One small part of each curve only properly corresponded to the simulated ones. Null measured velocity in the initial part of depth was maybe affected by presence of UDV probe, which was drawn for 2-3 [mm] within the melt to achieve good measurement of inside the liquid metal; vortices on the top region of melt kept in contact with the probe and their velocity was thus strongly reduced.

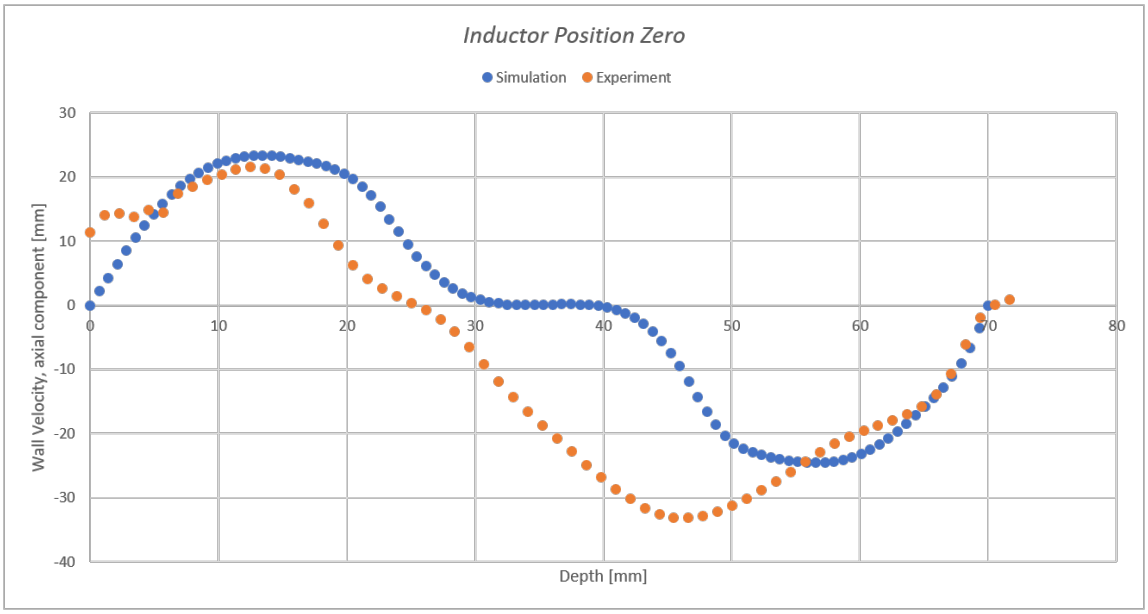

Fig. 3.21: Comparison between simulated and measured axial velocity along the wall. Experiment maximum measured velocity: 33.19 [mm/s]; simulation maximum velocity: 23.30 [mm/s].

Final remarks must be dedicated to solution's method of the numerical model: comparison between simulated and measured velocities confirmed that the choice of $k-\varepsilon$ model was right, especially if compared with the $k-\omega$; average velocity distribution achieved with $k-\omega$ model showed significant concentration of turbulences and higher velocity of vortices in a small region confined next to melt's corners (Fig.3.25). Velocity

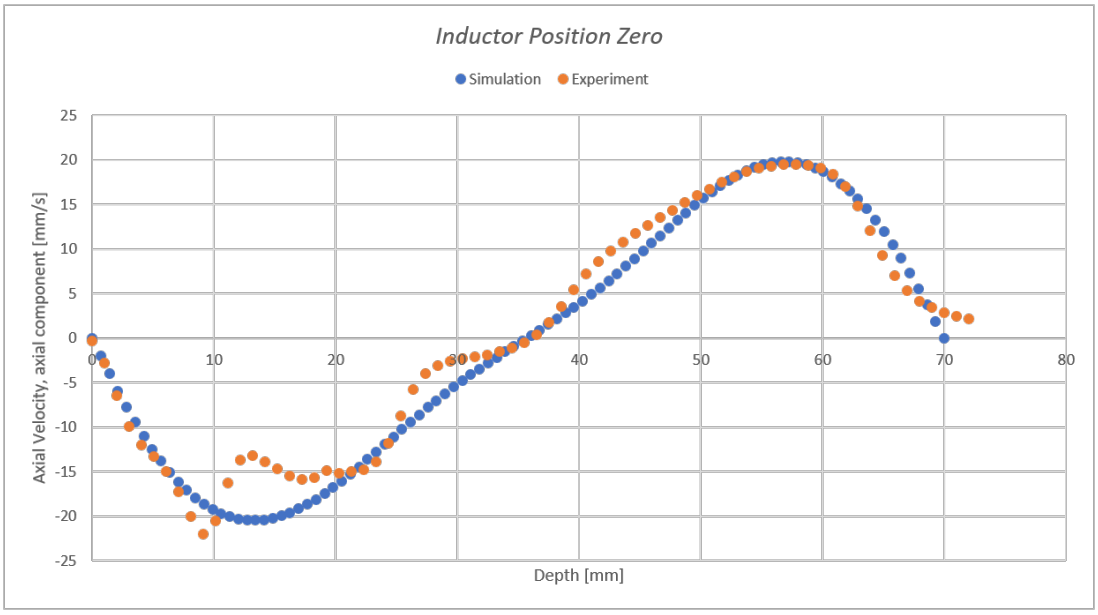

Fig. 3.22: Comparison between simulated and measured axial. *Inductor Position Zero*. Experiment maximum measured velocity: 22.04 [mm/s]; simulation maximum velocity: 20.47 [mm/s].

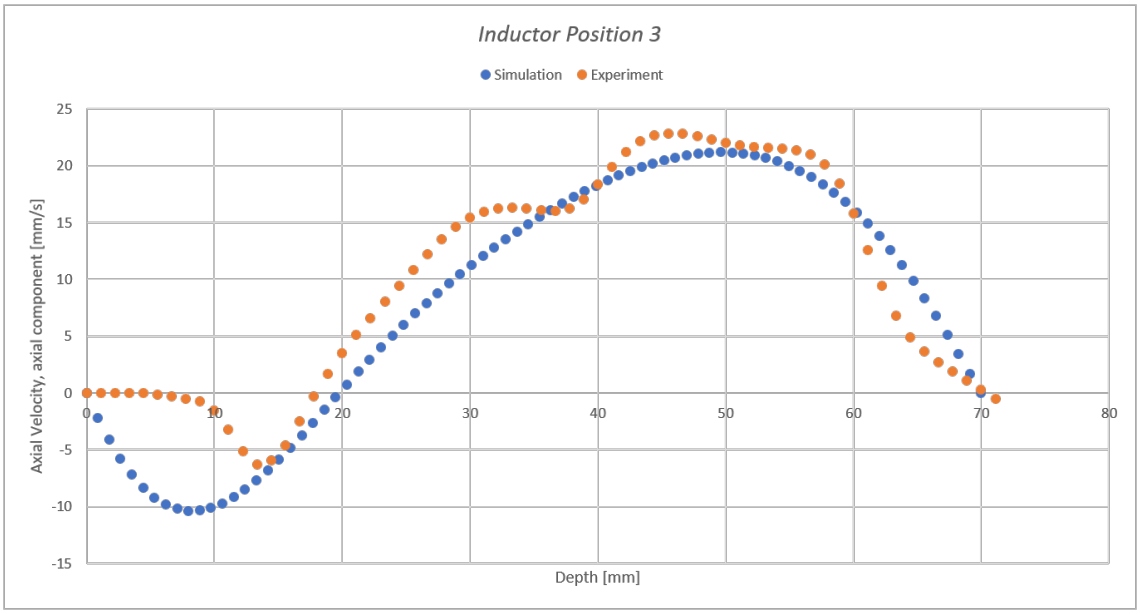

Fig. 3.23: Comparison between simulated and measured axial. *Inductor Position 3*. Experiment maximum measured velocity: 22.84 [mm/s]; simulation maximum velocity: 21.19 [mm/s].

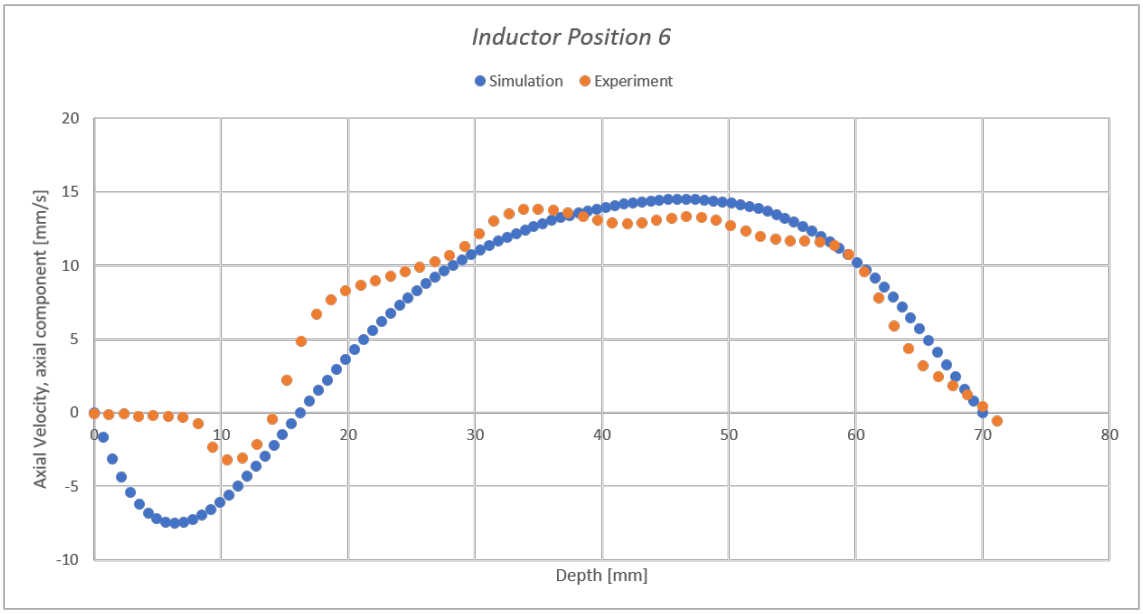

Fig. 3.24: Comparison between simulated and measured axial. *Inductor Position 6*. Experiment maximum measured velocity: 13.82 [mm/s]; simulation maximum velocity: 14.48 [mm/s].

distribution was really low in a big, central region of the liquid, thus amplitude of the two toroidal eddies resulted extremely reduced and global behaviour of simulated axial velocity was different from measured one, both in shape and magnitude. Convergence to solution was achieved with number of iterations which was twice than the one for $k - \varepsilon$ and peak of simulated axial velocity along the axis was much lower (around 8 [mm/s] over 20.47 [mm/s] for $k - \varepsilon$ model).

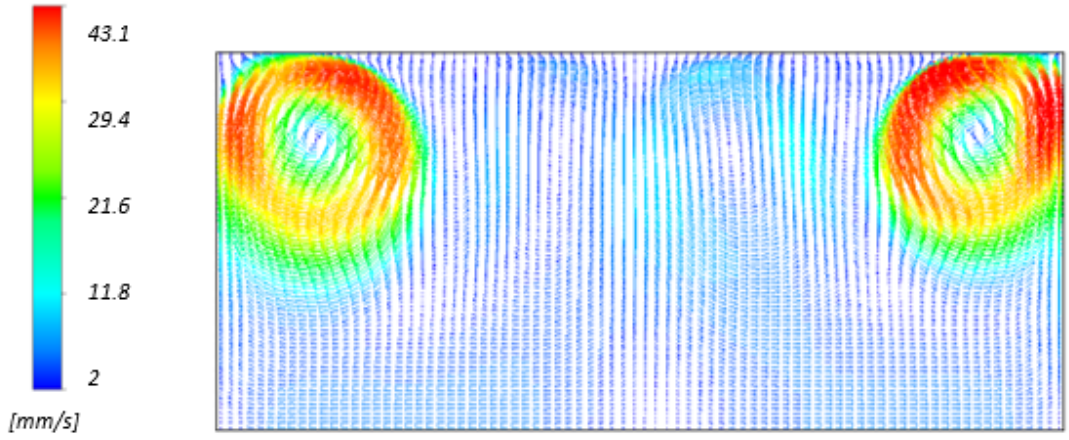

Fig. 3.25: Average velocity distribution achieved with $k - \omega$ model. Melt region is on horizontal position, axis of the cylinder appears below.

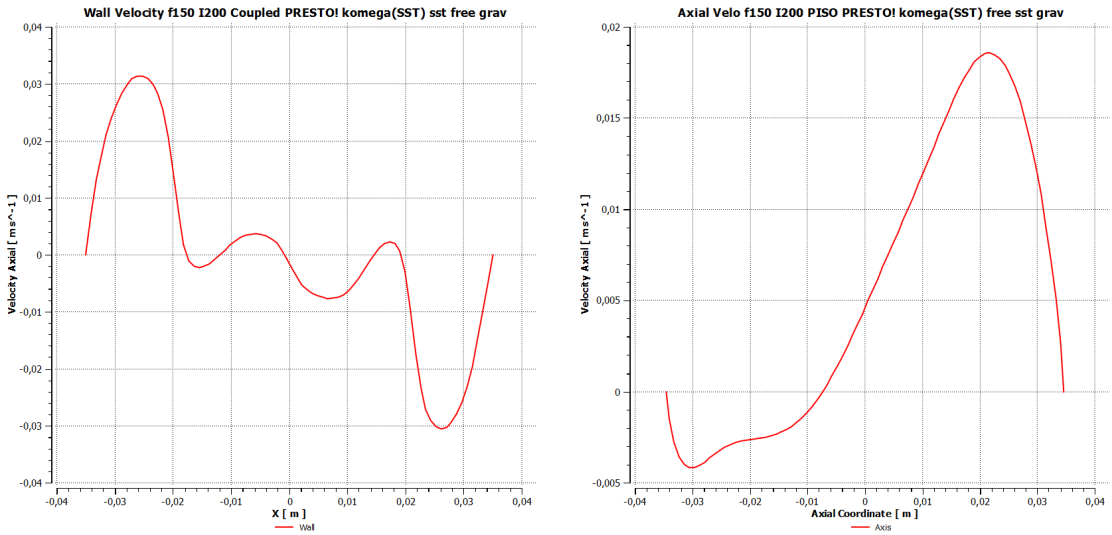

Fig. 3.26: Axial velocity along the wall (left) and along the axis (right) achieved with $k-\omega$ model.

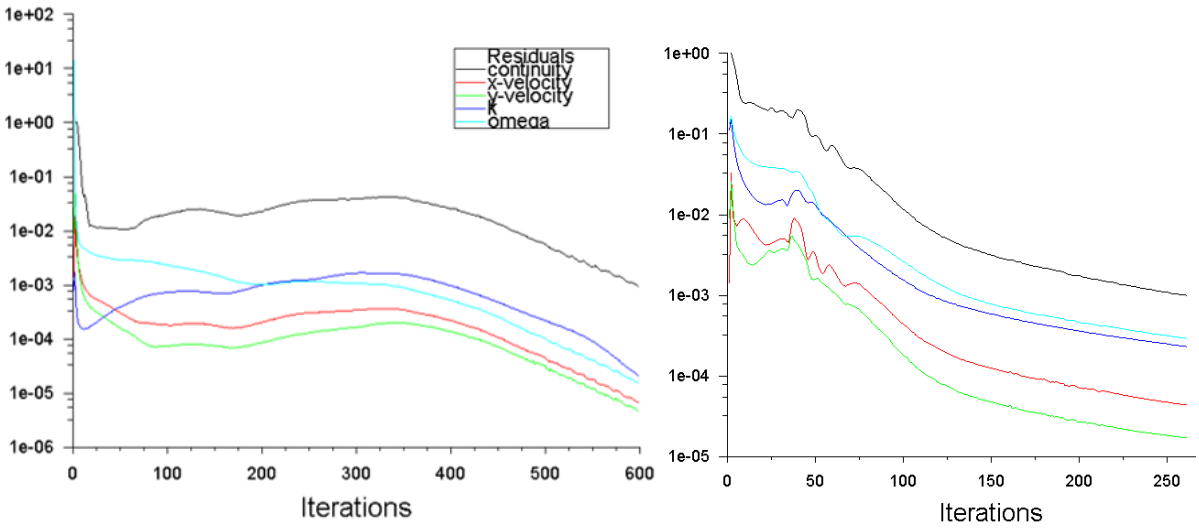

Fig. 3.27: Residual behaviour over number of iterations for $k-\omega$ model (left) and $k-\epsilon$ (right).

Chapter 4

PMF application

4.1 Procedure of optimization for PMF application

4.1.1 Analysis of results from AMF application

Good correspondence between numerical and experimental results gave the possibility to properly continue with the investigation of the transition from simulated curves. Two main criterion where then chosen:

1. ***if*** the transition happened. From a general point of view, transition from two-to-one vortices was fixed to happen in the case amplitude of the lower vortex did not increase anymore during coil's upward movement. In the opposite way, amplitude of top eddy reduced significantly; its amplitude and velocity were evaluated to understand if they were significant again for the inductor in *Position 6*.

2. ***when*** the transition happened. In the case transition was verified, amplitude of the lower vortex was much bigger than the upper one and their dimensions were then calculated to fix PMF parameters.

In a more specific way, adopted convention to establish when the transition happened was that amplitude variation of the lower vortex became smaller than ***5%***; velocity curves for different inductor positions were adopted to achieve this goal. Variations of amplitude were not calculated referring to the symmetrical configuration but according to the two subsequent steps of inductor's movement, thus the following formula was adopted:

$$\Delta a_{\%} = \frac{A_{p+1} - A_p}{A_p} * 100$$

where A_{p+1} is the amplitude of lower vortex at *Inductor Position* $p+1$ and A_p represents the same amplitude with the inductor in the previous position. From the investigation of

amplitude variation, it was found that was definitely taking place between *Inductor Position 3* and *Inductor Position 4*, when coil overcame almost half of melt's height (Fig.4.1). A big relative gap was noticed between the two positions and, from *Inductor Position 4* amplitude of the lower vortex was not supposed to change in a significant way anymore. Therefore, from previous results, procedure of optimization of PMF application started and the following investigation was based on the analysis of three positions of the inductor: *Symmetry Position*, *Inductor Position 3* and *Inductor Position 6*; all of them represented significant moments of vortices and their velocity behaviour, for the transition especially. Geometrical parameters of eddies were the initial data for calculation of the *characteristic frequency* f_{ch} of vortices in each position, thus the evaluation of *pulsed frequency* f_p to fix for pulsed current feeding the inductor. As already stated, this investigation wanted to prove that resonance could be achieved not with *pulsed frequency* only but with the application of a range of frequencies around that one too; further investigations were carried out with the application of pulsed frequency far away from f_{ch}, to make evident that resonance could not be achieved in those conditions, but the same stirring effect registered with AMF only.

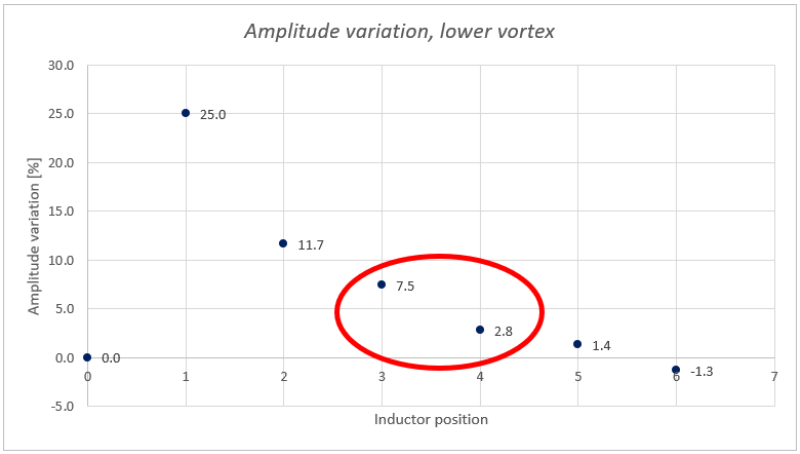

Fig. 4.1: Percentage of amplitude variation over inductor's movement.

4.1.2 Current signal for PMF application

Optimization of PMF application was carried out with experimental activities only. No simulations were created because transient and too complex numerical models would have been necessary, thus high computational time. Pulsed signal was therefore manually calculated, then it was implemented in the generator.

Main characteristics of pulsed current were fixed starting from the evaluation of dimensional parameters of vortices during inductor's movement; global length of each eddy

Parameter	*notation*	*unit*	*I.P. Zero*	*I.P. 3*	*I.P. 6*
eddy size, radial	r_r	[mm]	7.75	7.75	7.75
eddy size, axial	r_z	[mm]	17.5	25.5	26.5
length	L_{ch}	[mm]	79.3	104.3	106.6
velocity	v_{ch}	[mm/s]	22.5	18	6.85
revolution period	T_{ch}	[s]	3.52	5.8	15.56
frequency	f_{ch}	[Hz]	0.28	0.17	0.064
pulsed frequency	f_p	[Hz]	**0.3**	**0.2**	**0.1**

Table 4.1: Characteristic parameters of melt flows in three main positions of the inductor. Relationship between parameters of vortices and electromagnetic quantities can be noticed.

L_{ch} and characteristic velocity v_{ch} were initially analysed, thus characteristic frequency as the inverse of characteristic period T_{ch}. The notation was adopted by the authors of Ref. [23] and formulas for achieving characteristic frequencies were the following:

$$L_{ch} = 2\pi \cdot \frac{r_r + r_z}{2}; \qquad v_{ch} = \frac{V_{max,wall} + V_{max,axis}}{2};$$

$$T_{ch} = \frac{L_{ch}}{V_{ch}}; \qquad f_{ch} = \frac{1}{T_{ch}}$$

Precise value of each characteristic frequency was obviously impossible to fix for the signal, therefore pulsed frequency was approximated with more suitable values for experimental activities (last line of (Table 4.1)). Figure 4.2 shows what the applied current was: pulses alternated with null signal with the same time ratio and each pulse was generated starting from the sinusoidal wave adopted for AMF application. Let us call T_p the revolution period of pulsed current; it was the sum of an interval of time during which the signal was zero (T_0) and a pulse time (T_{act}):

$$T_{act} + T_0 = T_p; \qquad T_p = \frac{1}{f_p}$$

Each pulse was fixed to last for the same time of null signal, thus ratio:

$$\Psi = \frac{T_{act}}{T_0} = 1$$

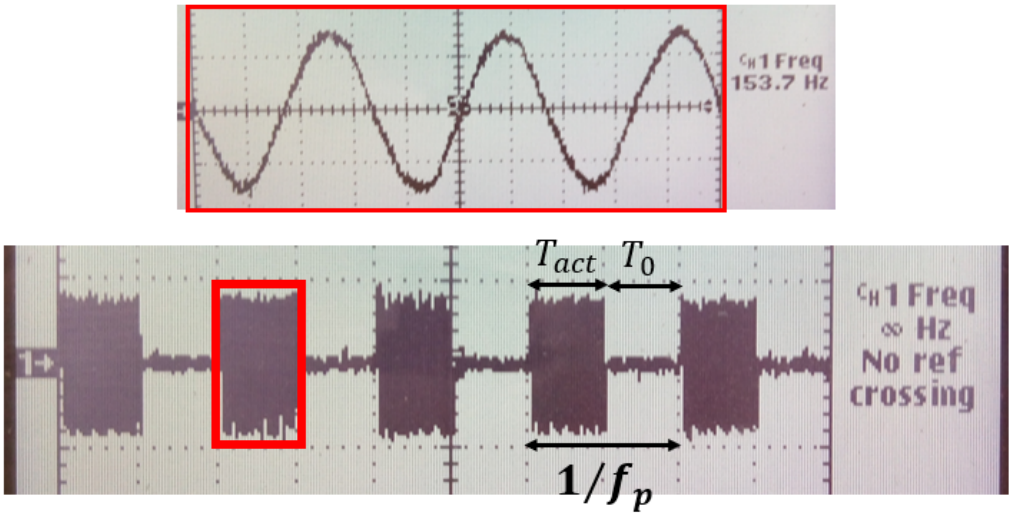

Fig. 4.2: Pulsed current was generated starting from sinusoidal wave adopted in AMF application. Each pulse was built with a specific number of sinusoidal waves, depending on the value of pulsed frequency.

and pulses were made with a sequence of sinusoidal waves, whose frequency was $f_{AC} = 150$ [Hz]. Specific number of sinusoidal waves inside each pulse depended from chosen pulsed frequency. Experimental activity of PMF application was carried on with using current generator provided by ELOTHERM SMS Group, which allowed to modify shape, frequency and amplitude of the output signal by transistor circuits. RMS value of pulsed current was calculated from the energy equivalence: energy absorbed by the inductor during AMF application (alternated current) was fixed to be equal to the one of PMF conditions

$$E_{AC} = P_{AC} \cdot \Delta t_{AC} = P_p \cdot \Delta t_p = E_p$$

where Δt_{AC} was the considered interval of time in the case of sinusoidal wave, while Δt_p was the same interval when pulsed signal was taken into account. $P = r \cdot I^2_{RMS}$ represented the electric power. Therefore, amplitude of pulsed current was:

$$I_{p,RMS} = \sqrt{\frac{\Delta t_{AC}}{\Delta t_p} \cdot I^2{}_{AC,RMS}} = 282[A]$$

The range of applied frequencies for pulsed signal included both expected resonance frequencies and those values which were not supposed to produce resonance condition. In order to produce a precise experimental investigation, all of the different frequencies of pulsed current were applied to all inductor positions:

- $f_p = [0.1, 0.2, 0.3, 0.5, 1, 2, 4, 5][Hz]$ range of applied pulsed frequencies

- $I.P. = [0, 1, 2, 3, 4, 5, 6]$ set of inductor positions

In this way, behaviour of the flow under pulsed conditions was completely analysed.

4.2 Experimental results

Equation (2.45) already evidenced that instantaneous velocity is made of mean value and pulsed component; main aim of experimental activities with PMF was to evaluate turbulence intensity of the flow for different frequencies of supplied current, thus quantify influence of resonance during two-to-one transition. In order to do that, *pulsed component* of axial velocity along the axis was taken into account and two characteristics of this velocity were calculated:

- average standard deviation
- fast fourier transform (*fft*)

All of inductor's positions were tested and results from the application of pulsed signal were always compared with the steady state ones, following the same pattern that authors of Ref. [22, 23] adopted.

In the case of standard deviation analysis, results for *all* of the pulsed frequencies were summarized in a unique diagram for each position, to put in evidence increase in turbulence intensity with the application of different electrical parameters. Application of steady state signal produced an horizontal row, fixed on a unique deviation value, due to the fact that instantaneous velocity corresponded to its average value only, and pulsed component was absent; on the other hand, application of pulsed signal could not produce a continuous curve but standard deviation was characterised by a discrete set of points only, which quantified intensity of turbulence in the flow with that specific value of f_p. Following schemes include experimental results from significant positions only, thus extreme and mid positions of the inductor. The analysis started with taking into account results form previous studies on the same experimental setup, when the inductor was in *Symmetry Position*: application of $f_p = 0.1[Hz]$ and its close values significantly increased standard deviation, if compared with the same in AMF conditions. Confirmation of resonance effect came from diagrams in following inductor's positions: the set of frequencies far from the characteristic one produced flat behaviour of average standard deviation for both *Inductor Position 3* and *Inductor Position 4* (Fig.4.4 and 4.5 respectively), close and below steady signal row; the more f_p pulsed frequency got close to vortices characteristic

frequency, the higher deviation was. A big gap could be noticed between points representing application of PMF and steady signal. Resonance condition produced deviation values corresponding to almost twice of AMF. The same trend was noticed for inductor on its top position (Fig.4.6), even some unexpected points were achieved for $f_p > 1[Hz]$; behaviour for $f_p = [2,3][Hz]$ can be explained with difficulties in the registration of results, due to position of the inductor itself, while standard deviation for $f_p = [5][Hz]$ must be interpreted with the interaction between that pulsed current and melt flows even in unusual conditions. Globally, expected behaviour of standard deviation was correctly achieved with the variation of pulsed frequency during inductor's shifting.

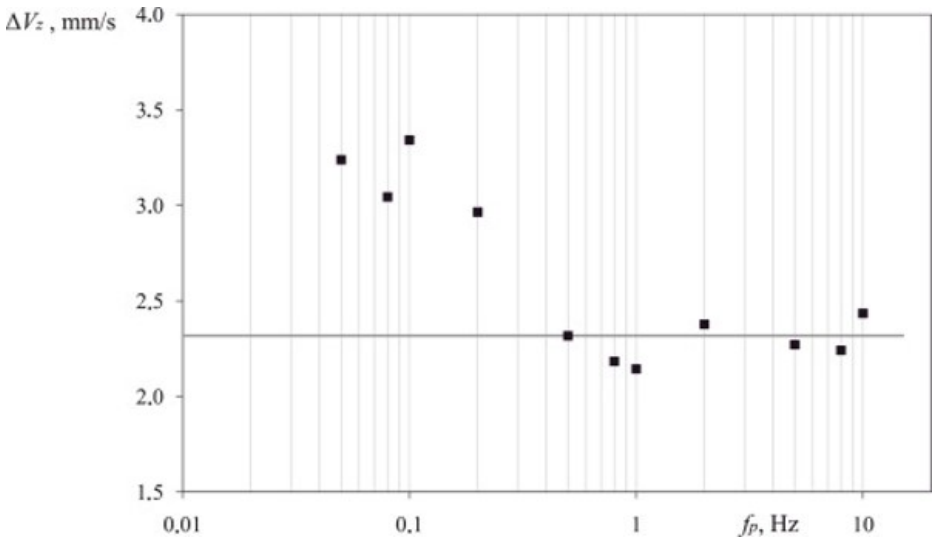

Fig. 4.3: Average standard deviation over f_p pulsed frequency for *Inductor Position Zero*. This graph was taken from previous investigations on the same experimental setup.

Fast Fourier Transform was then applied to pulsed component of axial velocity for validating previous results from standard deviation: in that case *qtiplot* was adopted and results for PMF application were not taken from previous studies but they have been calculated during experimental activities too. Every single pulsed frequency was tested for each position and expected resonance frequencies were represented in fft diagrams, basing on Table 4.1. PMF application was again compared with steady state condition.

Starting from the analysis in *Symmetry Position*, it was noticed a peak of amplitude for pulsed frequency values close to characteristic frequency of vortices: relative amplitude of *fft* for pulsed velocity reached 2000 initial position of the inductor but it was three times more for its mid height, *Inductor Position 3*, and almost 3500 for the top position. The peak was much more evident if compared with *fft* for AC current (blue dots in Fig.4.7, 4.8, 4.9); in the case of steady state signal, no predominant frequency components were present, therefore all of the frequency components had the same energy.

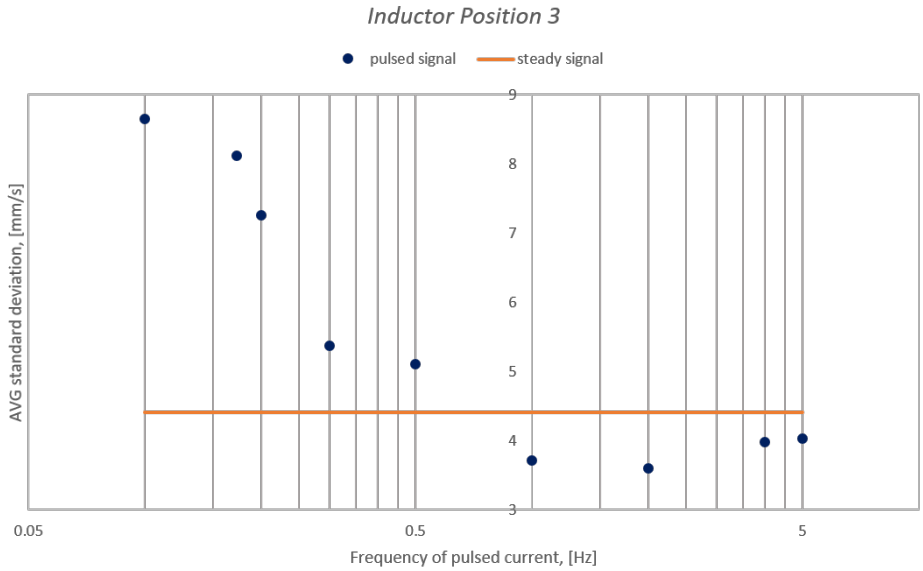

Fig. 4.4: Average standard deviation over f_p pulsed frequency for *Inductor Position 3*. Orange row refers to AMF application, blue dots to PMF application.

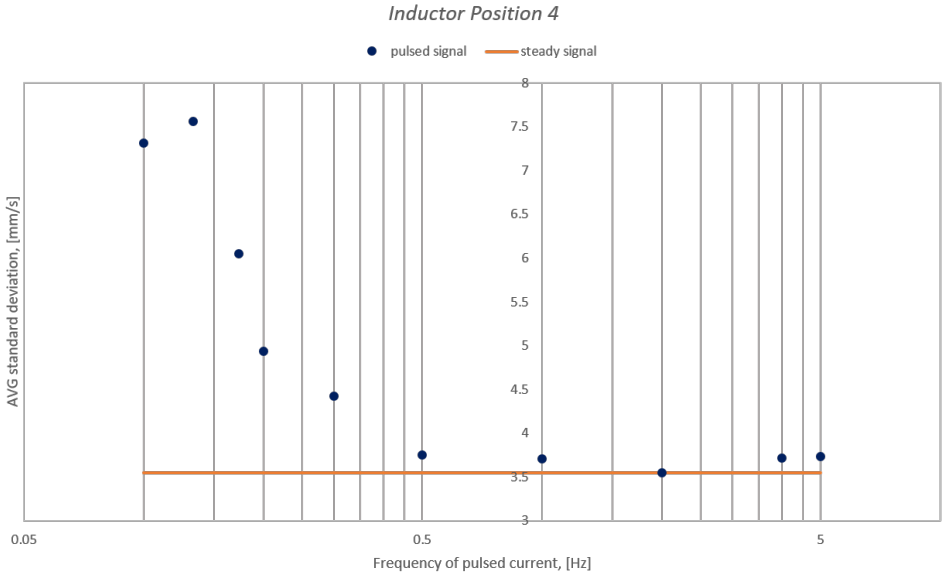

Fig. 4.5: Average standard deviation over f_p pulsed frequency for *Inductor Position 4*.

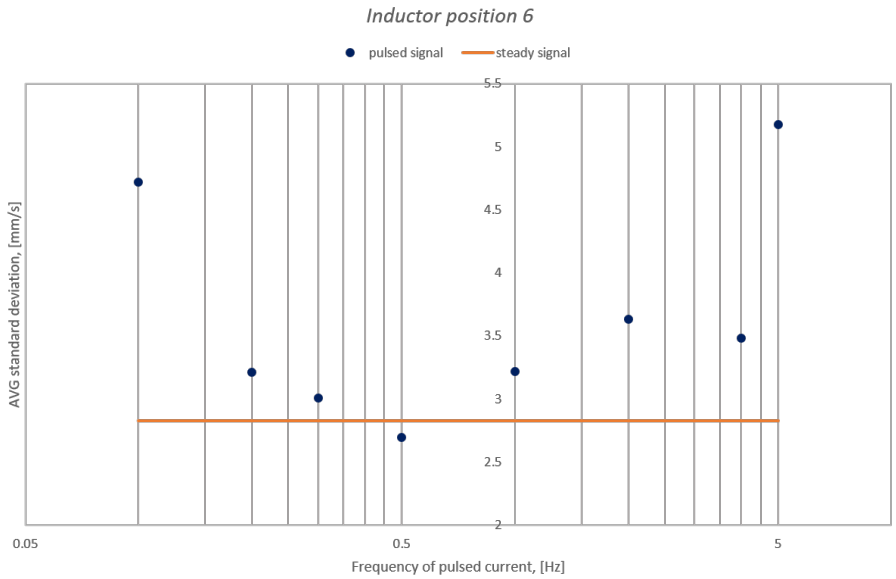

Fig. 4.6: Average standard deviation over f_p pulsed frequency for *Inductor Position 6*.

Finally, experimental activities represented further validation of resonance effect with PMF application. Superficial behaviour of melt was directly observed and registered: it was noticed that motion of melt on its surface was much intense when f_p pulsed frequency of the signal was close to the characteristic frequency of vortices, and obviously when pulsed current was applied instead of AC one. This last comparison also evidenced the difference between intermittent superficial waves in PMF application and stable, much less intense waves in the case of AMF.

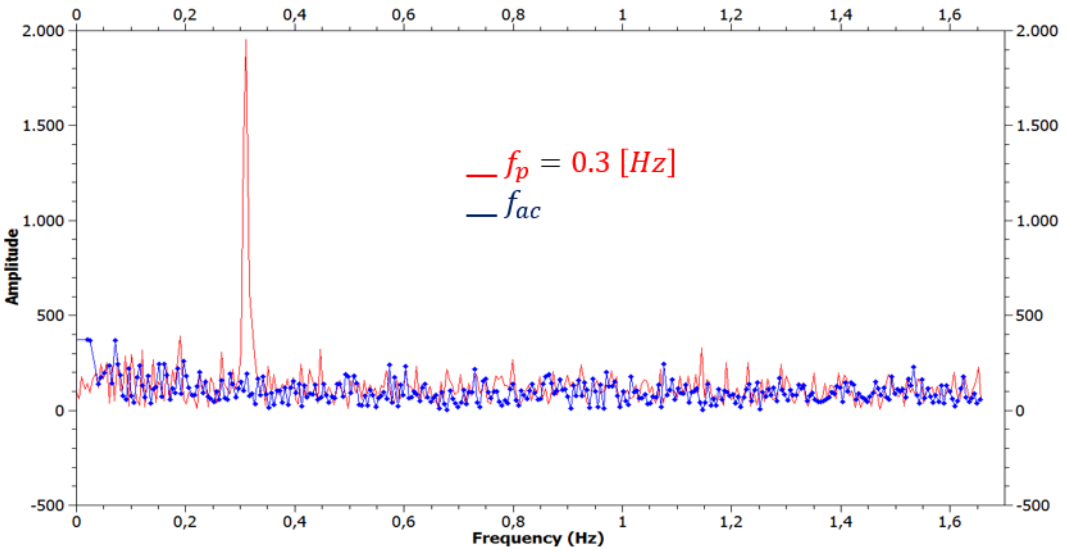

Fig. 4.7: *Fast Fourier Transform* of pulsed component of axial velocity along the axis for *Inductor Position Zero* and $f_p = 0.3[Hz]$. It was compared with steady state AC conditions.

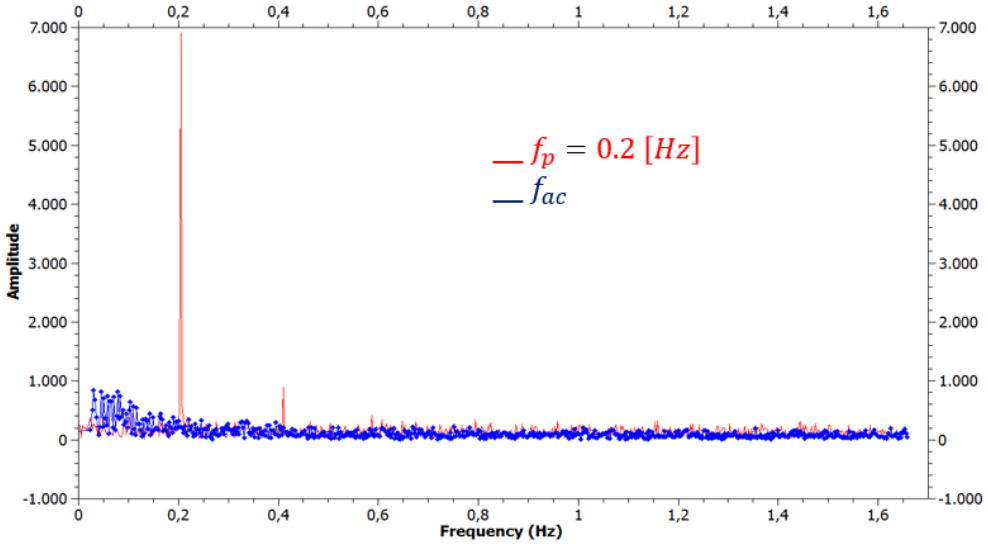

Fig. 4.8: *Fast Fourier Transform* of pulsed component of axial velocity along the axis for *Inductor Position 3* and $f_p = 0.2[Hz]$. It was compared with steady state AC conditions.

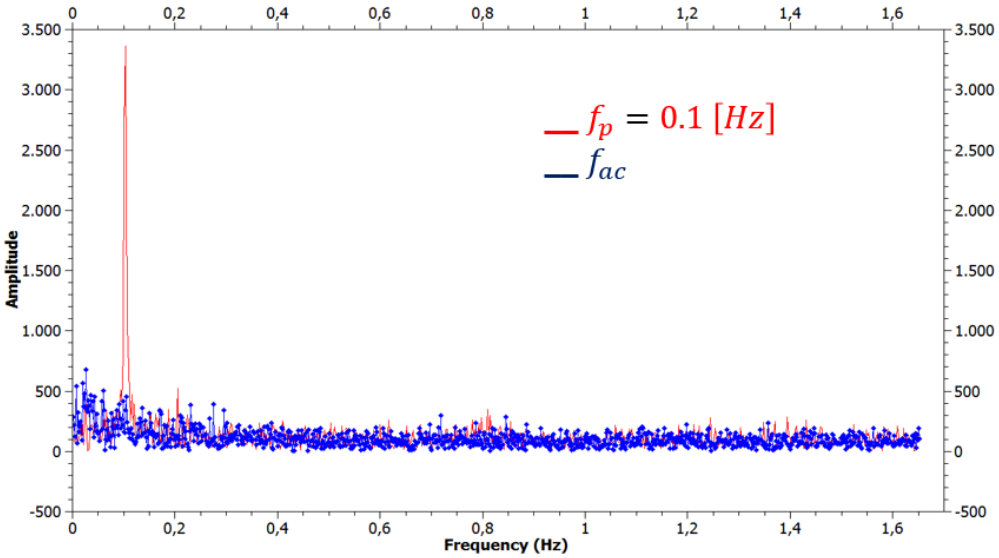

Fig. 4.9: *Fast Fourier Transform* of pulsed component of axial velocity along the axis for *Inductor Position 6* and $f_p = 0.1[Hz]$. It was compared with steady state AC conditions.

Chapter 5

Conclusions and final remarks

This thesis work was carried out at the ETP, Hannover Institute of Electroheating, in the frame of the application of low-frequency pulsed Lorentz force for electromagnetic stirring of molten metals. Both numerical simulations and experimental activities were carried out in parallel, on the base of previous studies on the same experimental setup. Main goal of this investigation was to optimize stirring effects on molten metal with the use of pulsed magnetic field (PMF) in substitution to the more classical alternate magnetic field (AMF) for Continuous Casting, in non standard conditions.

GalInStan melt was chosen for the investigation. The initial step consisted in analysing steady state application of AMF: when the inductor was in *symmetrical position* with melt volume, two toroidal eddies with similar velocity, amplitude and energy were generated, as expected; the same set of electromagnetic quantities was applied while relative position between inductor and the melt was changed. The inductor, a 6-turns, copper coil, moved upward and great variation of vortices properties was produced. A unique, more energetic eddy was generated and the *transition* from two-to-one vortices happened when the inductor overcame almost half of melt's height (it was previously named *Inductor position 3*. In order to quantify flow intensity inside the melt, axial component of their velocity was measured both along the axis and next to the border of the liquid, because they represented the most significant data. Each step of numerical investigation was validated with experimental activities in the same conditions and good correspondence between their results was found. For hydrodynamic simulation, $k-\varepsilon$ model was adopted and axial velocity form numerical results was extremely close the experimental one, for each position of the inductor. On the other hand, $k-\omega$ algorithm was abandoned because its strong concentration of velocity distribution next to melt volume corners. UDV probe was chosen for experimental measurements of velocity inside molten metal.

Once the *transition* was identified, optimization of PMF application started: charac-

teristic properties of vortices in non symmetrical position of the inductor were calculated to achieve resonance effect between mechanical quantities of the melt (flow velocity) and electromagnetic parameters (current feeding the coil). Pulsed current was fixed with the same characteristic frequency of vortices and intensity of flow motion was analysed again. Average standard deviation of pulsed component of axial velocity was calculated, and its fast Fourier transform as well, for each position of the inductor and each frequency in the range of pulsed ones. Expected results were achieved again: from the evaluation of standard deviation it was found that pulsed velocity component increased its value of two times when frequency of supplied current was close around the characteristic one of vortices; really low motion was therefore achieved when pulsed frequency was far away and the same results as for AMF application were thus noticed. Fast Fourier transform validated the previous results and a peak in the amplitude of pulsed velocity component was evident for the same pulsed frequencies as the characteristic ones. Finally, strong motion of GalInStan melt was verified with direct observation during experimental activities: AMF application was noticed to produce small and low-intensity superficial oscillations of the liquid, with casual frame; on the other hand, pulsed frequency of current was evident to produce big waves on melt' surface, which shifted towards central point with fixed rhythm and higher speed. Resonance between motion of the flow and feeding pulsed current was definitely achieved with proper choice of electromagnetic parameters, thus stronger intensity of motion than the one with classical AMF application.

Bibliography

[1] Kolesnichenko A. F., Podoltsev A. D., Kucheryavaya I. N., *Action of Pulse Magnetic Field on Molten Metal*, ISIJ Internation, Vol. 34 (1994), No. 9, pp. 715-721

[2] Musaeva D., Baake E., *Experimental Investigation of Al-Alloy Directional Solidification in Pulsed Electromagnetic Field*, Materials Science Forum, Vol. 870 (September 2016), pp. 471-476

[3] Baldan M. (2016). *Numerical and practical investigation of an inhomogeneous heating process for forging parts* (Master's Thesis). Retreived from Padova Digital University Archive. (ID Code: 52123)

[4] B.G. Thomas, *Continuous Casting: Modeling*, The Encyclopedia of Advanced Materials, (J. Dantzig, A. Greenwell, J. Michalczyk, eds.) Pergamon Elsevier Science Ltd., Oxford, UK, Vol. 2 (2001), pp. 8-31

[5] Liu T., Sen P., Kim C.J., *Characterization of Nontoxic Liquid-Metal Alloy Galinstan for Applications in Microdevices*, Journal of Microelectromechanical Systems, Vol. 21 (April 2012), No. 2, pp. 443-450

[6] El-Kaddah N., Natarajan T.T., *Electromagnetic stirring of steel: effect of stirrer design on mixing in horizontal electromagnetic stirring of steel slabs*, Processing of the Second International Conference on CFD in the Minerals and Process Industries, CSIRO, Melbourne, Australia, 6-8 December 1999, pp. 339-344

[7] Musaeva D., Ilin V., Baake E., Geža V., *Numerical Simulation of the melt flow in an induction crucible furnace driven by a Lorentz force pulsed at low frequency*, Magnetohydrodynamics, Vol. 51 (October 2015), No. 4, pp. 771–783

[8] Hellawell A., Liu S., Lu S.Z., *Dendrite Fragmentation and the Effects of Fluid Flow in Castings*, JOM, 1997, pp. 18-20

[9] Su Z.J., Chen J., Nakajima K., He J.C., *Criterion for Dendrite Fragmentation of Carbon Steel under Imposition of Linear Travelling EMS*, Steel Research, int. 80 (2009), No. 11, pp. 824-833

[10] Xu Y., Wang T., Wang F., Wang E., *Influence of lower frequency electromagnetic field on dendritic crystal growth in special alloys*, Journal of Crystal Growth, Vol. 468 (2017), pp. 506-509

[11] Li Y., Cui X., Jin G., Cai Z., Tan N., Lu B., Yang Y., Gao Z., Liu J., *Influence of magnetic field on microstructure and properties of Ti/cobalt-based composite plasma cladding coating*, Surface and Coatings Technology, Vol. 325 (2017), pp. 555-564

[12] Dandan J., *Flow measurement in liquid metals using Lorentz force velocimetry: laboratory experiments and numerical simulations* (Ph.D. dissertation), Fakultät für Maschinenbau (Department of Engineering), Technischen Universität Ilmenau, Ilmenau, 2012

[13] Ma X., Yang Y., Wang B., *Effect of pulsed magnetic field on superalloy melt*, International Journal of Heat and Mass Transfer, Vol. 52 (2009), pp. 5285–5292

[14] Tzavaras A.A., Brody H.D., *Electromagnetic Stirring and Continuous Casting - Achievements, Problems, and Goals*, Journal of Metals (March 1984), pp. 31-32

[15] Poole G., El-Kaddah N., *Effect of Coil Design on the Temperature and Velocity Fields during Solidification in Electromagnetic Stirring Processes*, ISIJ International, Vol. 54 (2014), No. 2, pp. 321–327

[16] Willers B., Barna M.,Reiter J., Eckert S., *Experimental Investigations of Rotary Electromagnetic Mould Stirring in Continuous Casting Using a Cold Liquid Metal Model*, ISIJ International, Vol. 57 (2017), No. 3, pp. 468–477

[17] Toh T., Hasegawa H., Harada H., *Evaluation of Multiphase Phenomena in Mold Pool under In-mold Electromagnetic Stirring in Steel Continuous Casting*, ISIJ International, Vol. 41 (2001), No. 10, pp. 1245–1251

[18] Dickey M.D., Chiechi R.C., Larsen R.J., Weiss E.A., Weitz D.A., Whitesides G.M., *Eutectic Gallium-Indium (EGaIn): A Liquid Metal Alloy for the Formation of Stable Structures in Microchannels at Room Temperature*, Advanced Functional Materials, Vol. 18 (2008), pp. 1097-1104

[19] Morley N.B., Burris J., Cadwallader L.C., Nornberg M.D., *GaInStan usage in research laboratory*, Review of Scientific Instruments, Vol. 79 (2008)

[20] Haiyan T., Xiaochen G., Guanghui W., Yong W., *Effect of Gas Blown Modes on Mixing Phenomena in a Bottom Stirring Ladle with Dual Plugs*, ISIJ International, Vol. 56 (2016), No. 12, pp. 2161–2170

[21] Kumar A., Dutta P., *A scaling analysis of alloy solidification in presence of electromagnetic stirring*, Journal of Physics D: Applied Physics, Vol. 39 (2006), pp. 3058-3066

[22] Musaeva D., Ilin V., Baake E., Gež̆a V., *Influence of low-frequency pulsed Lorentz force on the melt flow and the structure of solidifying material*, Research and Development (January 2016), pp. 61-66

[23] Musaeva D., Ilin V., Baake E., Gež̆a V., *Experimental investigation of low-frequency pulsed Lorentz force influence on the motion of Galinstan melt*, SP JPM (2016), pp. 1-8

[24] Nakai Y., Hino Y., Sumi I., Kikuchi N., Uchida Y., Miki Y., *Effect of Flux Addition Method on Hot Metal Desulfurization by Mechanical Stirring Process*, ISIJ International, Vol. 55 (2015), No. 7, pp. 1398–1407

[25] Horiuchi S., Uddin M.A., Kato Y., Kikuchi N., *Liquid/liquid Mixing Pattern in a Mechanically-stirred Vessel*, ISIJ International, Vol. 54 (2014), No. 1, pp. 82–86

[26] Zhu X.R., Harding R.A., Campbell J., *Calculation of the free surface shape in the electromagnetic processing of liquid metals*, Appl. Math. Modelling, Vol. 21 (April 1997), pp. 207-214

[27] Haiqi Y., Miaoyong Z., *Three-Dimensional Magnetohydrodynamic Calculation for Coupling Multiphase Flow in Round Billet Continuous Casting Mold With Electromagnetic Stirring* , IEEE Transactions on Magnetic, Vol. 46 (January 2010), No. 1, pp. 82-86

[28] Fujisaki K., Ueyama T., Okazawa K., *Magnetohydrodynamic Calculation of In-Mold Electromagnetic Stirring*, IEEE Transactions on Magnetic, Vol. 33 (March 1997), No. 2, pp. 1642-1645

[29] Spitzer K.H., Reiter G., Schwerdtfeger K., *Multi-Frequency Electromagnetic Stirring of Liquid Metals*, ISIJ International, Vol. 36 (1996), No. 5, pp. 487-492

[30] Spitzer K.H., Dubke M., Schwerdtfeger K., *Rotational Electromagnetic Stirring in Continuous Casting of Round Strands*, Metallurgical Transactions B, Vol. 17B (March 1986), pp. 119-120

[31] Shiba R., Uddin M.A., Kato Y., Kitamura S., *Solid/liquid Mass Transfer Correlated to Mixing Pattern in a Mechanically-stirred Vessel*, ISIJ International, Vol. 54 (2014), No. 12, pp. 2754–2760

[32] Kirpo M., *Modeling of Turbulence Properties and Particle Transport in Recirculated Flows* (Ph.D. dissertation), Department of Physics, University of Latvia, Riga, 2008

[33] Salandin F., *Sistemi per il rimescolamento elettromagnetico di compositi metallici allo stato fuso* (Bachelor's Thesis), Facoltà di Ingegneria (Department of Engineering), Università degli Studi di Padova, Padova, 2011

[34] Umbraško A., *Heat and mass transfer in electromagnetically driven recirculated turbulent flows* (Ph.D. dissertation), Faculty of Physics and Mathematics, University of Latvia, Riga, 2010

[35] Mohammed M.N., Omar M.Z., Salleh M.S., Alhawari K.S., Kapranos P., *Semisolid Metal Processing Techniques for Nondendritic Feedstock Production*, The Scientific World Journal (2013), pp. 1-16

[36] Takagi H., Uetani Y., Dohi M., Yamashita T., Matsuda k., Ikeno S., *Effects of Mechanical Stirring and Vibrations on the Microstructure of Hypereutectic Al-Si-Cu-Mg Alloy Billets*, Materials Transactions, Vol. 48, No. 5 (2007), pp. 960-966

[37] Puga H., Barbosa J., Seabra E., Ribeiro S., Prokic M., *The influence of processing parameters on the ultrasonic degassing of molten $AlSi9Cu3$ aluminium alloy*, Materials Letters 63 (2009), pp. 806-808

[38] Thrum A., *Induction or gas stirring in ladle furnaces - a comparison*, ABB

[39] Spitans S., Jakovics A., Baake E., Naake B., *Numerical Modelling of Free Surface Dynamics of Melt in an Alternate Electromagnetic Field*, Metallurgical and Materials Transactions B, Vol. 47, No. 1 (2016), pp. 522–536

[40] Soresk A., Kudlinski Z., *The influence of the near-meniscus zone in continuous casting mold on the surface quality of the continuous casting ingots*, Archive of Metallurgy and Materials, Vol. 57, No. 1 (2012), pp. 371-377

Sitography

[41] Introduction to Continuous Casting, University of Illinois,
http://ccc.illinois.edu/introduction/overview.html

[42] Continuous Casting, Wikipedia,
https://en.wikipedia.org/wiki/Continuous_casting

[43] Nucleation and Crystallization, SlideShare website,
https://www.slideshare.net/umairbukhari3/
nucleation-crystallization

[44] Solidification Processes of Materials in Magnetic Fields, JOM,
http://www.tms.org/pubs/journals/JOM/9802/Li/Li-9802.
html

[45] Modeling solidification and mushy zone deformation of alloys, SciELO website,
http://www.scielo.br/scielo.php?script=sci_arttext&pid=
S1678-58782003000200011

[46] Comprehensive Material Processing, google books,
https://books.google.it/books

[47] Electromagnetic stirring in Continuous Casting process, Ispat guru website,
http://ispatguru.com/electromagnetic-stirring-in-\
continuous-casting-process/